Study of novel organic/inorganic hybrid optical scattering materials based on spectroscopic refractive index matching

朱, 峻鋒

Doctoral Thesis

Academic Year 2021

Study of novel organic/inorganic hybrid optical scattering materials based on spectroscopic refractive index matching

Graduate School of Information Science and Electrical Engineering, Kyushu University

Zhu Junfeng

A Doctoral Thesis

submitted to Graduate School of Information Science and Electrical Engineering, Kyushu University

Zhu Junfeng

Thesis Committee:

Professor Shunji Kimura	(Supervisor)
Professor Kazutoshi Kato	(Co-Supervisor)
Professor Yuji Oki	(Co-Supervisor)
Associate Professor Naoya Tate	(Co-Supervisor)

Contents

List of Figures

List of Tables

Chapter 1

Introduction

1.1. Background and motivation

The methods that used the interaction between light and matter to estimate and quantify the subject in a sample, such as absorption spectroscopy and fluorescence spectroscopy [1–5], are increasingly used in our daily lives. In general, spectroscopy-based detecting methods will not harm the measured sample because its principle is based on the substance's absorption or emission of light. It is widely used for solid, liquid, or gas sample detection. Spectroscopy can identify whether the target material is present in the sample and its concentration and degree of crystallinity. Therefore, it is used in various fields, including biology, chemistry, and medical measurement [6–13]. Normally, various spectroscopic devices are necessary to evaluate substances based on spectroscopic methods. The spectroscopic function of these traditional spectroscopic devices is generally divided into four main categories depending on whether they are based on physical or chemical principles and regular structures: 1. spectroscopic devices are based on physical regular structures, such as dielectric filters, grating, prism, etc. 2. spectroscopic devices based on chemical regular structure, such as Previskite, Metal organic frameworks (MOF), etc. 3. spectroscopic devices based on chemical random structure, such as Color filter. However, there have been almost no such devices for the 4th category of physical random structure-based spectroscopy devices until now. Therefore, here, our research team creatively proposed the concept of the spectroscopic refractive index matching principle (SRIM). The basic principle of this concept is that the refractive index (RI) of inorganic materials is greater than that of organic materials in the visible region. In contrast, in the ultraviolet (UV) region, the refractive index of organic materials exceeds that of inorganic materials due to the strong absorption, which caused a refractive index matching point at a specific wavelength. The organic-inorganic hybrid material behaves as

transparent for the light corresponding to the wavelength at the cross-point, while the light acts as scattered for other wavelengths. Such a scattering spectroscopic material does not require a regular structure, so it belongs to the class of physical random structures. On the other hand, some optical detection equipment was constructed based on traditional spectroscopic devices, such as spectrophotometers, fluorescence spectrophotometers, etc. They are usually built based on a spatial optical path system and are often large and heavy because they consist of various optical components precisely arranged and fixed on an optical substrate, ensuring high measurement accuracy but unfavorable in portability and cost. Here, our research team has proposed another concept that uses organic polydimethylsiloxane (PDMS) as a matrix material to rapidly manufacture printable, monolithic integrated micro-optical sensing/detecting devices through techniques such as imprinting, transfer printing, and 3D printing. It is called Silicone Optical Technology (SOT®) [14–17]. Because organic PDMS materials have the characteristics of good flexibility, high light transmittance, strong biological affinity, and low cost. Based on this technology, so far, our research team has developed a variety of optical components and equipment, such as flexible optical lenses, gratings, wavelength conversion filters, etc. And combined with the developed optical components, our team has developed a portable absorbance measurement device using the light absorption and scattering suppression structure of dispersed carbon particles [18]. This portable device can be used to detect various biological and chemical substances. The successful production of these small, micro-optical components and equipment based on PDMS matrices not only provides a more straightforward, faster, and low-cost method for the output of sensing devices and measuring instruments based on the principles of spectroscopy but also provides the technical conditions of miniaturization, flexibility, and wearability for general rigid sensing/ detecting devices, which are highly significant for the upcoming era

of Internet of Everything. Then, our recent research focuses on combining the above-mentioned SOT technology and microfluidic technology [19–40] to develop a miniature optical device that can be used for instant detection of DNA/protein. The basic principle of their spectroscopy is to use absorbance measurement of DNA/protein at UV absorption peaks of 260/280 nm [41–43].Hence, a UV transparent spectroscopic material with a narrow bandwidth below 10 nm is required.

Here, in this thesis, based on the novel principle of SRIM and SOT technology, transparent scattering hybrid materials in a specific wavelength were creatively developed by dispersing disordered inorganic CaF_2 micro-nano particles in an organic PDMS matrix material. This hybrid material can be used to make modules and equipment with spectroscopic properties through various methods such as film formation, potting, vacuum injection. And the transparent scattering filter based on the hybrid material is flexible, simple, and cheap to manufacture; it does not require surface polishing and is not limited by the incident angle of the input light. Then, the hybrid material achieved the tunability of the transparent wavelength by multi-dispersed matrix materials/nanomaterials based on the effective medium approximation theory (EMA). Furthermore, the effect of particle size, particle size distribution, particle concentration, and sample thickness on this scattering spectroscopic material is partially explained based on the Rayleigh-Gans-Debye (RGD) scattering calculation and the Monte Carlo random walk scattering simulation. Afterward, a spectroscopic material with a transmittance bandwidth of around 10 nm was developed based on the optimal conditions given by the simulation. It has laid a solid foundation for the subsequent development of DNA/protein microfluidic photoelectric equipment for medical point-of-care testing [44–59].

1.2. Chapter overview

The first chapter is the introduction of this thesis. In this chapter, the background and motivation of this study are mainly described. In addition, the structure of this thesis and the outline of each chapter are also explained.

Chapter 2 describes the fundamental physical and statistical theories involved in this study, including the novel spectroscopic refractive index matching (SRIM) principle and the scattering model constructed based on the physical and statistical theories. The properties of some necessary materials are also described.

Chapter 3 focuses on developing the world's first flexible scattering filter materials with transparency at 278 nm, etc. UV wavelengths by dispersing disordered CaF_2 particles into PDMS matrix materials based on the SRIM principle. Then, a simple RGD and Hulst approximation calculation can clarify the effective transmittance of scattering materials in the UV region. The results of this part have been reported in Optical Materials Express [60] and Conference on Lasers and Electro-Optics (CLEO) 2018 [61].

Chapter 4 focuses on tuning transparent peak wavelengths (controlling SRIM wavelength) by multi-dispersing hybrid materials or external conditions such as temperature. The transparent wavelength-tunable range is about 30 nm was obtained at this stage. Then, according to the Monte-Carlo theory that considers the RGD approximation and the experimental results of the diffusing angular distribution of scattered light at different wavelengths, an RW model is constructed to clarify part of the distribution of scattering light and effective transmittance. The results of this part have been reported in Optical Materials [62] and Conference on Lasers and Electro-Optics (CLEO) 2020 [63].

Chapter 5 focuses on finding out the conditions of optimizing sample thickness, concentration, and particle size distribution for improving spectroscopic perfor-

mance at this stage by enhancing the RW scattering model in Chapter 4. Then, the optical module combining CaF_2 dispersing PDMS scattering material and UV LED fabricated at the present stage of optimum conditions achieves an actual spectroscopic bandwidth of 9 nm. The results of this part have been reported in Proceeding of The International Society for Optics and Photonics (SPIE) 2021 [64] and Optical Materials Express [65].

Chapter 6 is the simulation and discussion. It summarizes the evolution of the RGD-Hulst model, the simple RW model, the improved RW model, their advantages and disadvantages, and their scope of application.

Chapter 7 is the conclusion. It summarizes the research results of this thesis and discusses future prospects.

The relationship between the subject matter of this thesis in Chapters 3 to 5 is shown in Figure 1.1. The spectroscopic functions are explored from discovery, extension to optimization with spectroscopic refractive index matching as the core.

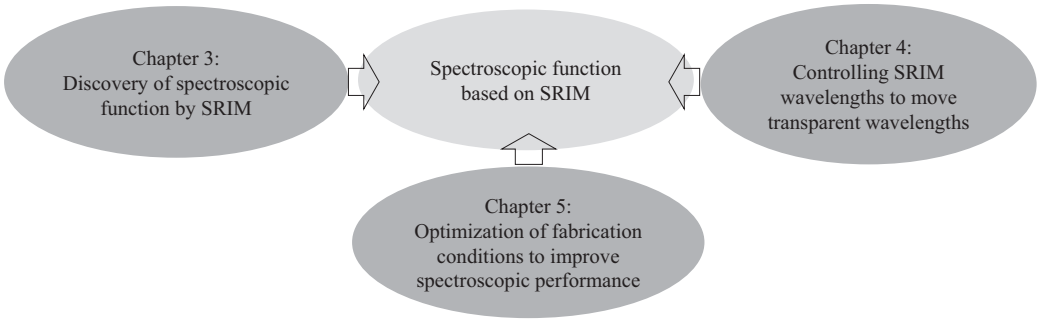

Figure 1.1: Relationships among the Chapters.The spectroscopic function based on spectroscopic refractive index matching is the core of this thesis

Chapter 2

Theory

2.1. Introduction

This chapter will detail the various research theories involved in this thesis. First, the names and properties of some of the materials used in this thesis to make spectroscopic scattering materials are shown. Then, the fundamental theories used in this thesis to develop spectroscopic scattering materials, i.e., spectroscopic refractive index matching (SRIM) theory and RGD and Hulst scattering approximation principles based on various refractive index (RI) differences. Also, Sellmeier's equation for simulating refractive index dispersion, effective medium approximation (EMA) theory for calculating the effective refractive index of mixtures are also presented. Finally, the random walk (RW) model based on the Monte-Carlo principle is also introduced, which is mainly used for the simulation of scattered light distribution and transmittance in this thesis.

2.2. The properties of Various material in this thesis

2.2.1 Organic martrix materials

The organic matrix material used in this thesis is mainly PDMS, which is a high molecular weight compound with a siloxane bond ($-\mathrm{Si}-\mathrm{O}-\mathrm{Si}-$) as the main chain and organic groups attached to the side chains. The molecular structure of a typical PDMS is shown in the Figure 2.1.

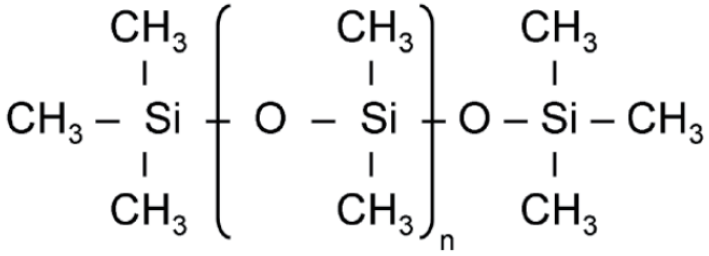

Figure 2.1: PDMS molecular structure [66]

Then, as shown in Figure 2.2, the figure demonstrates some properties of PDMS, such as flexibility, heat resistance, chemical stability, UV transmission, bioaffinity, simple curing and molding, transferable complex microstructures, low cost, etc. In this thesis, high UV transmittance, bio-affinity, and the simplicity of molding are mainly used in this study.

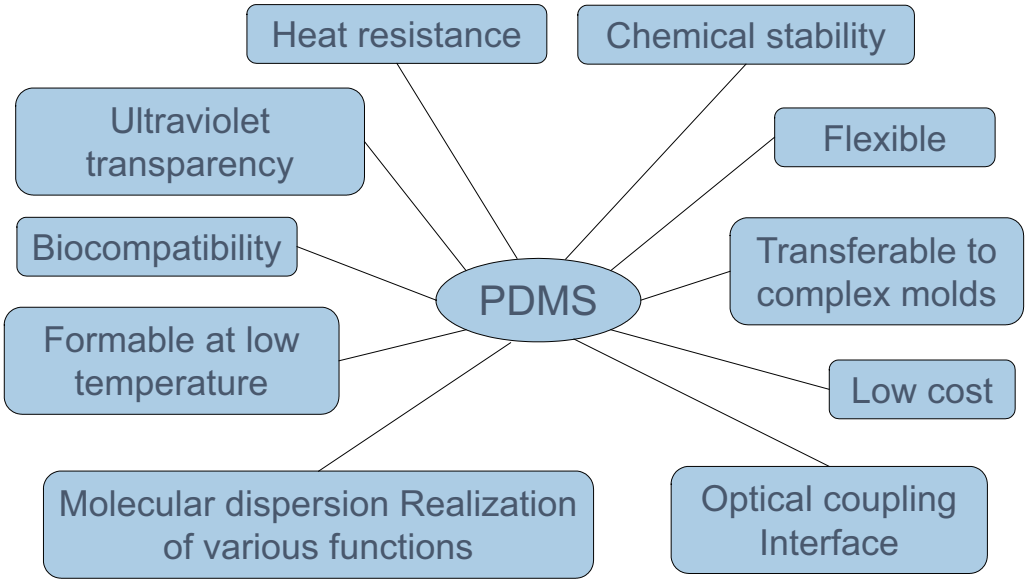

Figure 2.2: Advantages of PDMS

Then, some organic PDMS materials were used as matrix materials or additive

materials in this thesis. Four different PDMS matrix materials are frequently used in these studies, namely matrix A, B, C, and D. Among them, matrix A, B, and C can be cured by adding a curing agent. In contrast, matrix D is a pure PDMS material with low molecular weight (LMW-PDMS), which does not harden even when curing agents are added. They are numbered as follows.

- Matrix-A: SIM-360 (Made by Shin-Etsu Chemical)
- Matrix-B: KE-103 (Made by Shin-Etsu Chemical)
- Matrix-C: SYLGARD-184 (Made by Dow Corning)
- Matrix-D: RTV thinner (Low molecular weight PDMS (LMW-PDMS), made by Shin-Etsu Chemical)

Figure 2.3 shows the transmittance spectra of 1 mm samples of these four organic PDMS matrix materials. Matrix A, B, C are the cured samples, D is the liquid sample. It can be observed that all four PDMS matrices have a transmittance of more than 60 % in the UV region above 240—300 nm. Moreover, the LMW-PDMS matrix still has high transmittance even in the 200—240 nm UV region. In addition, as one of several optical parameters of main interest in this thesis, refractive index dispersions will be given and discussed in the next section of refractive index matching principles (Section 2.3.1).

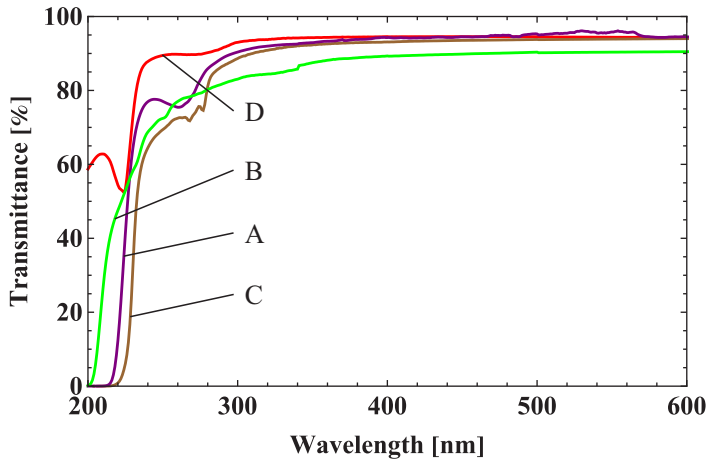

Figure 2.3: 1 mm thick measured transmittance spectra of solid samples with matrix A, B, C, and liquid sample with matrix D

2.2.2 Inorganic dispersant materials

There are three primary inorganic dispersant materials used in this thesis, of which high-purity SiO_2 and CaF_2 particles are mainly used as dispersants to produce refractive index matching. In contrast, nano-quantum dot materials are primarily used as refractive index adjusting agents. SiO_2 and CaF_2 were chosen as refractive index-matched dispersants because their refractive indices are close to those of PDMS, and the high purity SiO_2 and CaF_2 have extremely high transmittance even in the UV regions. The reason for choosing nano-quantum dot materials as refractive index adjusting agents is that their refractive indices are much larger than PDMS, effectively enhancing the refractive index dispersion of PDMS matrices with a tiny amount of doping. First, SiO_2 was selected as shown in Table 2.1. The SiO_2 was Shin-Etsu Chemical powder (X-24-9163A) with an average particle size of 0.1 μm. Then, four different CaF_2 powder particles were selected for the experiments in this thesis. As shown in Table 2.2, the CaF_2 pow-

der I used here was filed by excimer laser window of OKEN (Applied OKEN Co., Ltd.) using a hand file, and its particle size was randomly distributed. Powder II-IV are commodities, and their particle size distribution is shown in Table 2.2. Then, powder V is made from CaF_2 molding material based on an electric router with a diamond drill, and powder VI is obtained from CaF_2 molding material based on a 3D milling machine with a diamond drill. The effect of the particle size distribution of CaF_2 on the experimental results will be discussed in detail in Chapter 3 and 5. (The particle size range of CaF_2 powders I-IV was observed using an optical microscope (ECLIPSE TE-2000, Nikon), and CaF_2 powders V-*V*I were observed using a scan electron microscope (SEM, TM-4000Plus, Hitachi). They both have an accuracy of about 0.1 μm).

Table 2.2: CaF_2 powder specification

Specifications	I	Ⅱ	Ⅲ	Ⅳ	V	Ⅵ
Maker	OKEN	Wako	High Purity Chemical	Hakushin chemical	OKEN	OKEN
Particle size (μm,Measured value)	0.1-10	0.1-10	5-10	5-50	0.1-80	0.1-50
Purity	Unknown	99.9 %	99.9 %	99.99 %	Unknown	Unknown
Product number	None	LKL 0228	Lot. 4575021	Lot. 805577	None	None
Production method	Diamond file (hand file)	Chemical synthesis	Chemical synthesis	Chemical synthesis	Diamond drill (electric router)	Diamond drill (3D milling machine)

Table 2.1: SiO_2 powder specification

Specifications	SiO_2 powder
Maker	Shin-Etsu Chemical
Particle size (μm)	0.1
Purity	99.9 %
Product number	X-24-9163A
Production method	Chemical synthesis

2.3. Spectroscopic refractive index matching

2.3.1 Spectroscopic refractive index matching

The basic principle of the new organic-inorganic scattering materials with spectral properties developed in this thesis is called spectroscopic refractive index matching (SRIM).

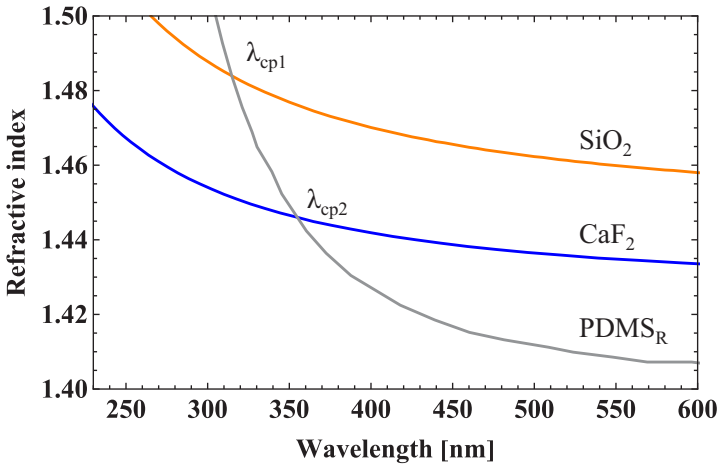

Figure 2.4: Refractive index dispersion of $PDMS_R$ [67], SiO_2 [68], CaF_2 [69]

In this study, the principle of SRIM is based on the difference in the slope of the wavelength-dependent refractive index dispersion curves exhibited by organic and inorganic materials. As shown in Figure 2.4, inorganic UV high transmission materials such as SiO_2, CaF_2, etc., have a slightly higher refractive index in the visible region than organic materials such as PDMS due to their relatively high density. However, their refractive index dispersion is smaller than that of PDMS in the 200—300 nm range because of their shorter cut-off wavelengths than organic materials such as PDMS. Therefore as shown in Figure 2.4, CaF_2 (SiO_2) inorganic materials, and $PDMS_R$ organic materials will reach refractive index agreement at a specific wavelength of λ_{cp2} (λ_{cp1}), i.e. they will have an cross

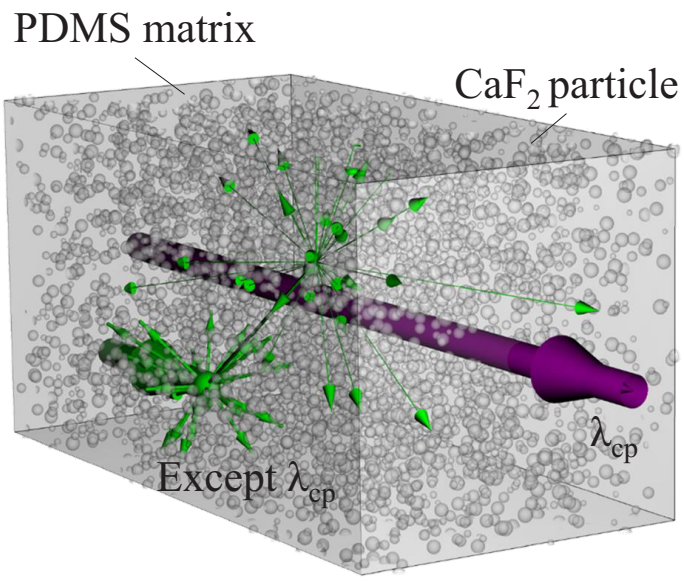

Figure 2.5: Spectroscopic scatterer model

point. Here $PDMS_R$ represents the refractive index dispersion curve obtained from the literature. PDMS from Shin-Etsu Chemical used in this thesis has some differences from the refractive index dispersion curves of $PDMS_R$ because of their different low molecular content. Therefore, it can be inferred that the mixture of PDMS and $CaF_2(SiO_2)$ does not scatter for the light corresponding to the cross point wavelengths λ_{cp2} and (λ_{cp1}). At the same time, it exhibits scattering properties for the other wavelengths. In other words, the material acts as a spectral material that allows light at wavelengths λ_{cp2} (λ_{cp1}) to pass through the organic matrix/inorganic particle hybrid and scatters light at other wavelengths. This new concept is illustrated in the Figure 2.5. In addition, SRIM wavelength is used in this thesis to represent λ_{cp} of two materials.

2.3.2 Sellmeier equation

To determine the dispersion of light in a medium, based on the dispersion model established by Cauchy, Wolfgang Sellmeier proposed an empirical equation known as Sellmeier's equation [70, 71]. It can describe the variation of the refractive index with the wavelength in a specific transparent medium. The equation is shown in 2.1.

$$n^2(\lambda) = A + \sum \frac{B_i \lambda^2}{\lambda^2 - C_i} \tag{2.1}$$

, where n is the refractive index, λ is the wavelength, and A, B_i and C_i are the empirically determined Sellmeier coefficients. The equation is mainly used to provide the refractive indices of different kinds of PDMS and combined with the effective medium approximation theory to simulate the variation of the effective refractive index dispersion of mixtures in the case of multiple dispersions in this thesis.

2.3.3 Effective medium approximation theory

The method of analyzing the mixture of two or more materials as a whole and approximating it to calculate its overall average refractive index and other properties is called the effective medium approximation (EMA) theory [72, 73]. The average refractive index of the hybrid materials is also called the effective refractive index. Generally speaking, there are various theoretical models of EMA theory, including Lorentz–Lorenz (LL) model, Maxwell–Garnett (MG) model, Bruggeman model, etc [74–78]. In this thesis, the effective refractive index simulation of hybrid materials is mainly based on the MG model, and its theoretical formulation is shown in equation 2.2. Because the MG model is more applicable in the case where the content of randomly distributed doped materials in the matrix is

low and their interactions do not have to be considered.

$$\frac{\bar{n}^2 - n_{\mathrm{m}}^2}{\bar{n}^2 + 2n_{\mathrm{m}}^2} = \sum_i P_i \, \frac{n_i^2 - n_{\mathrm{m}}^2}{n_i^2 + 2n_{\mathrm{m}}^2} \tag{2.2}$$

, where $\bar{n}$ is the effective refractive index of the mixture, n_{m} is the refractive index of the matrix material, and n_i is the refractive index of the dispersed (dopant) material. P_i is the volume fraction of the dispersion (dopant).

2.4. Scattering theory of dispersive refractive index difference

This section focuses on the soft optical scattering theory used in this thesis. There are Rayleigh scattering and Mie scattering. Generally, Rayleigh scattering occurs when the scattering particle size is smaller than the wavelength of the incident light. At the same time, Mie scattering occurs when the scattering particle size is close to or larger than the wavelength of the incident light. However, the refractive indices of the mixed materials used in this study are relatively close. In addition to considering the general cases of Rayleigh scattering and Mie scattering, the scattering theory in this study needs to consider the special scattering approximation theory for small refractive index differences. That is Rayleigh Gans Debye (RGD) approximation [79] and van de Hulst (Hulst) approximation [80] theory. They will be discussed in the next subsections. First, The beer-lambert theory was used to calculate the effective transmittance in this thesis, as indicated in equation 2.3.

$$T = e^{-\sigma N L} \tag{2.3}$$

, where T is the transmittance in this thesis. L is the sample thickness, N is the spatial density, and σ is the scattering cross-section area. Also, the spatial density

N is calculated using Equation 2.4.

$$N = \frac{P_i}{\frac{4}{3}\pi\left(\frac{D}{2}\right)^3} \tag{2.4}$$

P_i is the volume fraction of the sample affected by the dispersing concentration. D denotes the diameter of the dispersing particles. As a result, the dispersing concentration and particle size impact the spatial density N.

On the other hand, the scattering cross section area σ is calculated based on a different approximation theory. They are described in the following subsection.

2.4.1 Rayleigh Gans Debye scattering approximation

According to the Beer-Lambert as mentioned above, two parameters affect the overall transmittance per unit thickness, the spatial density N, and the cross-sectional scattering area σ. N is only affected by the concentration and geometry size of the dispersed particle material. σ is different, as it is affected not only by the geometry size and size distribution of the dispersed particle material but also by the refractive index difference of the hybrid material in this thesis. The cross-sectional scattering area in the general case is calculated as in equation 2.5.

$$\sigma_N = \pi(\frac{D}{2})^2 \tag{2.5}$$

A particular approximation condition for Rayleigh scattering can be considered when the refractive index difference between the two materials composing the mixture is tiny, i.e., the RGD scattering approximation [79]. In this case, although the geometry of the dispersed particle material is relatively small, it can be larger than the Rayleigh scattering limit. Then, the RGD approximation is valid, When conditions of 2.6 are matched.

$$\begin{cases} \left|\frac{n_d}{n_p} - 1\right| \ll 1 \\ kD\left|\frac{n_d}{n_p} - 1\right| \ll 1 \end{cases} \tag{2.6}$$

, where k is the wavevector of light in the medium, n_d is the refractive index of the dispersants materials, and n_p is the refractive index of the PDMS matrix. And, the scattering cross-section area can be approximated by the equation 2.7 according to the RGD scattering approximation [79].

$$\sigma_{RGD} = \frac{\varphi^2 \pi (\frac{D}{2})^2}{2} \tag{2.7}$$

, where σ_{RGD} is the RGD model's scattering cross-section, φ is the phase delay of the light wave passing through the particle sphere, and it can be calculated by equation 2.8.

$$\varphi = \frac{kD\delta n}{n_p} \tag{2.8}$$

, where δn is the refractive index difference between two materials.

2.4.2 Van De Hulst scattering approximation

On the other hand, when condition 2.6 is not satisfied, the Hulst approximation theory (also known as the anomalous diffraction approximation) [80] will be considered. Its scattering cross-section σ_{Hulst} is calculated as equation 2.9.

$$\sigma_{Hulst} = (2 - \frac{4}{\varphi} sin\varphi - \frac{4}{\varphi^2}(1 - cos\varphi))\pi(\frac{D}{2})^2 \tag{2.9}$$

2.5. Random walk scattering model

Although simple transmittance calculations based on RGD and Hulst approximation can be used to model the effective transmittance spectra, they cannot model the distribution of scattering light. Therefore, a 3D RW model using Monte-Carlo theory and RGD scattering [79] was proposed in this thesis. Compared to the general Monte Carlo theory-based RW model, this model incorporates the consideration of the RGD scattering case. It is expected to explain and simulate

the scattering of optically soft particles under similar conditions. A 2D view of the 3D RW model is shown in Figure 2.6, which describes the scattering of light by optically soft particles in the $x-z$ plane. A deflected angle of $\Delta\theta$ was obtained after a light beam was injected onto the optical particle. Also, before the light hits another particle, it passes a distance called the free path l. Finally, the process is repeated until the total distance passed on the z-axis exceeds t. Each free path l can be randomly determined, but its average value can be calculated as mean free path (MFP). MFP can be given by $(\sigma_s N)^{-1}$, where N is the spatial density of scattering particles, and σ_s is the scattering cross-sectional area of the particles. The specific model construction process will be described in Chapter 6.

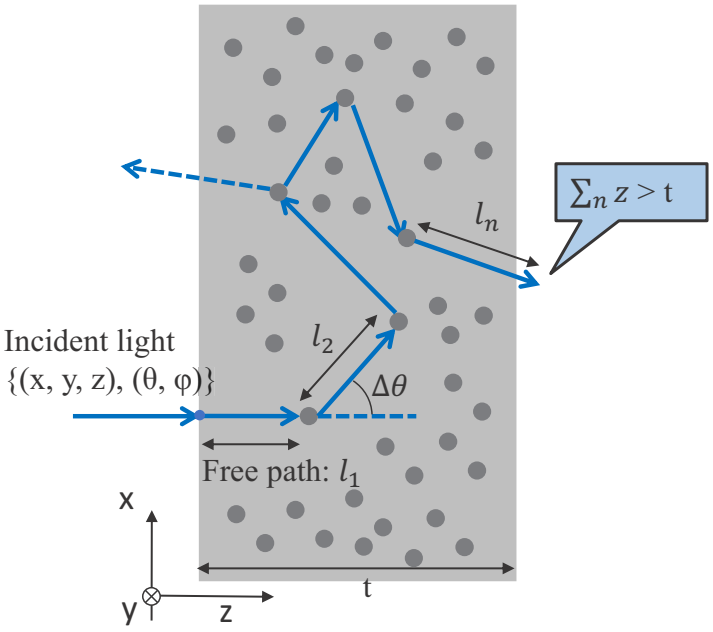

Figure 2.6: Light transmission schematic using the RW scattering model

2.6. Conclusion

This chapter describes the material properties used in this thesis, the theoretical principles, and the simulation models.

Chapter 3

Fabrication and modeling of transparent/scattering hybrid materials with UV bandpass filtering properties

3.1. Introduction and purpose

As described in the 1 Chapter, in order to reach the ultimate goal of developing a UV-transparent spectroscopic material with a narrow bandwidth, the feasibility of the basic principle of SRIM in the UV region first needs to be verified. Therefore, we focus on materials transparent in the UV region and devices with UV spectroscopic properties. However, most organic compounds, such as polymers, are opaque in UV area, so sample containers and liquid tubes must be made of SiO_2 and some forms of fluoropolymers [81]. Similarly, specific materials with interference structures, such as MgF_2 or CaF_2, are commonly utilized to construct UV spectroscopic devices, like the band-pass filters in [82]. While, in spectroscopic applications like the fluorescence microscopes and absorptiometers, optical filters are the most essential and fundamental components [83]. A wavelength filtering optical component usually requires an optical-grade surface prepared by etching, polishing, or imprinting. Furthermore, investigations using silver and silica layers [84] and nano-imprint lithography [85] have demonstrated the simpler integration and variety of UV filtering structures. But the optical surface must likewise be an interference interface. Then, PDMS is used as an embedding or potting material to fabricate some optical devices, such as optical lenses [86–89] for smartphone microscopes and microfluidic channels, soft-lithography techniques [90, 91] based waveguide systems, and optical filters with dye doping PDMS [92], due to PDMS's printability, high transmittance in the visible and UV regions, and ability to provide an optical surface without polishing. In a prior study, the high transparent PDMS was used to design and build a small optical system [18] based on soft molding and a single matrix. The techniques like this one for making a series of optical components and devices based on PDMS matrix materials are called SOT techniques (mentioned in Chapter 1). There-

fore, based on the SOT technique and SRIM principle (described in Chapter 2), a new technique concept for developing band-pass filtering elements is proposed, the conventional polishing, lithography, or coating is not required. In this chapter, PDMS organic materials are used as matrix materials. Scattering hybrid materials with band-pass spectroscopic properties that are transparent at each specific wavelength are developed by simply mixing and dispersing inorganic particulate materials such as SiO_2/ CaF_2. The effective transmittance of scattering hybrid material is calculated based on the RGD and Hulst approximations described in Chapter 2 by combining the refractive index dispersion measurements of various PDMS materials. This will contribute to finding the optimum conditions to satisfy the spectroscopic performance below 10 nm.

3.2. PDMS matrix materials properties

As mentioned in Section 2.3.1, the SRIM principle is based on a slight difference between inorganic and organic materials' normal dispersion slopes.(Figure 3.1). Here, the refractive indices of $PDMS_R$, SiO_2, and CaF_2 are the same as in Figure 2.4. Incident light of cross-point ($\lambda_{cp1}/\lambda_{cp2}$) wavelength was expected to pass through the hybrid medium of inorganic particle and organic matrix, whereas other wavelengths of light were expected to scatter. Then, the PDMS refractive indices [67] (PDMS in the literature is labeled $PDMS_R$) may match those of SiO_2 [68] at wavelength λ_{cp1} of 315 nm and CaF_2 [69] at wavelength λ_{cp2} of 355 nm, according to literature. However, the actual PDMS being used in our study are SIM-360, KE-103, Sylgard-184, and LMW-PDMS (as shown in Section 2.2.1). Therefore, the actual experimentally derived refractive index matching points are somewhat different from the intersection points in Figure 3.1. Moreover, Figure 3.1 showed the refractive indices ellipsometer measurement

results of various PDMS films as matrix candidates (Matrix SIM-360, KE-103, Sylgard-184; measured using SE-2000, SEMILAB Inc.). These dispersion curves differ significantly from the data in Ref. [67]. It shows that λ_{cp} follow the order SIM-360 >KE-103 >Sylgard-184, which contradicts our experimental data (KE-103 <SIM-360 <Sylgard-184) stated in next section. Because of the difficulty of n and k reverse fitting techniques, it cannot achieve refractive indices absolute precision within 0.001 by spectroscopic ellipsometry. Even if the relative index dispersion in Figure 3.1 was correct, the error of λ_{cp} was 4 nm. As a result, using merely spectroscopic ellipsometry measurements to predict and create wavelength-transparent materials is still inadequate at this stage.

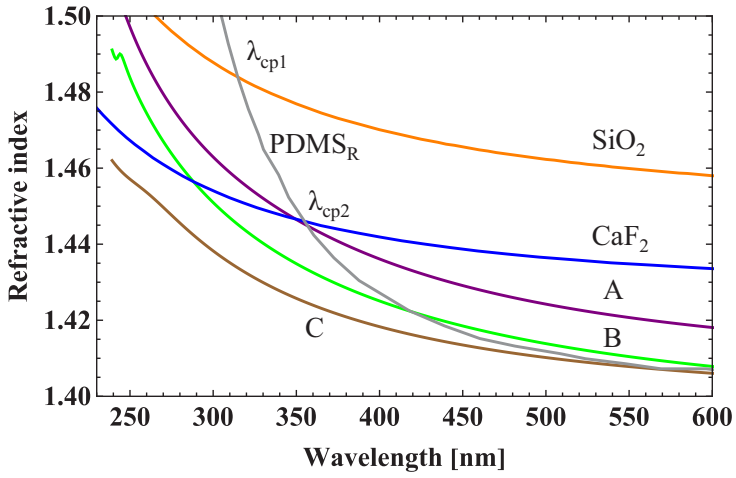

Figure 3.1: $PDMS_R$ (Ref. [67]), SiO_2 (Ref. [68]), and CaF_2 (Ref. [69]) refractive index dispersion from literature; PDMS matrix SIM-360, KE-103, Sylgard-184 (matrix-A, B, C respectively) refractive index dispersion measured by ellipsometer (SE-2000, SEMILAB). SiO_2 and $PDMS_R$ have a cross-point wavelength of λ_{cp1}, whereas CaF_2 and PDMS have a cross-point wavelength of λ_{cp2}

Then, Figure 3.2 demonstrates the calculated PDMS matrices absorption spectra, which were calculated using the measured 1.0 mm thick PDMS matrices (SIM-

360, KE-103, Sylgard-184 in solid-state and LMW-PDMS in liquid state) transmittance spectra (as shown in Figure 2.3). It determines their cut-off wavelengths. The content of cross-linker molecules in different PDMS matrices is responsible for the variation in cut-off wavelengths. Matrix LMW-PDMS has the shortest cut-off wavelength, due to it being almost pure PDMS. As a result, the order of cut-off wavelengths was determined to be LMW-PDMS <KE-103 <SIM-360 <Sylgard-184. This fits with our experimental data presented in the next section.

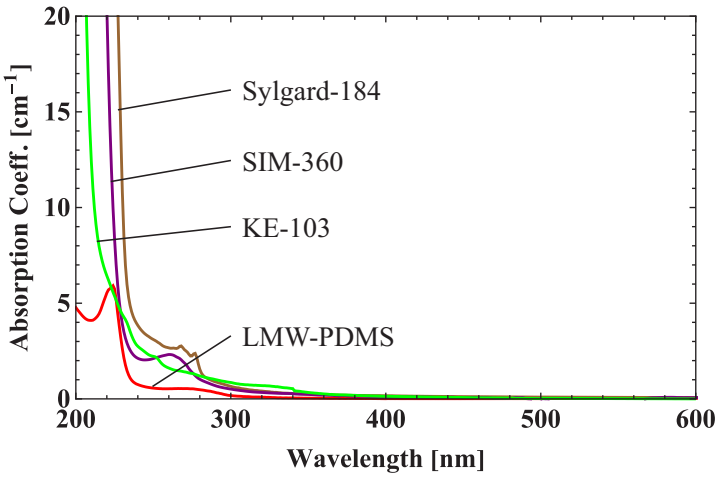

Figure 3.2: Calculated PDMS matrices absorption spectra based on the transmission data in Figure 2.3

The most successful experimental strategy for mixed chemicals was chosen based on the early estimates above. Figure 3.3 depicts the sample fabrication procedure. A planetary centrifugal mixer (KK-50S, Kurabo) was used to mix SiO_2 particles (X-24-9163A, Shinetsu) or CaF_2 particles (OKEN CaF_2 window grinded powder) with PDMS matrices (SIM-360, KE-103, Sylgard-184, and LMW-PDMS). Debubble was done four times with a mixer, each time for 200 seconds at 1440/1108 rpm (revolution/autorotation). The sample is cooled after de-bubbling to remove the heat generated by friction. Afterward, adding the curing agent into

the hybrid and fast mixing for a brief period (90 seconds) to prevent the hybrid from curing too quickly. Then, Filling the hybrid into a 1 mm thick mold, covering a Polymethyl methacrylate (PMMA) plate, and curing for 10 hours at 50 $°C$, after vacuum de-bubbling. A spectrophotometer (V-630, JASCO) and microscopic (ECLIPSE TE2000-U, Nikon) were used to measure the hybrid samples: 1.3 mm thick SiO_2: SIM-360 hybrids, 1.5 mm, thick 1.3 mm, and 1.0 mm thick SIM-360 film and CaF_2: SIM-360 hybrids; 1.0 mm thick KE-103 films and CaF_2: KE-103 hybrids, 1.0 mm thick Sylgard-184 films and CaF_2: Sylgard-184 hybrids, 1.0 mm thick liquid state of LMW-PDMS and CaF_2: LMW-PDMS hybrid. Herein, the transmittance obtained from the experiments in this thesis presents the transmittance results measured under spectrophotometer conditions, also called effective transmittance. Also, CaF_2: PDMS is used in this thesis to denote the hybrid material of CaF_2 and PDMS.

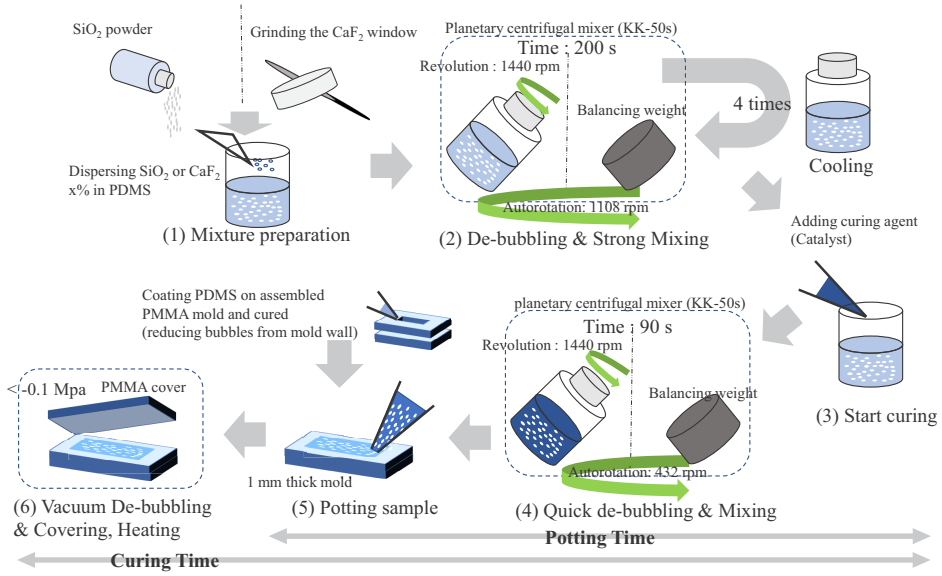

Figure 3.3: Fabrication process of inorganic-organic spectrophotometric scattering hybrid film

3.3. Experiment results and discussion

3.3.1 Results of SiO_2 dispesring PDMS sample films

Figure 3.4(a) shows the manufactured SiO_2: SIM-360 (matrix-A) films transmittance spectra with different SiO_2 concentrations (16, 20, 24 wt.%), and Figure 3.4(b) shows the normalized transmittance spectra based on SIM-360 film transmittance. Over the visible wavelengths range, the films are partially transparent, due to tiny scattering from SiO_2 particles (100 nm size). Despite the lack of SRIM in the estimation from Figure 3.1, the experimental cross-point may be confirmed around 233 nm as a small transparent peak. This contradicts the estimates shown in Figure 3.1. Furthermore, the sample's capacity to obscure visible light is limited due to the smaller particle size. This constraint can be solved by employing bigger particles. Despite being a portion of normalized spectra, the peak transmittance of the sample is 7-80 percent, as illustrated in Figure 3.4(b). Larger scattering is considered as the main reason for the 2-30 % loss (discussed in Section 3.3.3. These findings revealed that SRIM had an effect on the film's light transparency. But the cross-point wavelength was significantly shorter than previously expected values. Furthermore, the absorption of PDMS substantially influenced the measured transmittance spectra; thus, the cross-point wavelength λ_{cp} needs to be shifted to a longer wavelength. Despite the fact that greater particle size is expected to reduce transmittance in the visible region, SiO_2 needs to be replaced with other inorganic materials due to the obtained SRIM wavelength is less influenced by SiO_2 concentration.

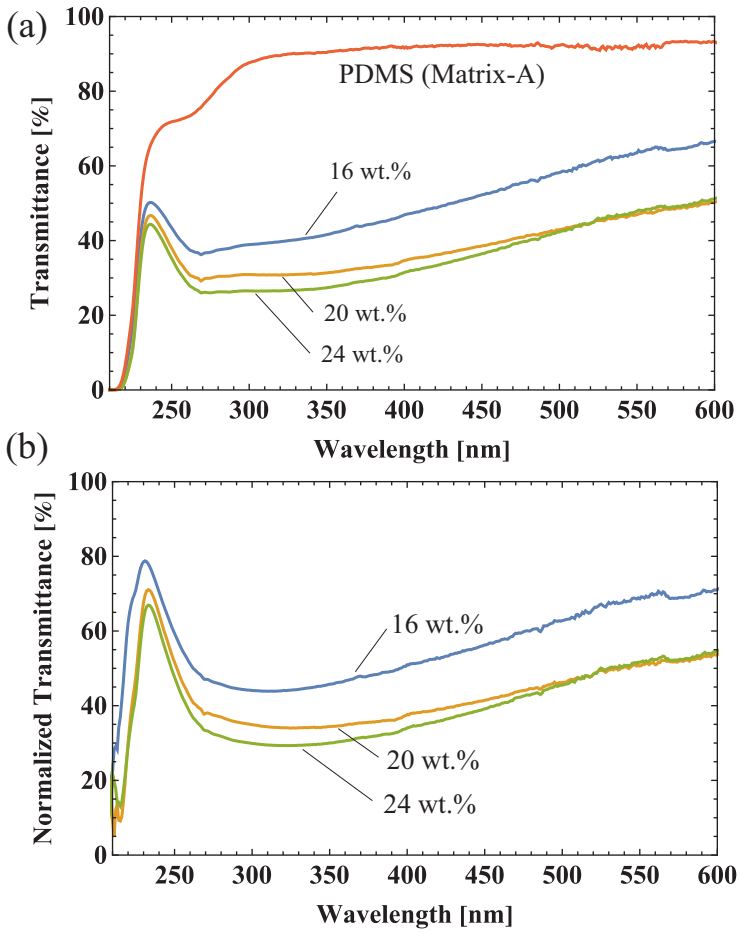

Figure 3.4: (a) Transmittance spectra of 16, 20, 24 wt.% SiO_2 dispersed in SIM-360 (matrix-A) hybrid films (1.3 mm thick); (b) Normalized transmittance spectra based on the film spectrum of the SIM-360 matrix.

3.3.2 CaF_2 dispersed PDMS sample films evaluation

CaF_2 particles are projected to have longer SRIM wavelengths than SiO_2 particles due to the smaller index difference. As shown in Table 3.1, Four different CaF_2 powders (powders I-IV mentioned in Section 2.2.2) were tested by mixing them with four different PDMS matrices. A cured film with 1.0 mm thick was used to evaluate the transmittance of the hybrid samples (SIM-360, KE-103,

Sylgard-184 matrix). However, a 1.0 mm quartz cell was used to measure the transmittance of hybrid materials with CaF_2: LMW-PDMS. Then, Figure 3.5 shows the relationship between the visible transmittance for hybrids with various dispersing concentrations. Only powder I's result indicates a transmittance peak in the UV area, which is expected. Because the produced powders II—IV include a few impurities, these powders' refractive index dispersion curve is higher than in Ref. [69]. The outcomes of the experiments back this up: Because of the somewhat bigger refractive index difference in the 500 nm range, powders II—IV samples had lower transmittance. Therefore, a slight refractive index difference might induce a significant wavelength shift, or the transparency condition can vanish, as seen in Figure 3.1. As a result, the transmittance peak in the UV area was not seen in the findings of powders II—IV. Increasing the concentration and utilizing a bigger particle size (compared to SiO_2: SIM-360 films) are effective approaches to improving spectroscopic performance. These parameters can increase the scattering cross-section and the spatial density of CaF_2, lowering the visible region transmittance. Then, peak wavelengths of 251, 259, 278, and 304 nm were obtained for samples with matrices LMW-PDMS, KE-103, SIM-360, and Sylgard-184, respectively; this order corresponds to the cut-off wavelength illustrated in Figure 3.2.

Table 3.1: Hybrid materials of CaF_2 powders dispersed in various PDMS matrices evaluation

	Concentration (wt.%)	LMW-PDMS	KE-103	SIM-360	Sylgard-184
CaF_2 powder I (fabricated)	10	86.0% (peak @ 251 nm), 26.3% (400 nm)		65.8% (peak @ 278 nm), 24.4% (500 nm)	67.0% (peak @ 304 nm) 25.0% (500 nm)
	20		68.0% (peak @ 259 nm), 4.9% (500 nm)	78.9% (peak @ 278 nm), 10.7% (500 nm)	
	30		67.8% (peak @ 259 nm), 2.5% (500 nm)	75.4% (peak @ 278 nm), 5.2% (500 nm)	
CaF_2 powder II (commercial)	5			No peak, 52.0% (500 nm)	
	10	No peak, 26.7% (500 nm)	No peak, 30.2% (500 nm)	No peak, 25.6% (500 nm)	No peak, 37.8% (500 nm)
	30			No peak, 4.4% (500 nm)	
CaF_2 powder III (commercial)	30		No peak, 0.7% (500 nm)	No peak, 0.7% (500 nm)	
CaF_2 powder IV (commercial)	10			No peak, 17.8% (500 nm)	No peak, 26.9% (500 nm)
	30			No peak, 0.9% (500 nm)	

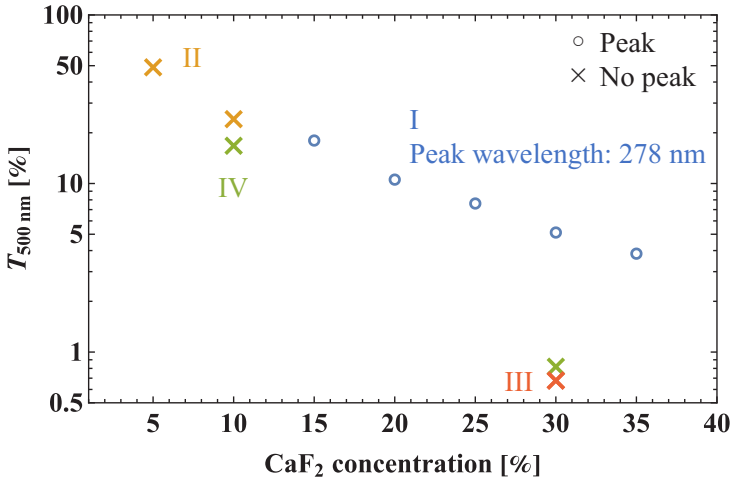

Figure 3.5: Experimental results of various CaF_2 materials. i: powder I dispersed in SIM-360 film at 15, 20, 25, 30, and 35 wt.%; ii: powder II dispersed in SIM-360 film at 5, 10 wt.%; iii: powder III dispersed in SIM-360 film at 30 wt.%; iv: powder IV dispersed in SIM-360 at 10, 30 wt.%

In Figure 3.6(b) and (d), pictures of CaF_2: PDMS hybrid film samples made by CaF_2 powder I and SIM-360/ KE-103 confirm that a concentration of 30 wt.% and a thickness of 1 mm are appropriate for scattering visible light. It could be owing to greater size of CaF_2's particle.

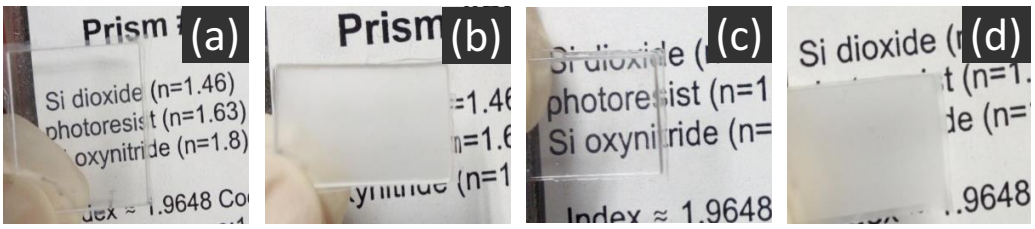

Figure 3.6: The sample images with 1.0 mm thickness: (a) SIM-360 (b) 30 wt.% CaF_2 in SIM-360 (c) KE-103, and (d) 30 wt.% CaF_2 in KE-103

The transmittance spectra of CaF_2: SIM-360 films made with 15, 20, 25, 30, and 35 wt.% CaF_2 concentrations are shown in Figure 3.7. The raw spectra are shown in Figure 3.7(a), and the observed error at 220 nm is 0.54 percent. The normalized spectra of theCaF_2: PDMS film with different concentrations are shown in Figure 3.7(b). The raw spectra's peak wavelength slightly shifted to 278 nm because of the influence of PDMS absorption, whereas Figure 3.7(b) showed a relatively stable transparent peak wavelength about 275 nm.

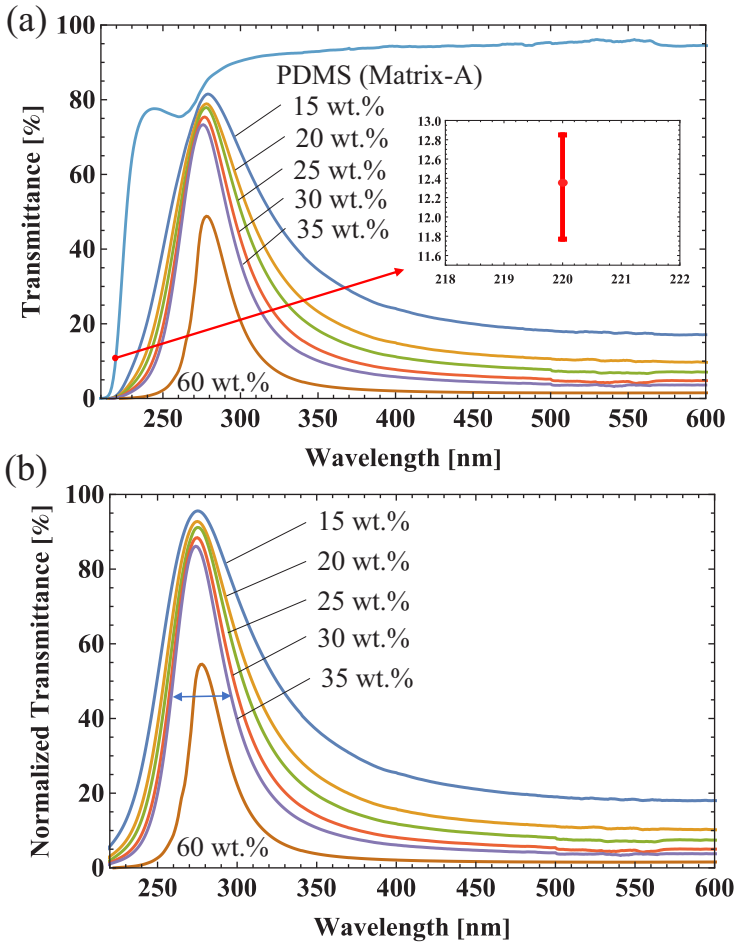

Figure 3.7: (a) CaF_2: SIM-360 1.0 mm thick hybrid films transmittance spectra, sample concentrations: 15, 20, 25, 30, 35, and 60 wt.%; (b) Normalized transmittance spectra based on pure SIM-360 film transmittance

As shown in Figure 3.7(b). 90-95 % peak transmittances, and less than 20 % visible transmittances were obtained, respectively. With increased CaF_2 concentration, the effective bandwidth shrank. 40 nm effective bandwidth (full width at half maximum, FWHM) was obtained when the CaF_2 concentration is 35 wt.%. This means that around 45 % 255 nm wavelength light can transmit through the film, indicating inadequate spectroscopic performance. Hence, raising the concentration improves spectroscopic performance effectively because the concen-

tration can regulate the spatial density CaF_2 particles (35 wt.% corresponds to 14.7 vol.%). Nevertheless, a high-concentration sample is more difficult to make, because of the higher viscosity of SIM-360. Despite this, a CaF_2: SIM-360 hybrid film with a 60 % concentration still was fabricated using an existing technique. Figure 3.7 depicts the outcome. The normalized spectrum yielded a bandwidth of 28 nm and visible transmittance of 1.5 %. However, scattering causes a 50 % loss at the SRIM wavelength (transmittance peak). The loss reason will be discussed in Section 3.3.3. As a result, higher concentration should be accompanied by a better fabrication technique. After that, by changeing the PDMS matrix form, the different hybrid samples transmittance were fabricated. They are CaF_2: KE-103 hybrid films with 0, 20, 30 wt.% concentration; CaF_2: Sglgard-184 hybrid films with 0, 10 wt.% concentration; and CaF_2: LMW-PDMS uncured sample with 0, 10 wt.% concentration respectively. The raw transmittance spectra of these hybrid samples are shown in Figure 3.8. The hybrid samples with matrices LMW-PDMS, KE-103, and Sglgard-184 had peak wavelengths at 251, 259, and 304 nm, respectively.Moreover, after normalizing the spectrum of Figure 3.8(a), the narrowest effective bandwidth—28 nm was obtained at this stage (at 30 wt.% concentration). By altering the PDMS matrix, the 260 and 280 nm goal wavelengths for DNA/protein measurement were achieved, and the obtained wavelengths were 259 and 278 nm, respectively.

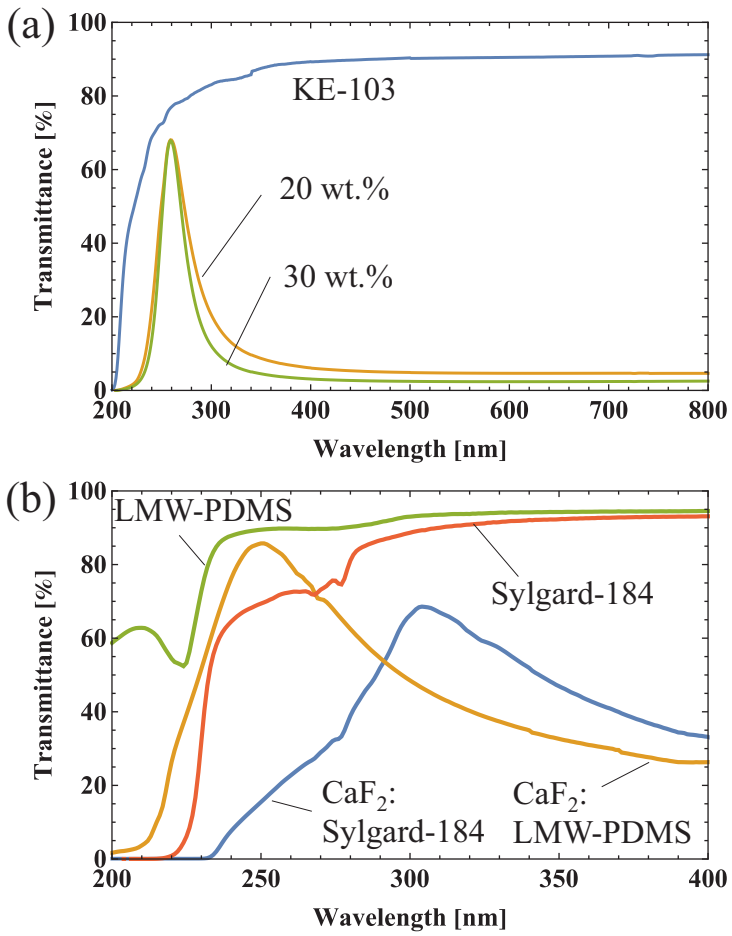

Figure 3.8: (a) 1.0 mm thick CaF_2: KE-103 hybrid films transmittance spectra. The concentrations of CaF_2 ranged from 0 to 30 wt.%; (b) 1.0 mm thick hybrid films transmittance spectra of CaF_2 in PDMS with Sylgard-184 (film) and LMW-PDMS (uncured sample). The concentrations of CaF_2 ranged from 0 to 10 wt.%

3.3.3 Transmittance loss discussion

Although we show that four different CaF_2 and PDMS combinations can be transparent at SRIM wavelengths (peak wavelengths), the peak transmittance of the normalized transmittance spectra is not 100 %. It can be caused by scattering from (i) microbubble residues during PDMS curing, (ii) internal micro-cracks

and grooves in fabricated particles, (iii) inhomogeneous distribution of refractive index due to the presence of low molecular weight siloxanes in PDMS, and (iv) the difference in refractive index between the matrix and particle's imaginary part. Despite the de-bubbling procedures being performed three times in sample production, the removal performance was restricted by the viscosity and curing time, as demonstrated in Figure 3.3 and Table 3.2.

Table 3.2: Four types of PDMS matrices have different properties

PDMS Matrices	Property	Curing condition (℃)	Workable time (mins)	Viscosity (Pa•s)
SIM-360	Low molecular weight siloxane (<200ppm)	23℃, 48h (150℃, 2h)	100	7
KE-103	Low viscosity model	23℃, 72h	180	1
Sylgard-184	Mixed low molecular weight siloxane	25℃, 48h	90	3.5
LMW-PDMS	Low viscosity (liquid)			Low

Then, the above four arguments can be stated in more depth as follows. (i) The CaF_2: PDMS films optical microscopic image in Figure 3.9(a) confirms the presence of residual bubbles. (ii): Figure 3.9(b) shows a scanning electron microscopy (SEM) image of powdered CaF_2 powder, which reveals numerous submicron grooves and cracks. It appeared that filling these grooves with a viscous PDMS matrix was too harsh. (iii): It appeared to be because of the PDMS purity. SIM-360 was purified by eliminating low molecular weight siloxane; using SIM-360, scattering due to (iii) could be reduced, whereas using KE-103, it could be increased. (iv): Because the scattering increases when the peak wavelength approaches the matrix's cut-off wavelength, the scattering is larger in the CaF_2 & Sglgard-184 and SiO_2 & SIM-360 combinations. From normalized transmit-

tance measurements of 15—35 wt.% CaF_2: SIM-360 samples, Figure 3.9(c) shows maximum transmittance at peak wavelength. The large scattering of maximum transmittance indicates that (i) may be the main scattering, which could be improved by optimizing the fabrication procedure. In addition, by lowering the scattering of (ii)—(iv), the upper limit of maximal transmittance can be enhanced. To improve (ii), the CaF_2 particle surface smoothing process can be considered by acid. Furthermore, optimization of (iii)—(iv) can be left out for now due to the scattering owing to (iii)—(iv) caused a transmittance loss less than 10 %.

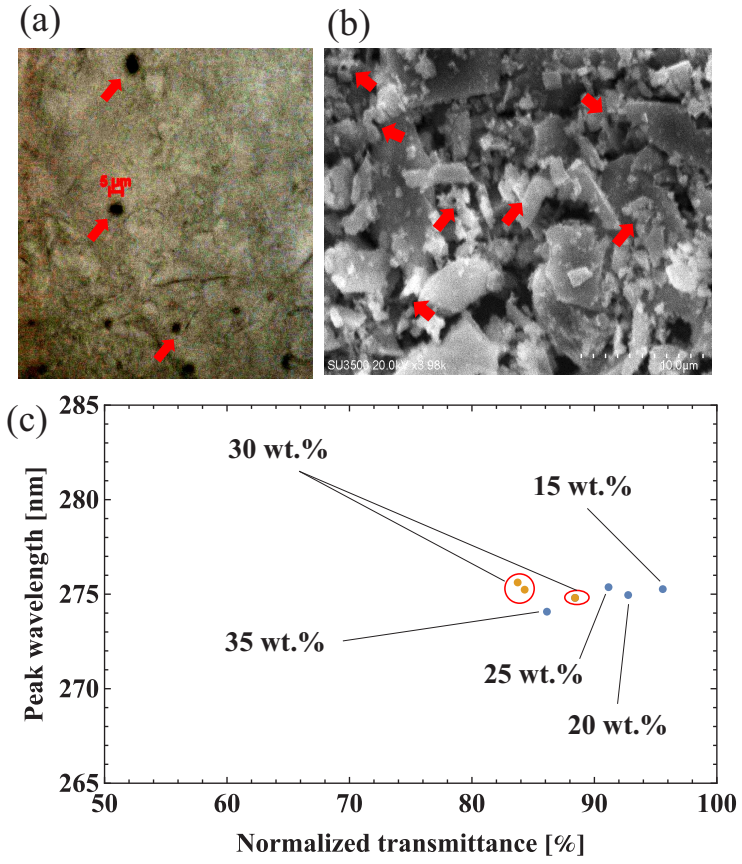

Figure 3.9: (a) 30 wt.% CaF_2: SIM-360 optical microscope image (measured by ECLIPSE TE2000-U, Nikon); (b) CaF_2 powder I scanning electron microscope image (measured by SU3500, Hitachi); (c) The maximum transmittance at peak wavelength from normalized transmittance measurement of 15—35 wt.% CaF_2: SIM-360 samples

3.3.4 CaF_2 particle size distribution evaluation

The SRIM wavelength was established by the type of PDMS matrix used in the previous sections. Whereas the spectroscopic performance of the scattering films is deemed insufficient for the next application. Apart from concentration, more elements that affect effective bandwidth should be considered: the particle size and dispersion of CaF_2 particles are the two elements. The microscopic picture

of the CaF_2 powder I (1 wt.%) dispersed in the H_2O sample is shown in Figure 3.10(a). The particle size distribution according to its statistics is shown in Figure 3.10(b). The most common particle size was 0.1 to 10 μm, and the particle size distribution may be fitted with a log-normal distribution, as indicated in equation 3.1:

$$\frac{1}{\sqrt{2\pi}x\sigma}e^{\frac{(-\mu+Log(x))^2}{2\sigma^2}} \ (x > 0) \tag{3.1}$$

, where -1.05 and 1.53 are used to fit the μ and σ, respectively.

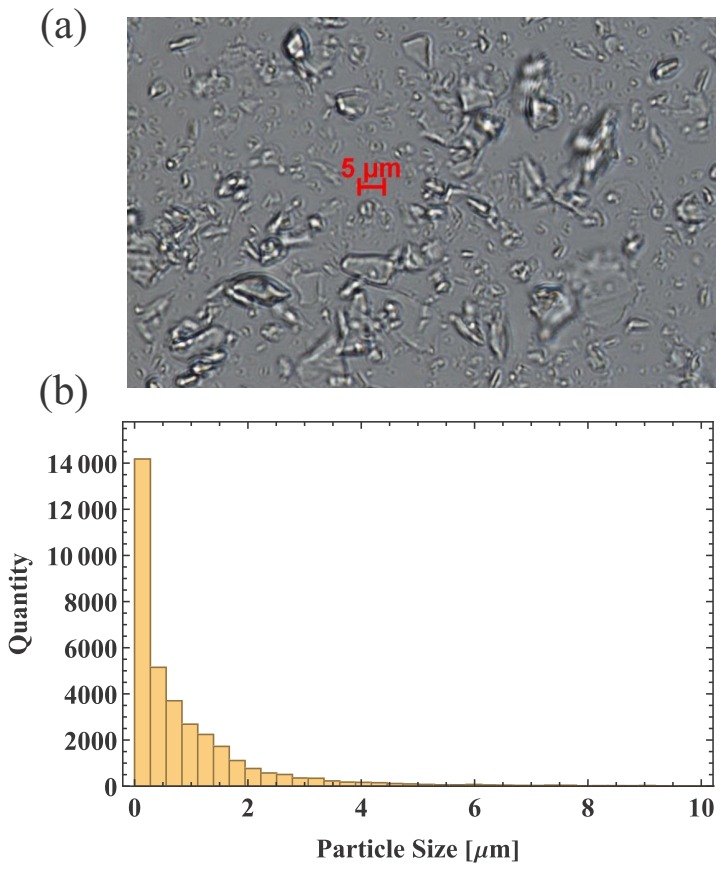

Figure 3.10: (a) optical microscope graph of CaF_2 powder I dispersing into H_2O sample (concentration of CaF_2: 1 wt.%) (measured by ECLIPSE TE2000-U, Nikon); (b) CaF_2 particle size distribution calculated from 16 pictures taken under various shooting conditions

3.3.5 The sample film's scattering property

The particle size and dispersion of the CaF_2 (powder I) is the other 2 parameters influenced the effective bandwidth. It is necessary to construct a calculating model to guide future research. Because controlling the particle size and dispersion of the ground CaF_2 particles is difficult in the current production method. Therefore, the scattered light distribution at different wavelengths was measured to confirm the scattering pattern. The properties of the visible area transmitted light was measured based on the setup illustrated in Figure 3.11(a). A CaF_2: SIM-360 hybrid film (1.5 mm thick) was placed next to the DPSS laser light source. An oscilloscope (TDS680B, Tektronix) was used to detect the transmitted and scattering light. Figure 3.11(b) shows the profile of scattering light at a wavelength of 532 nm. The incident light was scattered in the visible range, and Mie scattering (Hulst approximation, described in Section 2.4.2) could be considered in this region. The properties of UV area transmitted light were also measured, and the setup is illustrated in Figure 3.12(a). A UV LED was employed as the light source, and a 1-mm-diameter pinhole was used to fix the CaF_2: SIM-360 (1.0 mm thick). A fiber-coupled spectrometer was utilized to measure the transmitted and scattering light (HR-4000, Ocean optics). The profile of scattering light at a wavelength of 300 nm is shown in Figure 3.12(b). Due to the refractive index difference between CaF_2 and PDMS in this region being small, incoming light was almost not dispersed in this range. Hence, the RGD scattering (RGD model, described in Section 2.4.1) [79], rather than Mie scattering, should be considered.

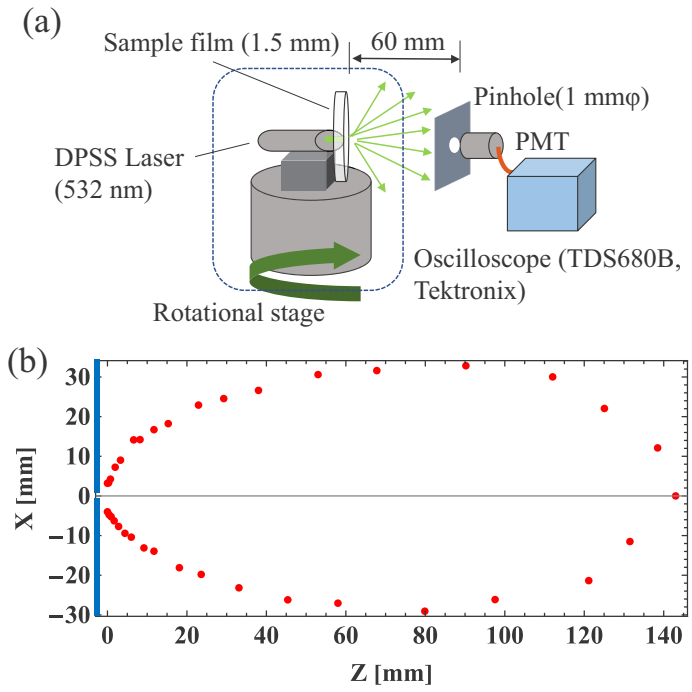

Figure 3.11: (a) Measurement setup of the scattering profile in the visible light area; (b) Visible scattering profile (CaF_2: SIM-360 with 30 wt.% concentration, 532 nm incident light)

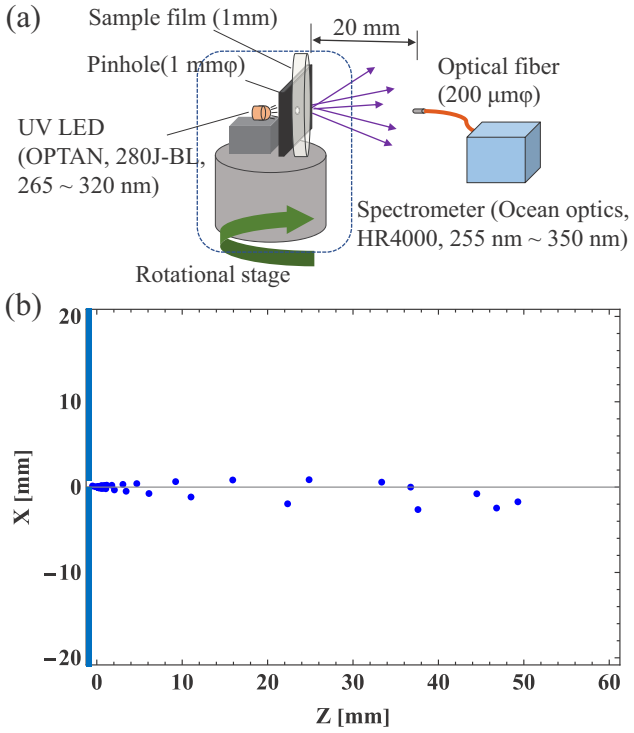

Figure 3.12: (a) Measurement setup of the scattering profile in the UV light area; (b) CaF_2 scattering profile in the UV area (CaF_2: SIM-360 with 30 wt.% concentration, 300 nm incident light)

3.4. RGD-Hulst model simulation results

According to the principle of RGD and Hulst approximation in Section 2.4, a hybrid scattering model with RGD and Hulst model has been developed, and the calculation model can be switched from the RGD model to the Hulst model using the phase delay φ (the specific construction process will be discussed in Section 6.1). As a result, the transmittance spectra of light transmitted through a 1 mm-thick sample film (CaF_2: SIM-360) were calculated using the mixed scattering model. It is based on the experimentally measured CaF_2 particle distribution and

the fitted refractive index dispersion. Then, the experimental data fitting result was shown in Figure 3.13(a). The simulation curve is in excellent agreement with the experimental data from the wavelength 240 nm to 310 nm. However, they still have some disagreement in the visible region, where the simulated result is slightly lower than the experimental results. Because the RGD-Hulst model cannot calculate the distribution of scattered light, the detailed reasons will be discussed in Section 6.1. Indeed, it is sufficient for assessing effective bandwidth and improving spectroscopic performance. As a result, as shown in Figure 3.13 (b), the calculated bandwidth values also be fitted with our experimental results. These findings were also highly consistent.

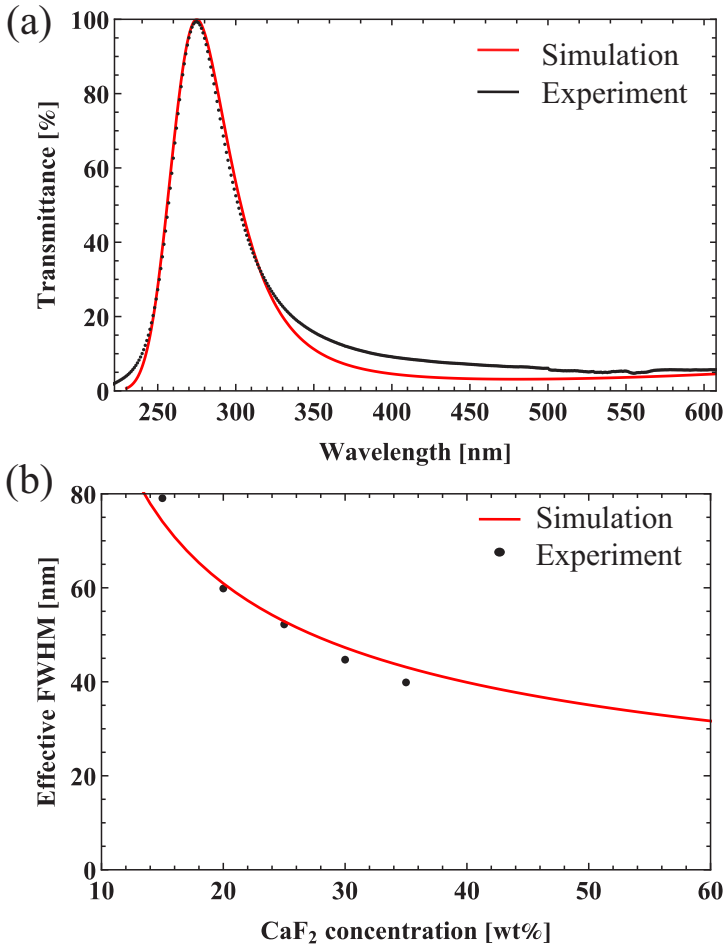

Figure 3.13: Fitting results of RGD-Hulst hybrid model simulation and experiment. (a) Simulation conditions: CaF_2: SIM-360, thickness: 1 mm, concentration: 30 wt.%, particle diameter and distribution: CaF_2 powder I, (b) calculation conditions: CaF_2: SIM-360, thickness: 1 mm, concentration: 10–60 wt.%, particle diameter and distribution: CaF_2 powder I. The bandwidth (effective FWHM) calculated based on the spectra of 1 mm thick CaF_2: SIM-360 with the concentration of 15—60 wt.%

Then, different particle sizes and distributions were simulated using a log-normal distribution and imported into the hybrid model to estimate the transmittance bandwidth of the hybrid film for different particle and distribution cases. The estimation results are shown in Figure 3.14. Here, (a) depicts the bandwidth

effect of varying particle size distributions (in the same mean particle size of 1 μm). (b) shows how the bandwidth changes as the average particle size changes (in the same distribution). The simulation curves in Figure 3.14 clearly show that, in addition to the concentration, particle size and distribution of CaF_2 are crucial for bandwidth improvement. CaF_2 powder with a larger particle size and narrower distribution is required to improve the spectroscopic performance of scattering hybrid filters. When the average particle size of CaF2 is 10 mum, concentration is raised to 50 wt.%, and have the same particle size distribution with experiment, a bandwidth of 10 nm could be predicted. Therefore, there is room for improvement in the spectroscopic performance of the hybrid material, particularly in terms of controlling the size and distribution of CaF_2 particles and building a comprehensive scattering model by including multiple scattering calculations considering the Monte-Carlo theory, which will be discussed in the following chapters.

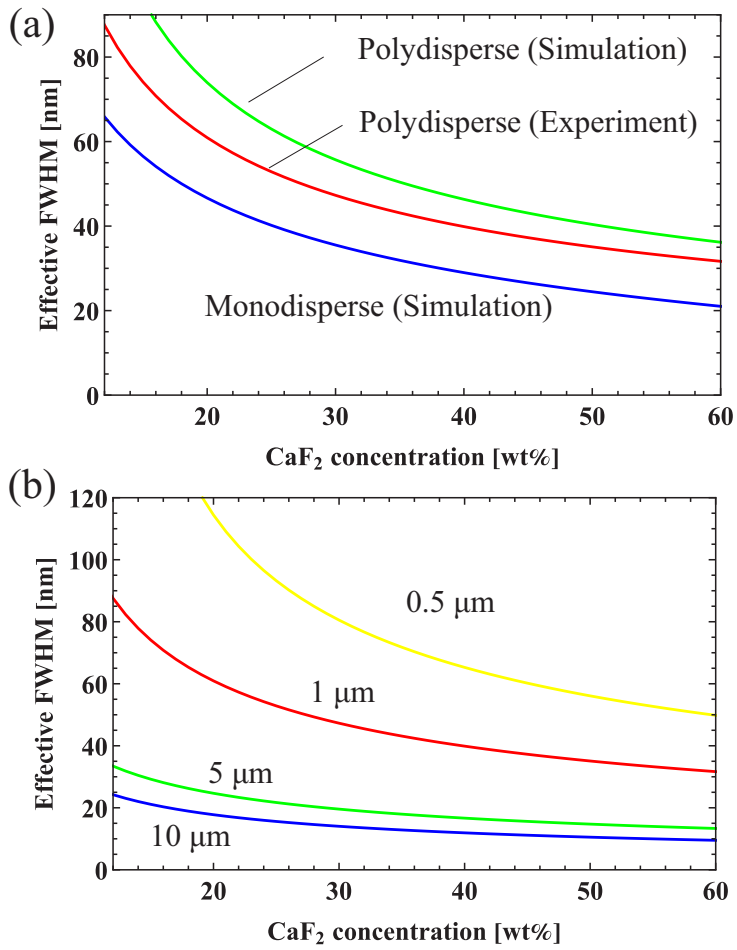

Figure 3.14: Calculated results of spectroscopic properties for different particle sizes and distributions (or experiments) based on lognormal distribution simulations; simulation conditions: (a) CaF_2 mean particle size: 1 μm; monodisperse particles standard deviation is 0 μm (simulation); polydisperse particles standard deviation is 3.4 μm (experiment); polydisperse particles standard deviation is 9.0 μm (simulation); (b) particle distribution standard deviation is 3.4 μm, average particle sizes are 0.5—10 μm

3.5. Conclusions

In terms of experimental results, this chapter developed and demonstrated novel organic/ inorganic hybrid materials with UV spectroscopic function based on the SRIM concept. It is fabricated by mixing the PDMS matrix and CaF_2 particles. The 15 wt.% CaF_2: SIM-360 sample resulted in a high transmittance of more than 95 %, and the effective transmittance bandwidth is 28 nm for a 1 mm thick sample with 60 wt.% dispersion. Moreover, transparent peaks at 251, 259, 278, and 304 nm were obtained, respectively, by using different PDMS matrices (LMW-PDMS, KE-103, SIM-360, and Sylgard-184), and the order of peak wavelength agree with the cut-off wavelength order of PDMS matrices. In terms of simulation results, numerical calculations model based on RGD and Huslt approximations apply to the 240—310 nm region. Also, the RGD-Hulst model suggests that, except for increasing concentration, the effective transmittance bandwidth can be narrowed by narrowing the particle size distribution and increasing the mean particle size of CaF_2. In other words, increasing the scattering cross-sectional area and spatial density per unit thickness can effectively improve the spectroscopic performance. Although the RGD-Hulst calculation model can predict effective transmittance and spectroscopic properties, it cannot explain the distribution of scattered light. Therefore, it still needs to be further improved.

Chapter 4

Fabrication and modeling of tunable UV bandpass filtering hybrid materials with multiple dispersing

4.1. Introduction and purpose

In the previous chapter, the SRIM-based principle developed transparent scattering materials at specific wavelengths in the UV region. It possessed certain bandpass spectroscopic properties by dispersing inorganic CaF_2 particle materials into organic PDMS materials. Then, in this chapter, we will focus on the tunability of UV transparent wavelength. The UV wavelengths that can transmit our spectroscopic scattering materials are often used for inactivation work on specific biological bacteria or viruses [93–101] in low-cost point-of-use (POU) water purification [102–109]. However, considering that the UV wavelengths that can effectively inactivate them differ for different biological bacteria or viruses. Moreover, the general UV light source emission spectrum has a certain line width. When using the specific wavelength of the UV light source sterilization, to avoid other wavelengths light harm the biological samples. Hence, a deep UV bandpass filter with a certain peak wavelength tunability is needed. In general, this class of bandpass filters is fabricated in many ways, such as vacuum deposition [84], nanoimprint lithography [85], crystal growth processing [110], focused ion beam (FIB) milling [111–113], inkjet-printing [114], and other innovative methods used to produce various filters reported. However, the cost of filters made using these processes is high because most of these manufacturing processes are complex. Furthermore, these filter devices' various inherent properties, such as incident light angle dependence, surface polishing treatment, and persistent mechanical strength, limit the flexibility of device applications. Therefore, low-cost filter devices limited by fewer usage scenarios are necessary. The spectroscopic diffusion materials that our research team developed meet exactly these requirements. Hence, this chapter measured samples' stabilities and transmittance spectra (CaF_2-dispersing PDMS hybrid films) with varied film thicknesses. Changes in the SRIM wavelengths were

studied with various environmental perturbations such as temperature and strain. Changes in total diffusion angles were determined experimentally by evaluating the scattering intensity distributions of film samples at different incident light wavelengths. Then, the SRIM wavelengths tunability of hybrid materials were successfully exhibited by dispersing low-molecular-weight PDMS (LMW-PDMS) and CdSe/ZnS colloidal quantum dots (CQDs). In addition, the construction of an RW model was completed based on the measured total diffusion angle results. The construction of this model not only compensates for the shortcomings of the RGD-Hulst calculation model that cannot simulate the scattered light distribution but also extends the wavelength range of effective transmittance that can be simulated.

4.2. Fabrication process of the hybrid films

The manufacturing of CaF_2 dispersed PDMS hybrid films is demonstrated in Figure 4.1. CaF_2 molding materials (high-purity, OKEN) were ground using a diamond drill with an electric router to produce CaF_2 powders with micro and nanoparticles (powder V in Table 2.2). The CaF_2 particles were mixed with the SIM-360 matrix using a mixer at the speed of 1440/1440 rpm (revolution/autorotation) for 200 seconds. Mixing was performed four times to aid in the dispersion these CaF_2 particles. The mixture was then injected with a curing agent (CAT-360, Shinetsu Chemical) and mixed for 90 seconds at 1440/475 rpm. Then, the vacuum oven was used to remove air bubbles from the hybrid PDMS solution before molding. The UV bandpass flexible filter could be obtained by injecting the hybrid solution into the mold, covering a PMMA plate once, curing at 50 $°C$. CdSe/ZnS colloidal quantum dots (CQDs, 8 nm diameter, Mesolight) or LMW-PDMS as additional dispersants might be added to the aforementioned

SIM-360 matrix before adding the particles of CaF_2 to achieve the tunability of SRIM wavelength (also tune transmittance wavelength). Finally, flexible and tunable UV bandpass filters were effectively constructed by varying the types and amounts of dispersants.

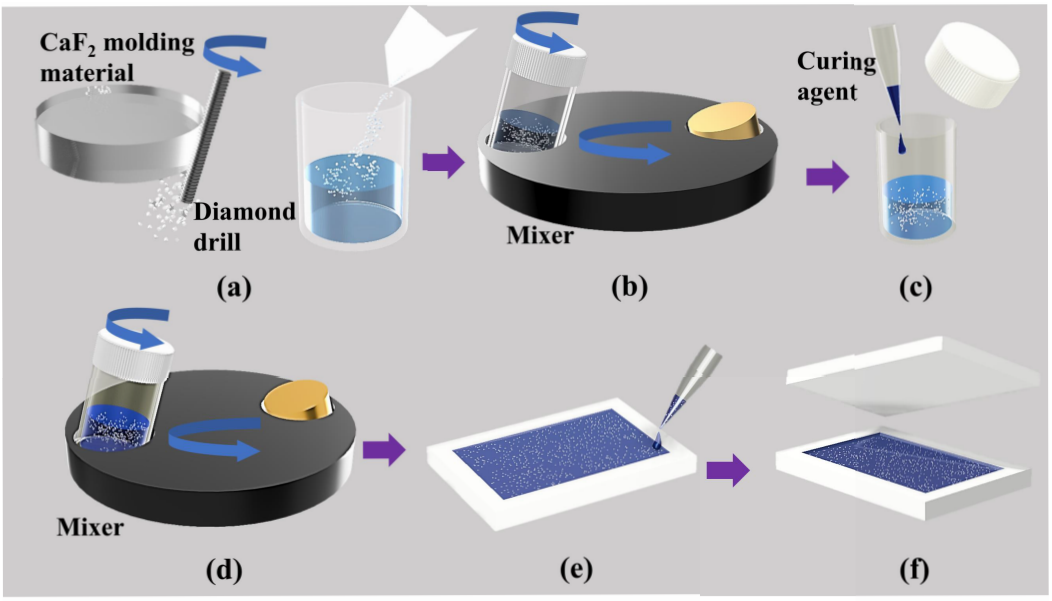

Figure 4.1: CaF_2 dispersed PDMS hybrid film fabrication processes. (a) Fabrication and dispersion of CaF_2 particles in a PDMS, (b) homogenous mixing of PDMS solutions containing LMW-PDMS or CQDs with CaF_2 particles, (c) the curing agent was added to the hybrid, (d) air bubble removal and mixing of the hybrid solution, (e) the hybrid solution is injected into a mold, (f) to cure the film after being covered with a PMMA plate

4.3. Experimental results and discussions

4.3.1 UV spectrum properties of CaF_2 dispersed PDMS hybrid films

As indicated above, three sample films (CaF_2: SIM-360) with 0.3 mm, 0.7 mm, and 1.1 mm thick were manufactured. Figure 4.2(b) shows the normalized transmittance spectra of the film after removing the absorption of the pure SIM-360 matrix (the transmittance spectra were measured using a spectrophotometer (JASCO, V-630)). The filters have more than 90 % transmittance at 271.5 nm (0.5 nm), which is a difference of several nanometers from the SRIM wavelength of the same matrix hybrid scattering material developed in the last chapter (also in our earlier study [60]). Because the previous powder-making process is more likely to mix impurities, resulting in changes in the refractive index of the matrix. As with the transmittance spectra of the samples in the previous Section 3.3.1. Low scattering around SRIM wavelengths caused significant UV transmission. The decreased visible transmittance is owing to higher scattering generated by about 0.02's refractive index difference in the visible light area. The data provided in Figure 4.2(a) can also explain this phenomena. After passing through a sample with 1.1 mm thickness, some representative scattered profiles were captured and presented on a white paper screen under varied wavelengths of incident light (produced by a femtosecond laser, Spectra Physics). When the incident light wavelength is more than 400 nm, the profiles of scattered light rapidly evolve into circles because of the intense scattering generated by the constantly increasing difference of refractive index. Only minor RGD scattering was observed around the 272 nm area, where the refractive index difference here is negligible [60, 79]. As a result, most UV lights with wavelengths approaching the SRIM wavelength

and a part of other wavelengths lights entered the spectrophotometer's detector at a specific acceptance angle, causing a bandpass transmittance phenomenon, as shown in Figure 4.2(b). Because of increased light scattering, the hybrid film's effective bandwidth reduced from 168 nm to 60 nm as the thickness rose. This is because, based on the Beer-lambert theorem, the transmittance corresponding to non-SRIM wavelengths decreases as the thickness increases.

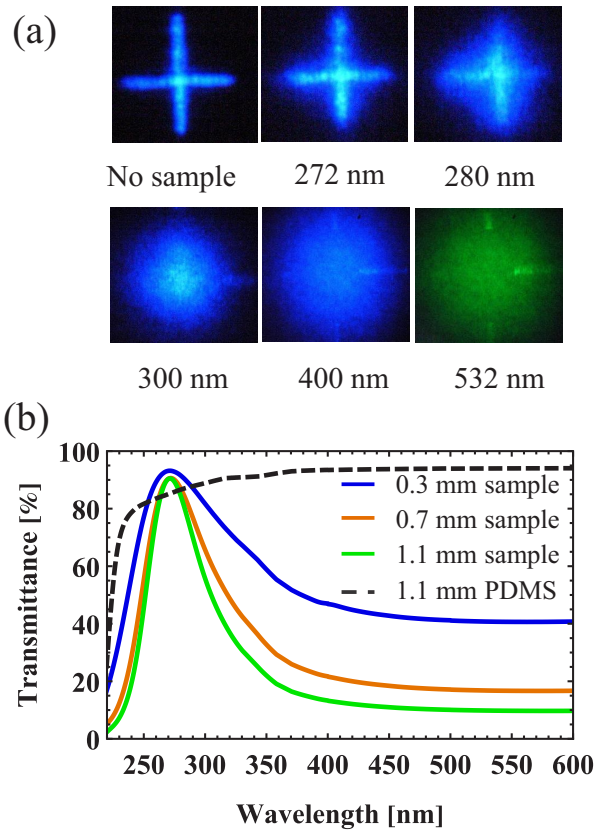

Figure 4.2: (a) Spatial scattering intensity profile with different input light wavelengths (When the cross optical spot through the 1.1 mm thick sample film); (b) 0.3, 0.7, and 1.1 mm thick hybrid films normalized transmittance spectra, they are fabricated by dispersing 30 wt.% CaF_2 particles in the PDMS matrix; and a 1.1 mm thick pure PDMS film transmittance spectra (SIM-360, cured for 28 hours)

Then, as shown in Figure 4.3, the different film thickness filter's peak wavelengths were recorded with the change of curing time. It is derived that the filter's peak wavelengths tend to stabilize after 28 hours of cure time. The PDMS molecules were not entirely cross-linked in the early curing process, and the residual crosslinker has an absorption around 240—280 nm UV area. The transmittance spectra of the PDMS film at various curing times were tested to demonstrate this consider, as shown in Figure 4.4. Figure 4.4 shows how the transmittance spectra of the PDMS film evolve with curing time at a temperature of 50 $°C$. The cross-linking of some PDMS molecules was not completed after 4 hours of curing, resulting in relatively high UV light absorption in the 240—280 nm region. The absorption of the film in this range decreased as the PDMS was fully cured. Finally, when the cure duration was more than 28 hours, the transmittance spectrum of the PDMS film tended to remain steady. As a result, compared to the fully cured sample, the CaF_2: PDMS film peak wavelength redshifted during the early curing process. With increasing curing time, the actual peak wavelengths of the various samples were nearly all kept at around 272.5 nm (about 271.5 nm after subtracting the PDMS absorption). Furthermore, consistent peak wavelengths show that tiny thickness adjustments in the PDMS films have little effect on the filter's peak wavelength.

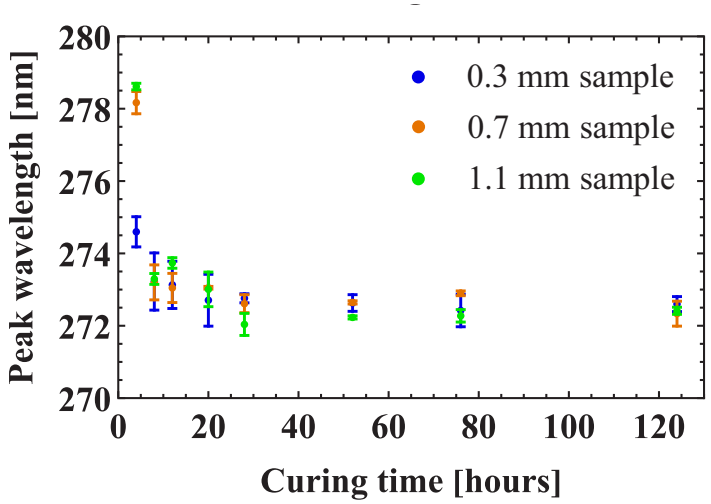

Figure 4.3: The change in the peak wavelength of the filters as the curing time increases

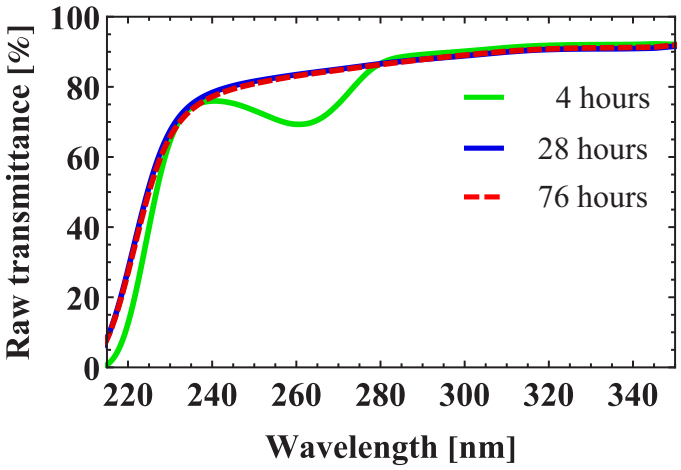

Figure 4.4: The 1.1 mm thick PDMS (SIM-360) films transmittance spectra at various curing phases

4.3.2 Properties of CaF_2 dispersed PDMS hybrid films at temperature and strain dependence

Considering the practicality and versatility of CaF_2: PDMS hybrid films as UV bandpass filters, it's important to investigate how the filters respond to strain and temperature variations. Figure 4.5 displays a spectrophotometer, a homemade heater, and strain measurement instrument used to examine fluctuations in the UV spectrum properties of the filters. As shown in Figure 4.6(a), heating the sample from 25 to 35 degrees Celsius causes the filter peak wavelength to shift by around 15 nm. Temperature dependency is basically the same in hybrid films of various thicknesses. The PDMS's thermo-optic coefficient is primarily responsible for the peak wavelength blueshift as temperature rises. Because the PDMS's negative thermo-optic coefficient ($-4.5 \times 10^{-4}\,°C^{-1}$) [115,116], which is one order higher than CaF_2 ($-1.27 \times 10^{-5}\,°C^{-1}$) [117]. Hence, the PDMS matrix dispersion curve decreases more as temperature rises, resulting in the cross-point of the CaF_2 and PDMS blueshifted, as shown in Figure 4.6(b). The PDMS matrix dispersion curve was simulated by Sellmeier equation [67,118–120], and the CaF_2 dispersion curve was derived from literature [69]. The 1.5 nm $°C^{-1}$ experimentally observed curve slope indicates the filter's temperature response. This is similar to the simulated results of 1.9 nm $°C^{-1}$. Moreover, the different thicknesses filter's peak wavelength shifts within 12 % stretching ratios (interval of 2 %) were evaluated to reveal the stability of the filter during the deformation process, as shown in Figure 4.7. It can be shown that as the stretching ratio is increased, the filter's peak wavelength does not change significantly. The stability of deformation is beneficial in extending the UV bandpass hybrid material's applications.

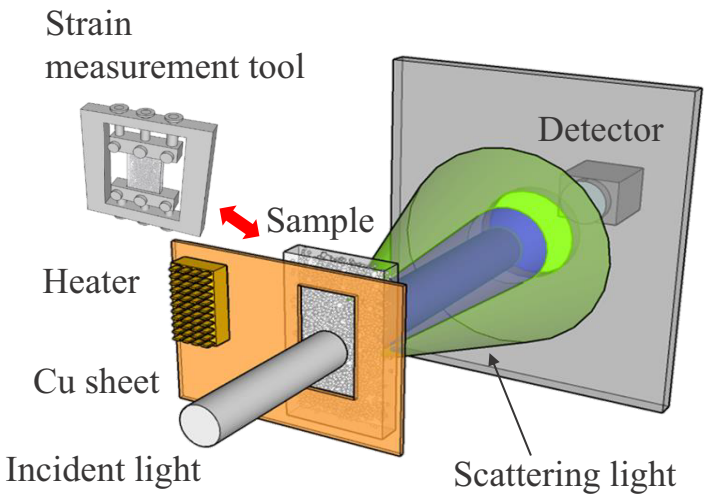

Figure 4.5: Measurement setup of the strain and temperature response characteristics of CaF_2-dispersed PDMS hybrid films

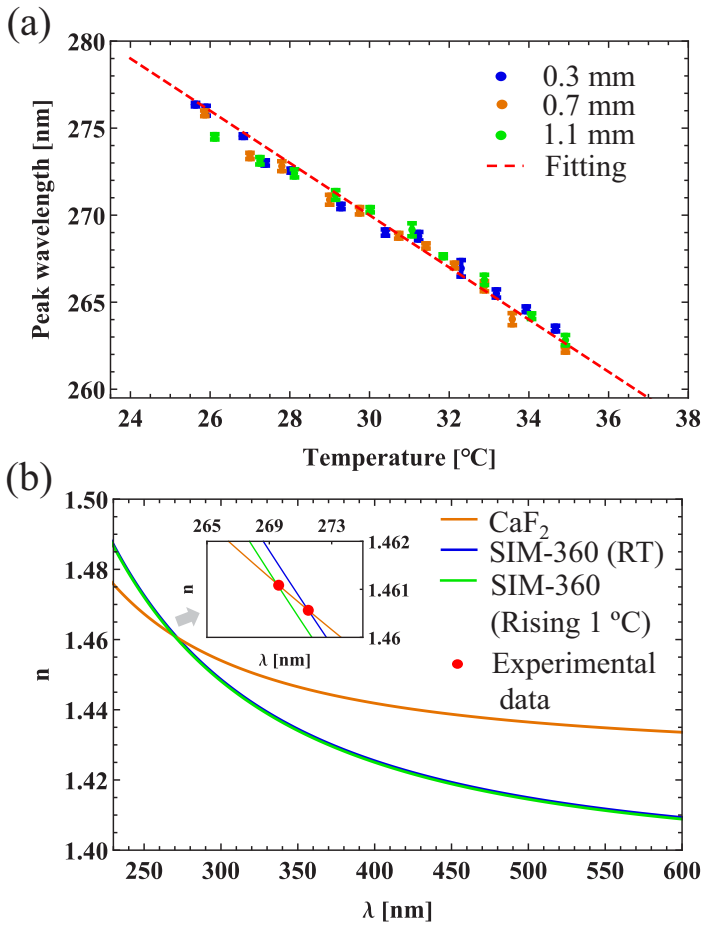

Figure 4.6: (a) The temperature-dependent of the various thicknesses samples peak wavelengths; (b) Numerical simulation of CaF_2 [69] and PDMS refractive index dispersion (SIM-360). The blueshift of the PDMS matrix's dispersion curve corresponding to a 1 $°C$ temperature change is shown in the inset

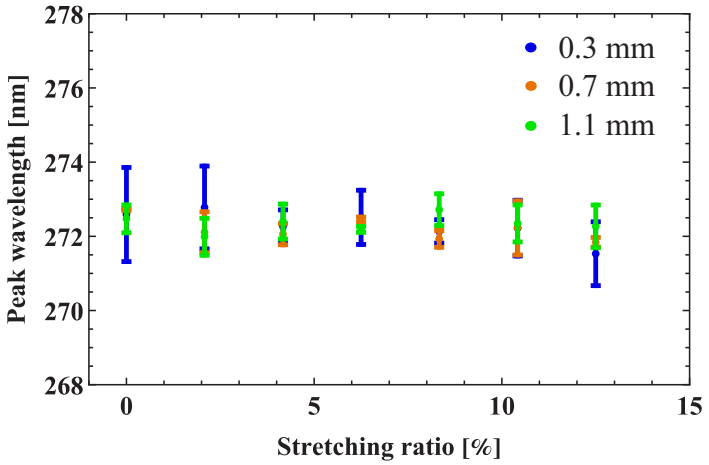

Figure 4.7: Strain affected the peak wavelengths of various thicknesses samples

4.3.3 Scattered light distribution measurement and simulation results based on random walk scattering model

The random walk (RW) scattering model was built to simulate the scattering light of CaF_2:PDMS hybrid films, according to the theory in Section 2.5 and the specific construction process in Section 6.2.1. The total diffusion angles after the different wavelengths of incident light pass through the hybrid film were measured as an essential input parameter of the scattering model before executing the simulation of UV filtering capabilities. A femtosecond laser was employed in our research to provide varied incident light wavelengths. A conversion screen was used to gather scattered light in a specific angle range when light from a slit (d = 0.2 mm) passed through a CaF_2: PDMS sample. The spatial intensity distributions of scattered lights were recorded using a charge-coupled device (CCD) camera, as shown in Figure 4.8(a). The normalized total diffusion angles of sample film were calculated based on the scattered light distribution along the direction perpendicular to the slit, and the results showed in Figure 4.8(b). The

exact computational process is described in the following.

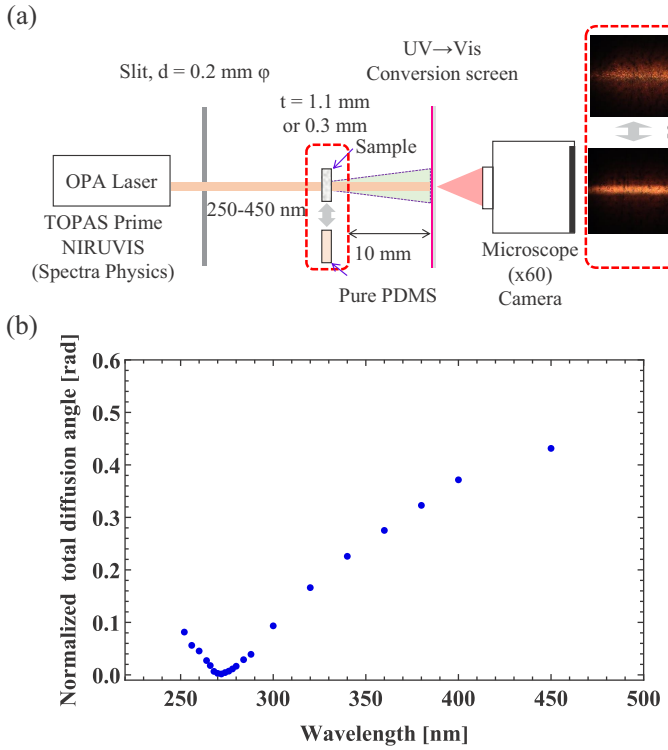

Figure 4.8: (a) Diagram of the measuring setup for determining the hybrid film's total diffusion angle; (b) The normalized total diffusion angles for the various incident light wavelengths

For example, the process of diffusion angle measurement at 278 nm is: after the slit incident light passes through the PDMS matrix and CaF_2 dispersed PDMS sample film, the scattering intensity profiles of scattered light will be acquired using the measuring setup given in Figure 4.8(a). Then, as illustrated in Figure 4.9, image processing was used to derive 278 nm light scattering intensity distributions along the direction perpendicular to the slit corresponding to the PDMS matrix and CaF_2 dispersed PDMS film sample. The double Gaussian function was applied to match the scattering intensity distribution data. It is, in fact, the superposition of two single Gaussian distributions, $N(\mu_1, \sigma_1^2) + N(\mu_2, \sigma_2^2)$,

where μ_1, μ_2, σ_1, and σ_2 denote the expectation and standard deviation of the two single Gaussian distributions, respectively. $\sigma_{PDMS1} \approx \sigma_{sample1}$ was used in the fitting process to calculate the relative diffusion angle of the scattering light. The following equation 4.1 was used to compute the total diffusion angle:

$$2 \times \tan^{-1}\left(\frac{2.355 \times \sqrt{\sigma^2_{sample2} - \sigma^2_{PDMS2}} \times L1}{2 \times L2}\right) \tag{4.1}$$

, where σ_{PDMS1} and σ_{PDMS2} are the standard deviations of two single Gaussian distributions of scattered light passing through the PDMS matrix, $\sigma_{sample1}$ and $\sigma_{sample2}$ are the standard deviations of two single Gaussian distributions of scattered light passing through the sample film, L1 is the pixel size, and L2 is the distance between the sample and the screen. The normalized total diffusion angle distribution was obtained by dividing the square root of the sample thickness at different incident light wavelengths.

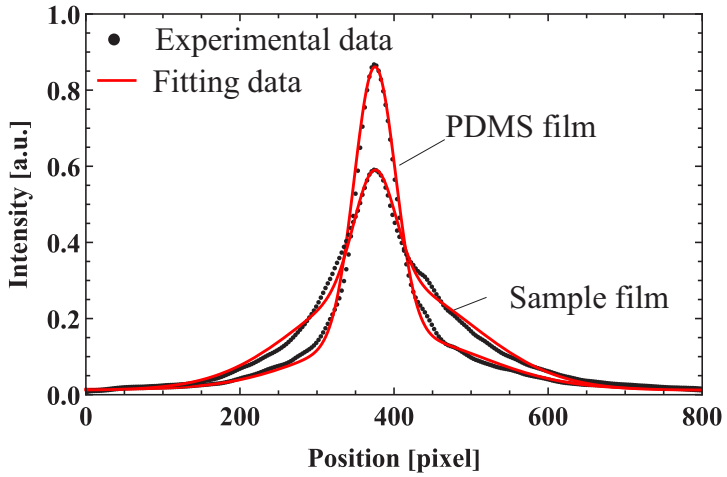

Figure 4.9: Relative intensity distributions of 278 nm scattered light passing through PDMS matrix or CaF_2-dispersed PDMS sample films (1.1 mm) and results of double Gaussian fitting (R^2 >0.999). A pixel is equal to 4 μm in length

Then, according to Figure 4.8(b). the overall diffusion angle was clearly ap-

proaching zero near 272 nm. This is essentially the same as the peak wavelength of the hybrid film. The total diffusion angles in the wavelength range of 257—287 nm were calculated using a 1.1 mm thick hybrid film sample, the 250—256 nm and 288—450 nm were calculated using a 0.3 mm thick sample. This is because in wavelength ranges with large refractive index differences, the 1.1 mm sample film scattering was significant. The recorded diffusion angle was less than the real value because the current measurement method is not sensitive to scattering light with large diffusing angles. To appropriately evaluate the optical scattering intensity distribution, the light scattering can be decreased by using a thinner sample or decreasing the doping concentration. Next, the scattering model was completed based on the RW model in Section 6.2.1. Input variables such as dispersant concentration, sample thickness, CaF_2 particle size, detector acceptance angle, the difference of refractive index between CaF_2 and PDMS corresponding to a specific wavelength, and the single diffusion angle corresponding to the refractive index difference were used to run a random walk scattering simulation. The output results of the simulation are the transmittance as well as the total scattering angle distribution, etc. Herein, the difference in refractive index was the only cause of the single diffusion angle in this case. Hence, the change in single diffusion angles with modifications in the refractive index difference was certain in the specified scattering model. The specific computational process of a single diffusion angle is described as follows.

Similarly, the calculation process at 278 nm wavelength, as an example, was taken. First, the relationship between the total diffusion angle and the single diffusion angle calculated based on the RW scattering model is shown in Figure 4.10. After that, the corresponding value of the single diffusion angle is inversely inferred by bringing in the total diffusion angle obtained from the experiment. The specific calculation process is: the matching total diffusion angles were generated

by inputting varied original values of single diffusion angles, as shown by the black dots. After obtaining the relationship between the total diffusion angle and the single diffusion angle quantitatively by nonlinear fitting to the black spot, the value of the single diffusion angle is determined by considering the actual size of the total diffusion angle.

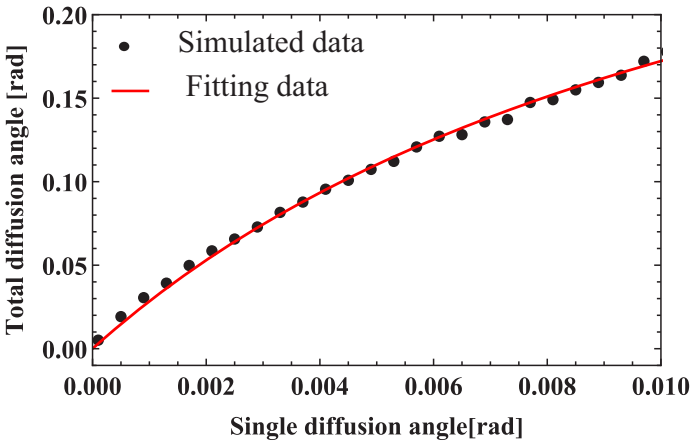

Figure 4.10: The simulation result of the relative relationship between the total diffusion angle and single diffusion angle for a 30 wt.% CaF_2 dispersed PDMS 1.1 mm thick film sample at a wavelength of incident light of 278 nm. The following is a description of the nonlinear fitting equation: $y = 0.491/(x + 0.018)$

After that, the variation of the single diffusion angle with the refractive index difference can be obtained based on the simulated relationship (showed in Figure 4.8(c)) between the refractive index difference and the wavelength, as shown in Figure 4.11(a). Also, the probability density function of the free path is considered as $f_{FP}(x)$ (as shown in Equation 6.3). The detailed procedure is described in Section 6.2.1. Then, according to the RW model, the UV light filtering properties of 0.3 mm and 1.1 mm thick film samples were simulated from 250 nm to 450 nm, based on a linear fitting relationship between the refractive index differ-

ence and predicted single diffusion angle ($\gamma = 0.29\Delta n$). As shown by red dots in Figure 4.11(b). When compared to the above-mentioned experimental results, it was demonstrated that the estimated spectrum data accurately reflects the hybrid films' light transmittance. In the 350—450 nm wavelength area, the simulation findings were marginally higher than the experimental results for the 1.1 mm thick film sample (lower curve in Figure 4.11(b)). This is because all directional scattering in this region is overly intense, resulting in larger experimental diffusion angle errors. The use of an RW scattering model to predict the CaF_2: PDMS hybrid film's transmission performance in the UV region is thus plausible.

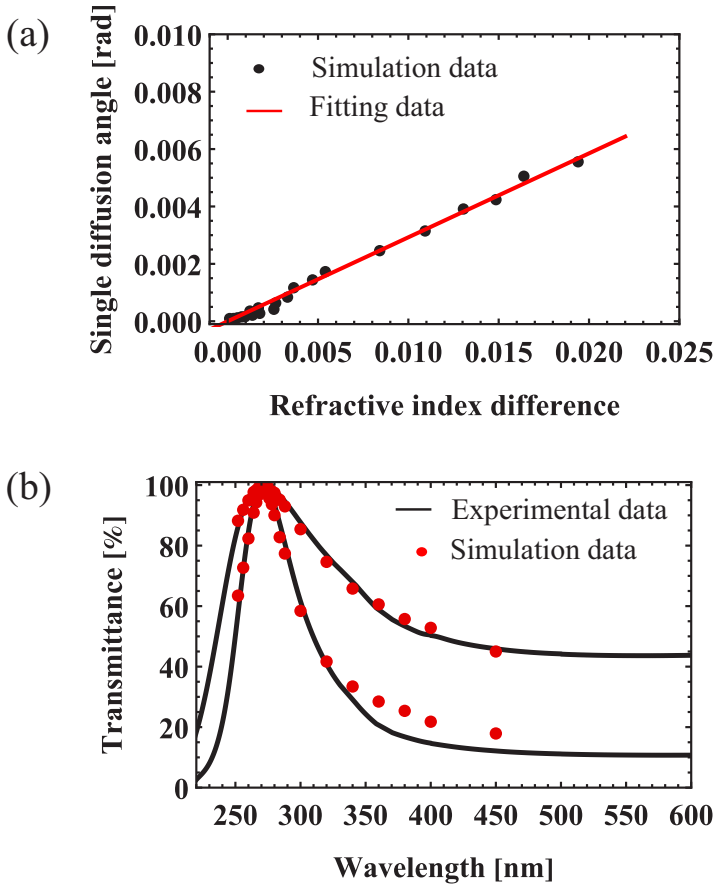

Figure 4.11: (a) Estimated correlation between refractive index differences and single diffusion angles (fitting curve: $\gamma = 0.29\Delta n$); (b) The experimental and estimation (using the single diffusion angle fitting results in (a)) transmittance comparison

4.3.4 LMW-PDMS or CQDs multiple dispersed for the transmittance peak tunability

Since the transparent wavelength of the hybrid film is determined by both the absorption of the material and the SRIM wavelength. So the method of actively tuning the transparent wavelength is to tune the position of the SRIM wavelength. According to the EMA theory in Section 2.3.3, the PDMS matrix's refractive in-

dex dispersion is considered to be changed by doping some materials to modulate the SRIM wavelength. So, LMW-PDMS and CQDs materials were mixed with the SIM-360 matrix to change the refractive index. Then, they are mixed with CaF_2 to change the SRIM wavelength. The sample fabrication process here is as described in Section 4.1. Then, the raw transmittance spectra of CaF_2 dispersed PDMS film filters with various LMW-PDMS and CQDs dispersing doses are shown in Figure 4.12. Herein, the peak wavelength transmittances of samples were marginally lowered while using the LMW-PDMS-dispersed film filter. This occurs because the addition of LMW-PDMS increases the absorption of UV light. On the other hand, the samples with CQDs dispersion have a significant decrease in peak transmittance with increasing CQDs concentration. Due to the lack of affinity between PDMS and CQDs, high-concentration CQDs dispersants generated significant aggregation problems. These aggregation problems, combined with the strong UV absorption of CQDs, lead to a rapid decrease in the transmittance of the hybrid films at the peak wavelength.

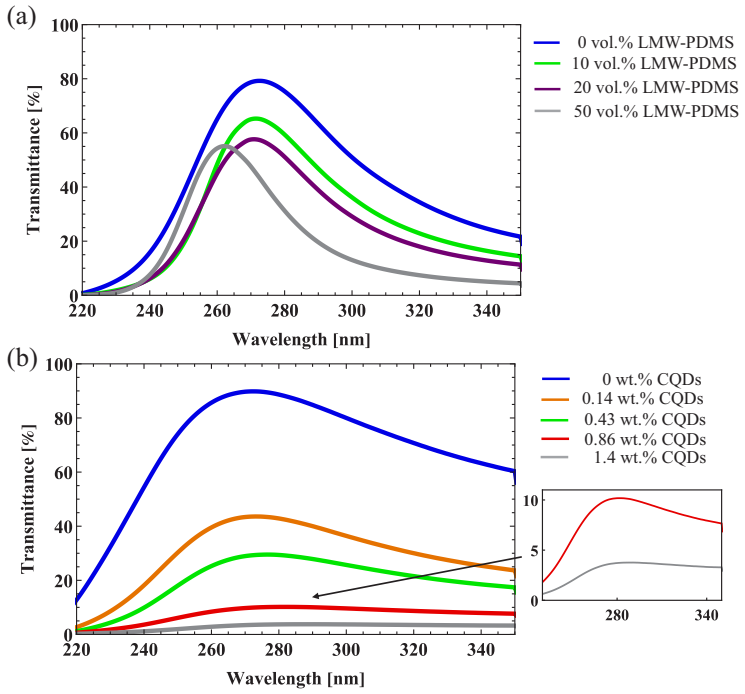

Figure 4.12: (a) Raw transmittance spectra of 1.1 mm thick film filters made by dispersing 0, 10, 20, and 50 vol.% LMW-PDMS into a 30 wt.% CaF_2: PDMS (SIM-360) hybrid material; (b) Raw transmittance spectra of 0.3 mm thick film filters made by dispersing 0, 0.14, 0.43, 0.86, and 1.4 wt.% CQDs into the 30 wt.% CaF_2: PDMS (SIM-360) hybrid material

After that, the shift of the peak wavelength was calculated based on the experimental results of transmittance. A peak wavelength blueshift or redshift of the hybrid film filter was obtained, as shown in Figure 4.13 and 4.14.

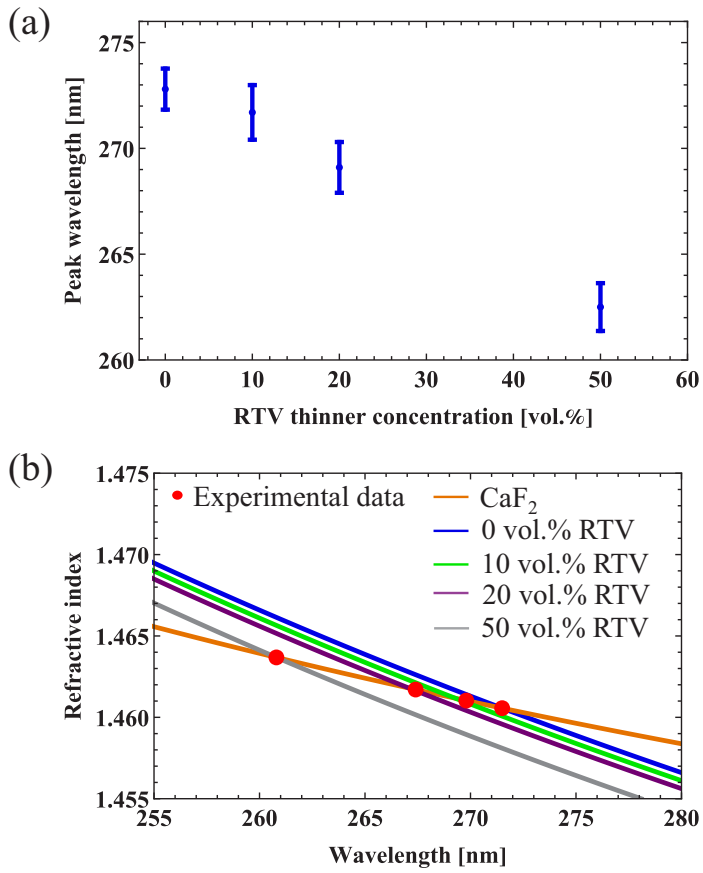

Figure 4.13: (a) Changes of peak wavelength with 0—50 vol.% LMW-PDMS (RTV thinner) dispersing concentrations; (b) Comparison between experimental and simulation at different LMW-PDMS dispersion concentrations. Herein, 30 wt.% CaF_2: PDMS (SIM-360) as a basis hybrid material; LMW-PDMS dispersed sample thickness was 1.1 mm; the experimental results in (a) is obtained based on the raw transmittance spectra, while the experimental results in (b) is obtained based on the transmittance spectra after removing the PDMS matrix absorption

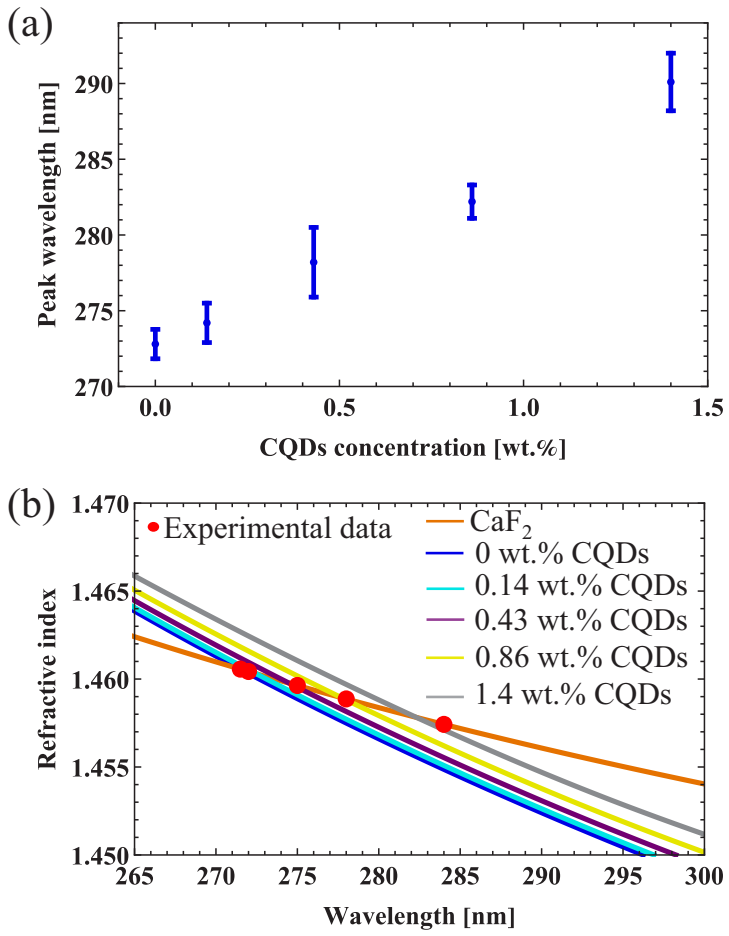

Figure 4.14: (a) changes of peak wavelength with 0—1.4 wt.% CQDs dispersing concentrations, (b) comparison between experimental and simulation at different CQDs dispersion concentrations. Herein, 30 wt.% CaF_2: PDMS (SIM-360) as a basis hybrid material; CQDs dispersed sample thickness was 0.3 mm; the experimental results in (a) is obtained based on the raw transmittance spectra, while the experimental results in (b) is obtained based on the transmittance spectra after removing the PDMS matrix absorption

Herein, the hybrid film's peak wavelength was blueshifted 10 nm by dispersing 50 vol.% LMW-PDMS, as seen in the figure 4.13(a). It demonstrates the hybrid film's spectral tunability. The dispersion curves of hybrid materials with varied dispersant concentrations were then generated using the Maxwell-Garnett

model [76–78] to theoretically illustrate these results, as shown in Figure 4.13(b). The peak wavelengths of the hybrid films were extremely close to the modeling findings after removing the absorption influence of the matrix. This is consistent with the theoretical conjecture that the peak transmittance wavelength should coincide with the SRIM wavelength after removing the matrix absorption. On the other hand, the peak wavelength of the CQDs dispensing CaF_2: PDMS hybrid film filter was redshifted by approximately 17 nm, when the CQDs concentration was increased to 1.4 wt.%, as shown in Figure 4.14(a). The simulation results of the refractive index dispersion curves of hybrid materials with various CQDs dispersing doses are shown in Figure 4.14(b). Similarly, after removing absorption effects in the experiments, the peak wavelengths of the hybrid films were nearly identical to the wavelength values corresponding to the refractive index cross points. In this concentration of 1.4 wt.%, the theoretical and experimental results of the SRIM wavelengths are somewhat disagreed. As described above, the sample transmittance at this concentration is extremely low due to the aggregation of CQDs, etc., resulting in a large experimental error. In future research, modified CQDs dispersants are expected to increase their dispersion in the PDMS matrix.

4.4. Conclusions

In terms of experimental results, this chapter evaluates the effects of thickness, strain, and temperature on the SRIM wavelength of scattering spectroscopic hybrid materials. Among them, only the response for the temperature change is significant, reaching 1.5 nm $^{\circ}C^{-1}$. In addition, the approach of multiply dispersed spectroscopic materials that can continuously tune to SRIM wavelengths was confirmed experimentally. The maximum control range of SRIM wavelengths

was -10 nm obtained for 50 vol.% LMW-PDMS dispersion and +17 nm for 1.4 wt.% CQDs dispersion. This result is also consistent with the results based on EMA theoretical calculations. In terms of simulation results, the simple RW scattering model based on Monte-Carlo theory and considering the RGD approximation extends the applicability range to 250—400 nm and allows the model to simulate the scattered light distribution. It compensates for the shortcomings of the RGD-Hulst model. However, the model is only applicable in the UV region when thin sample thickness. Therefore, it still needs to be improved.

Chapter 5

Fabrication and modeling of narrow UV bandpass transparent/scattering materials

5.1. Introduction and purpose

In Chapter 3, a new flexible spectroscopic scattering filter material transparent at a specific UV wavelength based on the SRIM principle utilizing inorganic particles dispersing organic materials is developed. Then, in Chapter 4, the tunability of transparent wavelengths was achieved by the refractive index adjustment of multiple dispersions. In this chapter, we will focus on the optimization of the spectroscopic properties of this flexible material and its application possibilities in integrated optoelectronic devices. In recent years, flexible integrated optoelectronic devices have made great progress [121–128]. The shortcomings of traditional electronic devices, such as their hard, weight, non-portability, and complexity production methods, are increasingly being overcome. However, The optical components being integrated into optoelectronic devices also need to be flexible due to the overall device flexibility and wearability requirements. Because of its flexibility, high light transmittance, biocompatibility and low cost, many optical devices based on PDMS materials have been developed. For example PDMS-based lenses [87,89,129,130], filters [92,131,132], and gratings [133–136]. Here, As mentioned in the introduction, we also proposed an approach called silicone optical technology (SOT®) [14–18] to rapidly fabricate small optical sensing/testing devices using PDMS materials. A series of optical components using the technology, including flexible optical lenses, gratings and wavelength conversion filters, have been created. Our latest research focused on constructing DNA/protein microfluidic optoelectronic devices that can be employed for fast diagnosis. In this application, a UV light filter with a filter capacity of about 10 nm is required for distinguishing measurement. Because DNA/protein have close absorption peaks at 260/280 nm, respectively [41,42]. However, this kind of narrow-band UV bandpass filter often needs a complicated fabrication process, some surface polishing,

high fabrication cost, and performance related to incident light angle, which makes it difficult to integrate them into the microfluidic system. As a result, a novel scattering filter hybrid material was demonstrated based on the SRIM principle by dispersing CaF_2 particles in PDMS in the previous Chapter 3. The manufacture of the UV transmission scattering filter is flexible, easy, cheap, is not limited by the incident angle of the input light, and can be applied to microfluidic systems by simple injection, potting, and other methods. Then, in Chapter 4, the dispersion of multiple dispersant materials, such as CQDs, was used to demonstrate the tunability of the filter's transparent wavelength, revealing its potential as a new material to fabricate arbitrary wavelengths transparent flexible bandpass filters. However, due to the constraints of the manufacturing method, conditions, and the manufactured CaF_2 particle distribution. In previous experiments, the best effective performance of hybrid filter material was about 30 nm FWHM. According to the beer-Lambert law, the spatial density (depending on particle concentration and particle size), sample thickness, particle size, and particle size distribution are the main determinants of reducing the effective bandwidth of the transmission spectrum. As a result, in Chapter 3, the RGD–Hulst model [79, 80] only partially reproduced the experimentally obtained effective transmittance spectra (in the 240—-310 nm wavelength region), and it is shown that increasing the CaF_2 particle size (in a certain range) and decreasing the particle size distribution can effectively reduce the transmittance spectrum bandwidth. However, since the model does not account for scattering light distribution, it is unable to predict the effective bandwidth when the scattered light reception conditions are changed. In Chapter 4, an RGD-considered 3D random walk (RW) scattering model was demonstrated. An "equivalent diffusing angle per single-particle" (single diffusing angle) was devised and determined as a function of the refractive index difference, which solved the difficulty to simulate the scattering light distribution in Chapter

3. Also, the RW model broadens the range of applicable transmittance bands. It can be utilized to forecast the spectroscopic performance of scattering materials under a certain range of concentrations and thickness conditions. However, it is unable to quantitatively forecast the spectroscopic performance of thicker and higher concentration hybrid materials or the effect of particle size and distribution on spectroscopic performance. As a result, this chapter combined an improved RW scattering model with RGD-Hulst model calculations. The optimal CaF_2 particle size, distribution, concentration, and sample thickness at this stage were calculated, and an optical module with a transmission spectroscopic bandwidth less than 10 nm was built. This is a milestone moment in developing DNA/protein microfluidic optoelectronic diagnostic devices for point-of-care applications.

5.2. Improved random walk model simulation results

The scattering filter hybrid material developed in this study is based on the SRIM theory, which states that the material is transparent for the light of SRIM wavelengths but scatters to varying degrees for incident light of non-SRIM wavelengths. As a result, increasing the scattering effect at non-SRIM wavelengths and adjusting the detector sensing surface size (the acceptance angle) are the two primary strategies to obtain extremely narrow spectroscopic performance inside 10 nm. Consider that in most cases, the detector conditions are preset. So increasing the scattering is the most concerning way in our study. Improving the scattering effect at non-SRIM wavelengths is practical by increasing the CaF_2 particle size within a specific range, reducing the particle distribution, and increasing the dispersing concentration and sample thickness. Herein, firstly the RGD-Hulst

model in Chapter 3 has pointed out the direction: increasing the CaF_2 dispersing concentration, particle size, and decreasing the particle distribution. The calculations point out raising the average particle size to around 10μm, narrowing the distribution as feasible can increase the scattering. In actuality, narrowing the particle distribution is more difficult, and the impact on spectroscopic performance is minor compared to the concentration. As a result, it is desirable to limit the particle size distribution to within 1–20 μm. Then, as described in Chapter 4, an RW scattering model was developed. It can simulate the scattered light distribution and take into account the influence of concentration and thickness on the scattering of low concentration and thin samples. But when the CaF_2 dispersing concentration and sample thickness vary widely or PDMS matrix changes, the model cannot be used to make quantitative predictions. As a result, an improved RW model with broad applicability is developed as shown in Section 6.2.2. Several parts of the scattering model were improved to the point where they can be used to quantitatively predict the spectroscopic properties of scattering materials within a given range. Also, it is expected to simulate all soft scattering phenomena based on the slight refractive index difference. Firstly, Figure 5.1 are used to provide the refractive index differences at different wavelengths. The various PDMS matrices refractive index dispersion is measured data by Ellipsometer (when the sample surface is in good condition), and the CaF_2 refractive index dispersion was obtained from the literature [69]. Then, in the improved RW model, the free path probability distribution $f_{FP}(x)$ is calculated as in equation 6.8 by adding thickness parameter. It takes into account that the scattered light may be deflected many times in thicker materials but still pass through the sample with a small diffusing angle. Also, the single diffusion angle is considered as a function of thickness and refractive index difference. The single diffusion angle per unit thickness— $\gamma(t_0/t)^{0.75}$, is calculated as a function of the refractive index

difference based on measured different wavelengths total diffusion angles results (Figure 4.8(b)). It is the same method as that used to calculate the relationship between the single scattering angle and the refractive index difference in Section 4.3.3. But the refraction index dispersion data used in this chapter's model came from experimental measurements (in Figure 5.1). After that, the calculated single diffusion angle per unit thickness versus the refractive index difference is shown in the Figure 5.2(a), where the fitted curve function is: $\gamma(t_0/t)^{0.75} = 9.2\Delta n^{2.4}$. The effective transmittance of a 30 wt.% CaF_2: SIM-360 hybrid film was estimated using this function. The estimated findings matched the experimental results in 220–450 nm wavelength range, as shown in Figure 5.2(b). Thus, compared to the 4.3.3 part, this further extends the applicable area.

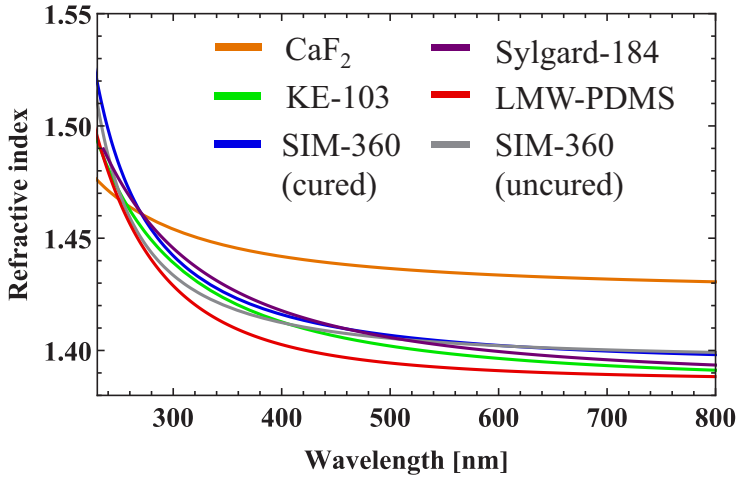

Figure 5.1: Refractive index dispersion measurements results of uncured PDMS matrices (SIM-360, KE-103, LMW-PDMS, Sylgard-184) and cured PDMS matrix (SIM-360), as well as CaF_2 refractive index dispersion from the literature [69]

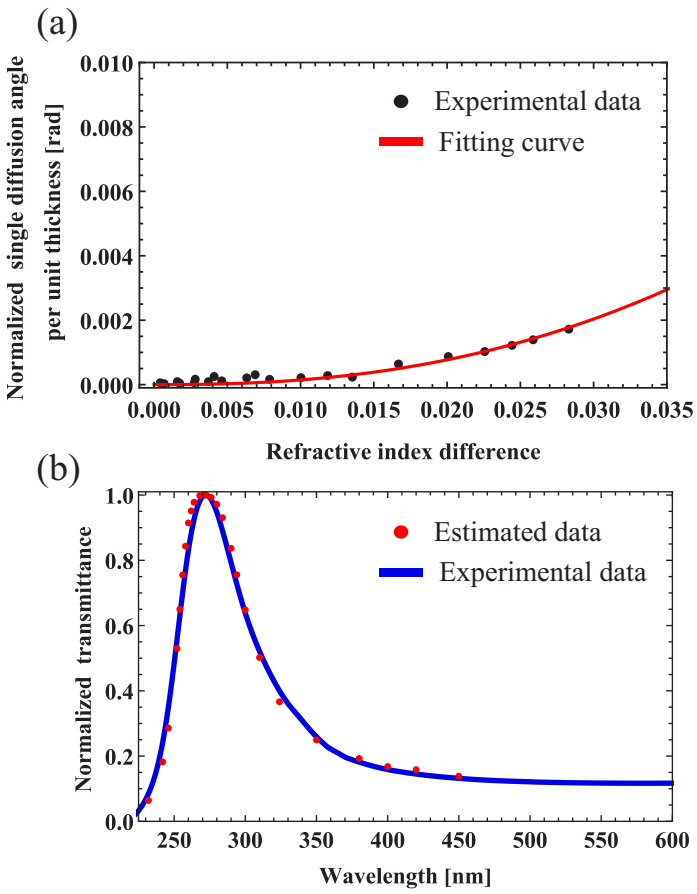

Figure 5.2: (a) Relationship between the normalized single diffusing angle per unit thickness-$\gamma(t_0/t)^{0.75}$ and refractive index difference (fitting curve: $9.2\Delta n^{2.4}$); (b) Comparison of experimental data (30 wt.% CaF_2: SIM-360 with 1.1 mm thick) with estimated transmittance findings based on the fitted single diffusion angle result

Furthermore, this improved RW model can accurately predict the transmittance spectra of materials with several PDMS matrices and concentrations. Figure 5.3(b) shows the simulated outgoing light average diffusing angle findings based on the improved RW scattering model for various concentrations and thicknesses conditions. This result is calculated based on the simulated scattered light distribution as in Figure 5.3(a). The findings show that dispersing PDMS with

the maximum feasible CaF_2 concentration and increasing the sample thickness can significantly enhance the diffusion angle at non-SRIM wavelengths. However, when the thickness reached 4 and 5 mm, the change in average diffusion angle was no longer significant. Also, considering the possibility of scatterer formation and absorption losses by the matrix material, an 80 wt.% concentration and a scatterer thickness of 4 mm indicate optimal conditions at this stage. It is expected to achieve spectroscopic performance within 10 nm by combining scattering filtering hybrid materials manufactured under optimal narrowing conditions with a narrower acceptance angle. (Previous investigations of sample transmittance spectra from Chapter3 and Chapter 5 used the spectrophotometer measurement arrangement illustrated in Figure 5.9 to acquire effective transmittance spectra and bandwidths. It only represents the spectroscopic performance at a specific angle.). Therefore, the scattering materials in this chapter will be fabricated under optimal narrowing conditions: CaF_2 particles with a size distribution in the range of 1–20 μm; concentration: 80 wt.%; sample thickness: 4 mm; small acceptance angles with an acceptable signal loss. All of which combined to achieve the spectroscopic performance target of 10 nm.

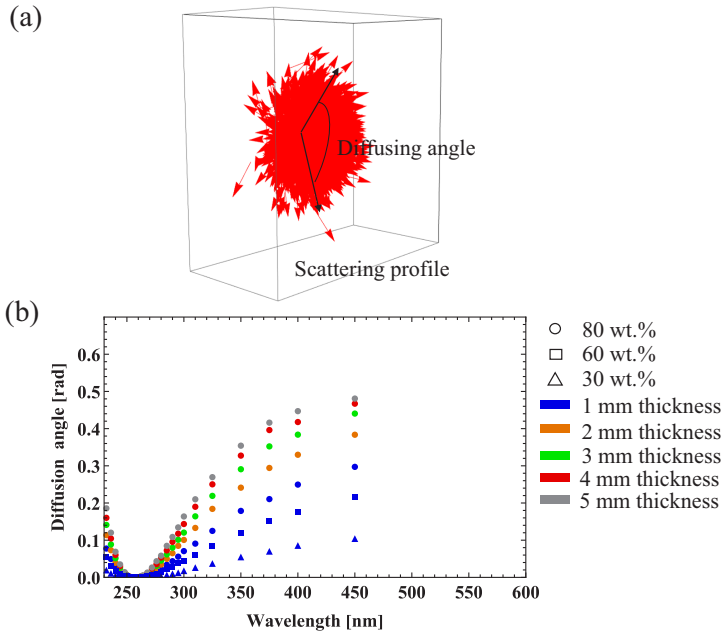

Figure 5.3: (a) scattering profile of incoming light with a wavelength of 400 nm passing through a 1 mm thick sample (80 wt.% CaF_2: SIM-360 matrix); (b)The estimated average diffusion angle after passing through the sample with various conditions

5.3. Scattering hybrid materials fabrication under optimal conditions

Figure 5.4 demonstrates how CaF_2 particles are made and how precipitation and centrifugal separation limit the particle size distribution. The powder of CaF_2 (VI) containing micron, submicron, and even nanoscale particles was made by grinding CaF_2 molding material (OKEN) with a 3D milling machine (MDX-40A, Roland) equipped with a diamond drill, as shown in Figure 5.4(a). The results show that this fabrication approach is more efficient than hand and electric router grinding (in chapter3 and chapter 4). Then, the precipitation separation

was used to remove large particles, as shown in Figure 5.4(b): the CaF_2 particles were dispersed in LMW-PDMS firstly, and the top 80 % of the mixture liquid was collected after stirring well and standing for 30 s. Next, pure LMW-PDMS was added to the remaining mixture to collect more particles. After repeating the above steps three times, go to the centrifugal separation as shown in Figure 5.4(c). This time, the upper 80 % volume of the collected mixture was eliminated after mixing at 1440 rpm for 60 seconds by centrifugal mixer (KK-50S, Kurabo). After that, add pure LMW-PDMS and repeat this centrifugal separation step 7 times. Finally, the residual mixture was washed three times with toluene to eliminate the LMW-PDMS, and the CaF_2 particles with a restricted particle size distribution were obtained by evaporating the toluene, as shown in Figure 5.4(d).

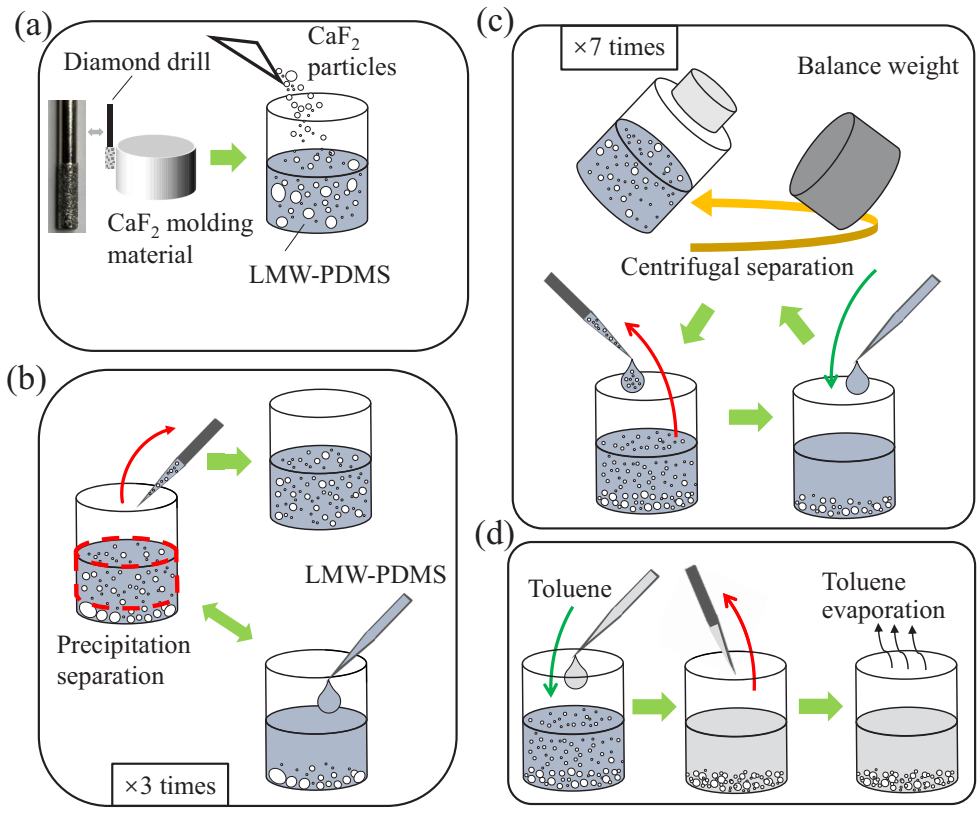

Figure 5.4: (a) CaF_2 particle fabrication procedure; Precipitation (b) and centrifugal (c) separation in LMW-PDMS to separate CaF_2 particles; (d) LMW-PDMS removing procedure

The scattering hybrid films in this investigation were made using two different fabrication processes. First, the CaF_2 particles are dispersed into PDMS matrices (SIM-360, KE-103, LMW-PDMS and Sylgard 184) and uniformly mixed for 200 seconds with a mixer (KK-50S, Kurabo) at 1440/1440 rpm (revolution/autorotation), as shown in Figure 5.5(a). Next, the combination of CaF_2 and PDMS was swirled at 1440/475 rpm for 90 seconds after adding the curing agent to make the standard cured films (30, 60, and 80 wt.%) as shown in Figure 5.5(b). It was then potted into molds and coved with a PMMA plate for over 28 hours before vacuum defoaming and curing at 50 $°C$. Alternatively, for the high-concentration

films (60, 80 wt.%), the samples were directly potted and sandwiched between two transparent quartz plates after mixing CaF_2 and PDMS thoroughly. Also, sample thickness is regulated by a spacer, as shown in Figure 5.5(c). Only the high-concentration films could benefit from this uncured technique. A scanning electron microscope (SEM, TM-4000Plus, Hitachi) was used to determine the size of the CaF_2 particles, an ellipsometer (SE-2000, SEMILAB) was used to determine the refractive index of the PDMS matrices, and a spectrophotometer (V-630, JASCO) and a fiber optic spectrometer (HR-4000, Ocean Optics) were used to evaluate the scattering hybrid materials.

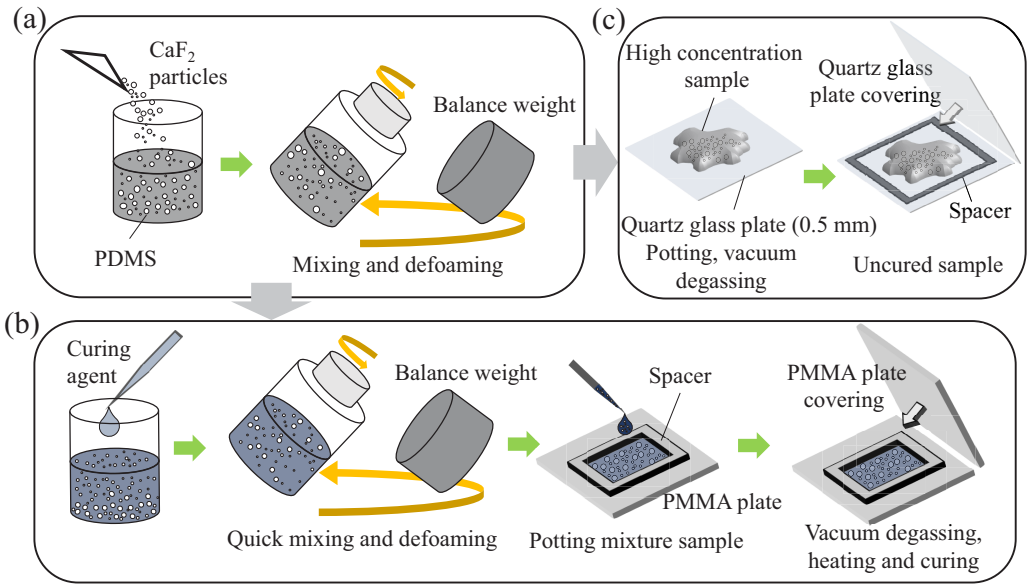

Figure 5.5: The scattering hybrid material sample fabrication: (a) CaF_2 in PDMS matrix mixture was mixed and de-bubbled; (b) Typical cured film fabrication procedures of 30, 60, and 80 wt.% concentrations; (c) Uncured sample fabrication procedures with 60 and 80 wt.% concentrations

5.4. Result and discussion

5.4.1 Particle size distribution of CaF_2

Figure 5.6(a) demonstrated SEM images of CaF_2 particles before precipitation and centrifugal separation. The directly ground CaF_2 particles have large size distribution that can be observed. It includes not only larger micron particles but also submicron and even nanoparticles. According to the calculation results of the RGD-Hulst model shown in Figure 3.14, it is known that reducing the particle distribution and increasing the particle size can reduce the transmission bandwidth. Although it seems to be more effective to increase the average particle size, narrowing the particle distribution to 1–20 μm is sufficient at this stage considering the difficulty of implementation. Moreover, Restricting the particle distribution also increases the average particle size because it removes many nano- and submicron particles (less than 1 μm). Meanwhile, it effectively reduces the mixture's viscosity, allowing for the fabrication of highly concentrated hybrid samples previously impossible to achieve. On the other hand, the scattering caused by the larger micron-scale particles ($> 20\mu$m) is weaker, despite occupying most of the mass fraction. So, large micron particles needed to be removed to increase the percentage of micron particles with stronger effective scattering. Figure 5.6(c) shows the SEM picture after precipitation and centrifugal separation, it is obviously that submicron, nanometer, and some larger micron particles have been eliminated. Then, after the SEM images were processed (using Wolfram Mathematica), the quantity ratio and volume ratio of each size particle before and after separation were shown in Figure 5.6(b) and (d), respectively. The separation stage clearly eliminated particles below 1 μm, and above 20 μm, with removal rates of 75 and 100 %, respectively. Since the contaminants blended into the scattering hybrid material will affect spectroscopic performance, the number of solvents utilized

in the separation process is restricted. Precipitation and centrifugal separation will be difficult to narrow the existing particle distribution further. As a result, alternate strategies for narrowing the particle distribution, such as micron sieve filtration, should be studied in the future.

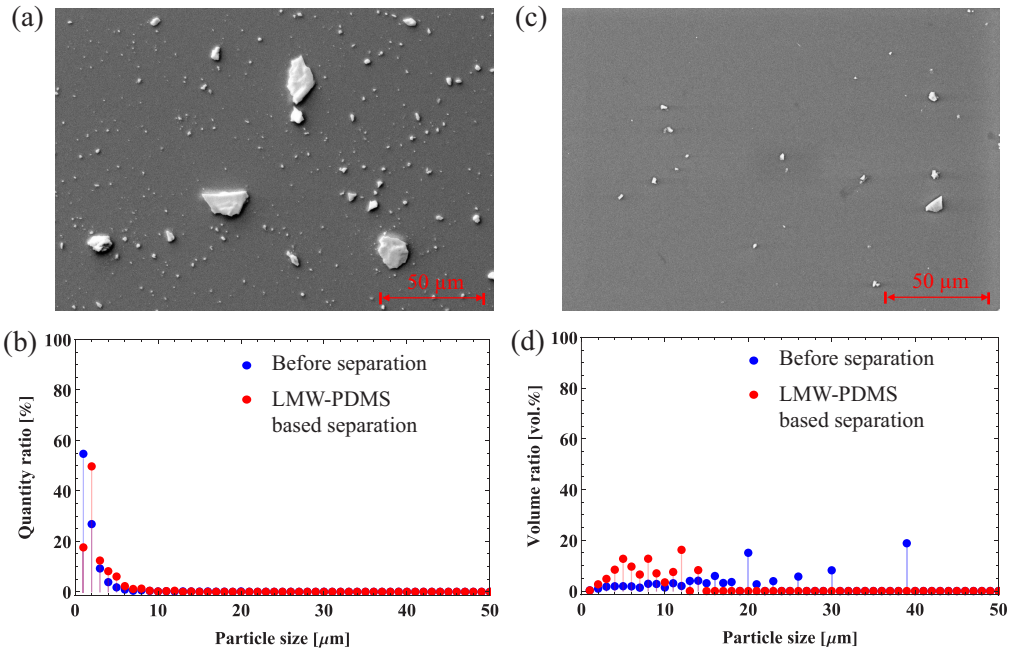

Figure 5.6: SEM Images of the CaF_2 particle distribution were taken (a) before and (c) after the LMW-PDMS-based separation processes; (b) The quantity ratio distribution of different size CaF_2 particles before and after separation; (d) The volume ratio distribution of different size CaF_2 particles before and after separation

In addition, since chemical synthesis allows for more precise control of particle size and distribution than grinding, certain synthesized commercial CaF_2 powders were tested to see if chemical synthesis might be used to achieve narrower particle distributions. The particle size distributions of the three commercial CaF_2 powders are shown in Figure 5.7(a), (c), and (e), respectively, while (b), (d), and (f) correspond to high-magnification images. Their particle sizes are clearly

smaller than 50 μm, just like the CaF_2 particles employed in this investigation. The scattering hybrid films were made by dispersing the three synthesized CaF_2 powders in a PDMS matrix (KE-103 or Sylgard 184) and evaluating them with a spectrophotometer (Figure 5.8). The transmittance peak was not detected significantly. Contaminants in the chemical synthesis could be to blame for this. Even if only minute amounts of contaminants were incorporated into the CaF_2 powders, they would significantly impact refractive index dispersion curves, causing the CaF_2 and PDMS refractive index matching points to vanish or shift to unnoticed wavelength regions. This experimental outcome highlights the originality of our research and the complexity of SRIM control.

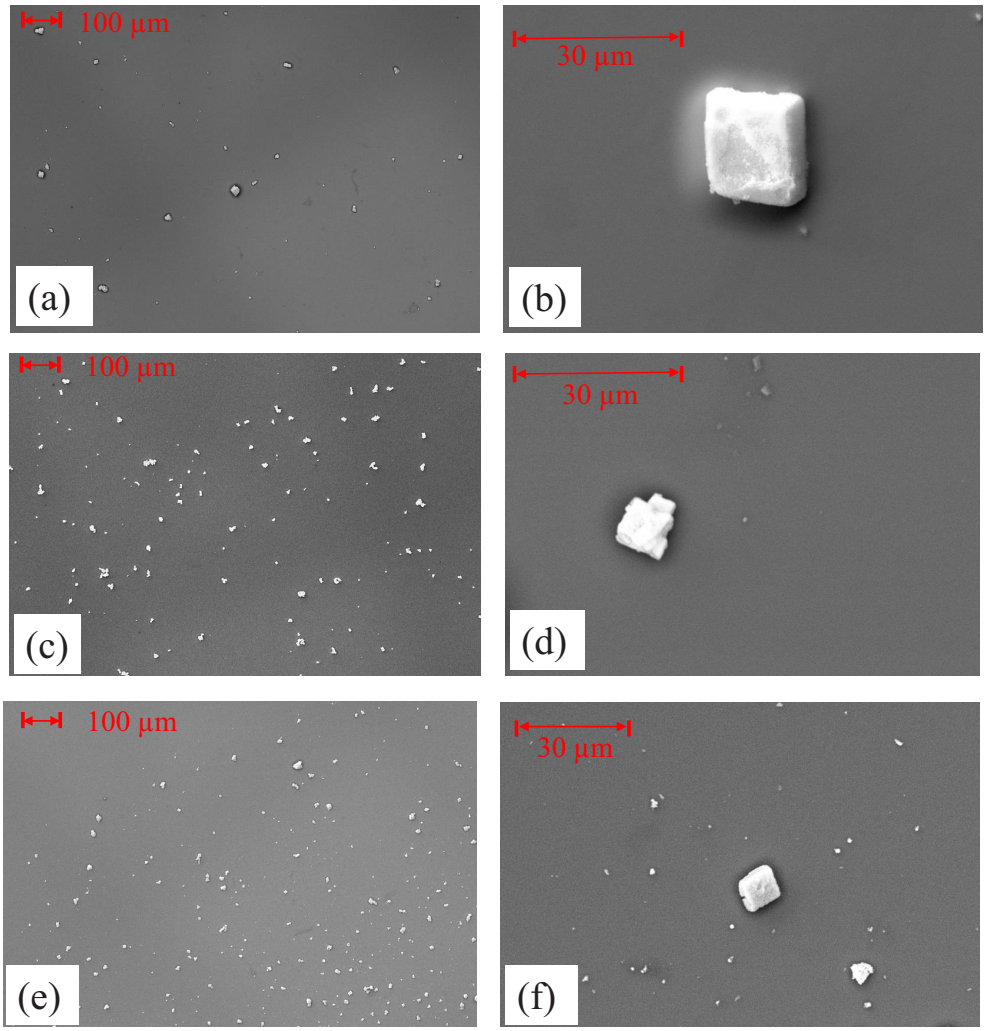

Figure 5.7: SEM images of commercial CaF_2 powders: (a) and (b) from Hakushin Chemical (Powder Ⅳ described in Table 2.2), (c) and (d) from High purity chemical (Powder Ⅲ described in Table 2.2), and (e) and (f) from Wako chemical (Powder Ⅱ described in Table 2.2)

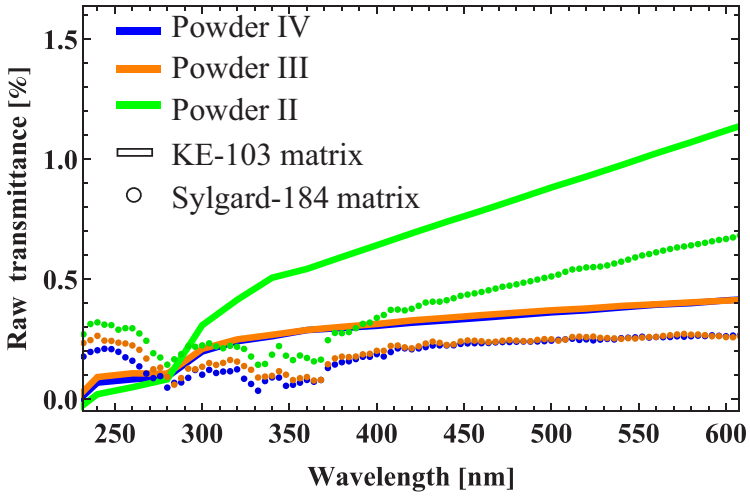

Figure 5.8: Raw transmittance spectra of 1 mm-thick uncured films prepared by three commercial powders (60 wt.%) dispersing into PDMS matrix (KE-103 or Sylgard 184)

5.4.2 Spectroscopic performance of CaF_2 dispersed PDMS

Figure 5.9 depicts a schematic of the set-up for evaluating scattering hybrid films with a spectrophotometer (V-630, JASCO), revealing that only partially scattered light reaches the detector, resulting in bandpass properties. In addition, images (a1), (a2), (a3), and (a4) depict a pure PDMS cured film, a 30 wt.% concentration cured film, an 80 wt.% concentration uncured film, and an 80 wt.% concentration uncured film sandwiched between two pieces of quartz glass, respectively. As can be seen from (a3), the high concentration uncured scattering hybrid material has the property of being deformable, demonstrating the possibility of its application in some flexible complex structure devices. Previous results from chapter3 confirmed the capacity to tune the wavelengths of the transmittance peak by changing the matrix type. Similarly, the findings of several uncured 1 mm-thick 80 wt.% concentration scattering hybrid films with varying transmittance peak wavelengths of 272, 257, and 248 nm are shown in Figure 5.10 (corresponding to

Sylgard-184, KE-103, and LMW-PDMS matrices, respectively). In comparison to prior investigations in chapter 3, some of the transmittance peak wavelengths showed a slight blue shift. The reason that can be considered is that the high concentration samples here are all uncured samples. The refractive index of the PDMS matrix becomes lower due to the lack of a high refractive index curing agent, resulting in the blue shift of the SRIM wavelength.

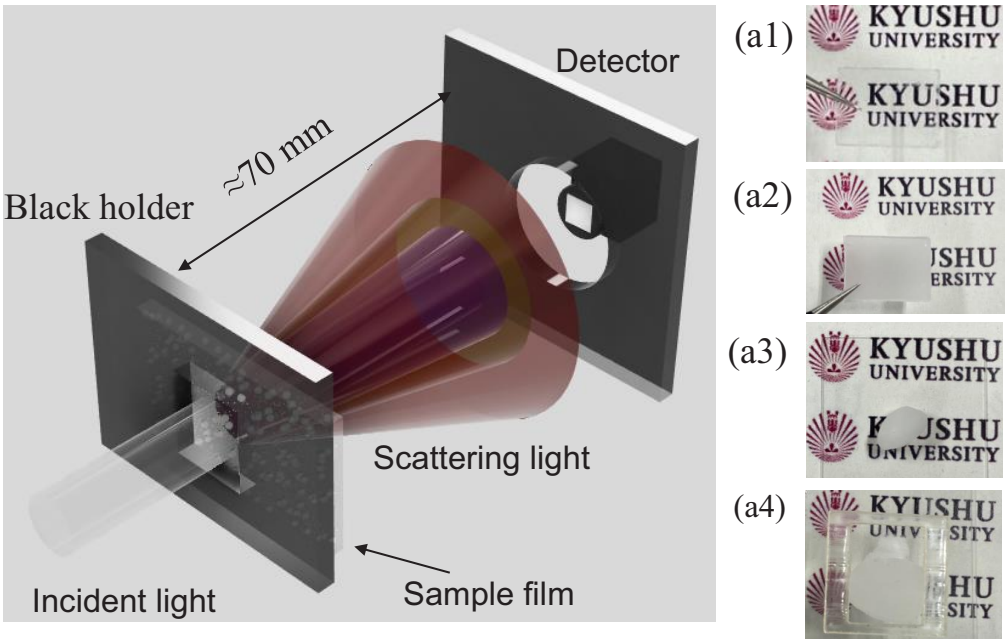

Figure 5.9: Transmittance evaluation setup in spectrophotometer, and the images of the (a1) pure KE-103 cured sample, (a2) 30 wt.% CaF_2: KE-103 cured sample, (a3) 80 wt.% CaF_2: KE-103 uncured sample, and (a4) 80 wt.% CaF_2: KE-103 uncured sample sandwiched between two pieces of quartz glass. The sample thickness is 1 mm in images of (a1), (a2) and (a4))

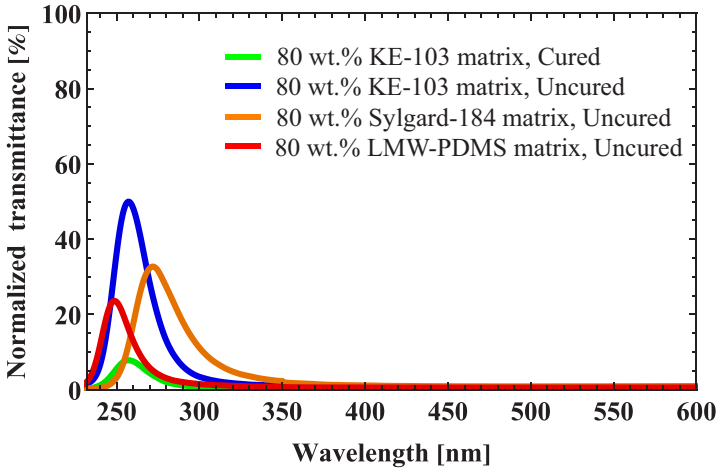

Figure 5.10: 80 wt.% high concentration CaF_2: PDMS scattering hybrid films transmittance spectra (where the PDMS matrices were KE-103, Sylgard-184, and LMW-PDMS, respectively)

In addition, the uncured sample exhibits a higher transmittance than the cured sample, according to the transmittance spectra shown in Figure 5.10. Among them, the peak transmittance of 80 wt.% CaF_2: KE-103 uncured sample almost five times higher than the 80 wt.% CaF_2: KE-103 cured sample. The transmittance loss can be considered scattering from the following causes: (i): the hard-to-remove air bubbles mixed during the production of highly concentrated samples; (ii): the surface cracks resulting from the shrinkage of the PDMS matrix during the curing process. Meanwhile, as shown in Figure 5.11, the results of the effective transmittance of the samples with different concentrations fabricated using the KE-103 matrix are essentially consistent with the predictions based on the improved RW model. It demonstrates the improved model's accuracy and indicates that it can be applied wider.

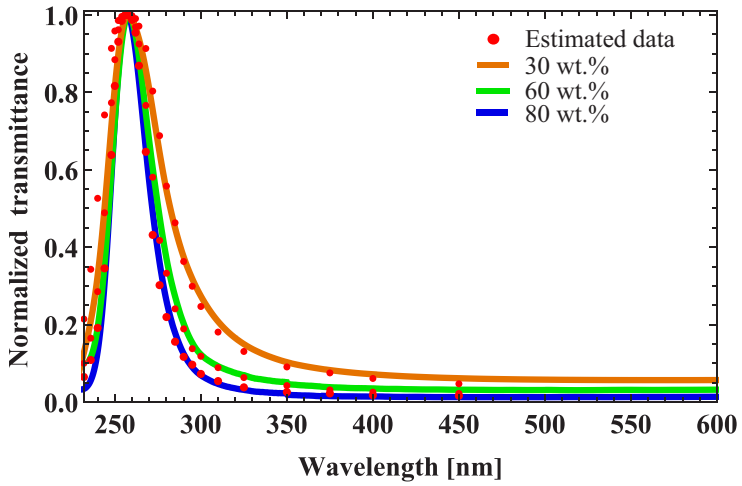

Figure 5.11: Experimental and estimated results comparison of 1 mm-thick different concentrations CaF_2: KE-103 films, the estimated results calculated based on the improved RW model

Most scattering hybrid film with an 80 wt.% concentration can be fabricated by dispersing narrow particle size distribution CaF_2 into a low-viscosity PDMS matrix. However, even using a narrow particle size distribution CaF_2, scattering hybrid film based on the SIM-360 matrix is difficult to fabricate at an 80 wt.% concentration due to the high viscosity of SIM-360. Moreover, as can be obtained from Figure 5.12, in addition to the conclusion that increasing the CaF_2 particle concentration can narrow the effective bandwidth, the 30 wt.% CaF_2: SIM-360 sample film's effective bandwidth change of before and after separation points out that narrowing the particle size distribution can likewise narrow the effective bandwidth. This also verified the RGD-Huslt model estimated results in Figure 3.14. Furthermore, according to the Figure 5.12 and the cut-off wavelength order of PDMS matrices (LMW-PDMS, KE-103, SIM-360, Sylgard 184), it can be concluded that using a PDMS matrix with a shorter cut-off wavelength can narrow the effective bandwidth because PDMS absorption increases with decreasing wavelength.

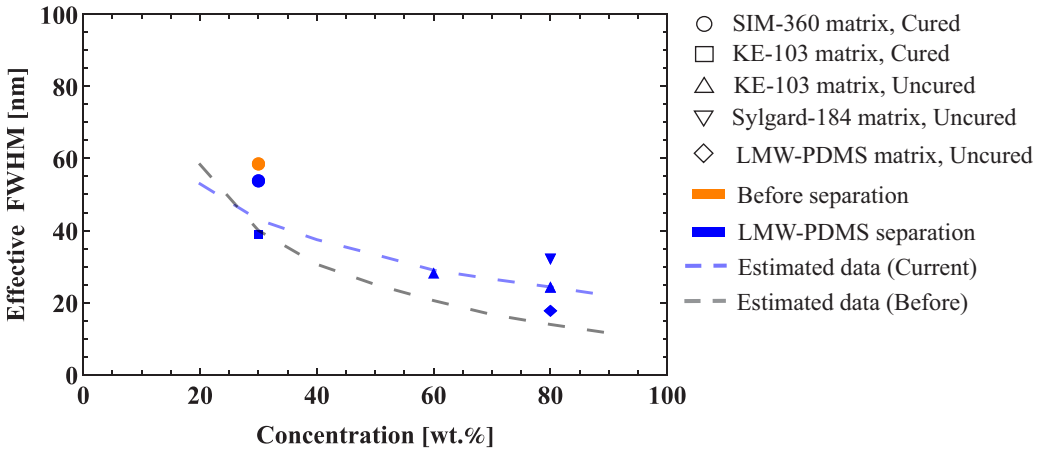

Figure 5.12: The changes of the 1 mm-thick scattering hybrid films' effective transmittance bandwidth with increasing CaF_2 concentration, as well as experimental and estimated results (based on RW and improved RW models) comparison of CaF_2: KE-103

Furthermore, the improved RW model, as shown in Figure 5.12, gives a better fit than the old model. The experimental results of the KE-103 matrix-based samples are almost consistent with the estimations calculated using the improved RW model. Then, increased film thickness efficiently narrows the transmittance bandwidth within a particular range, as shown in Figure 5.13, with the 4 mm-thick film based on an LMW-PDMS matrix having the narrowest effective bandwidth (FWHM) of 12 nm at this stage.

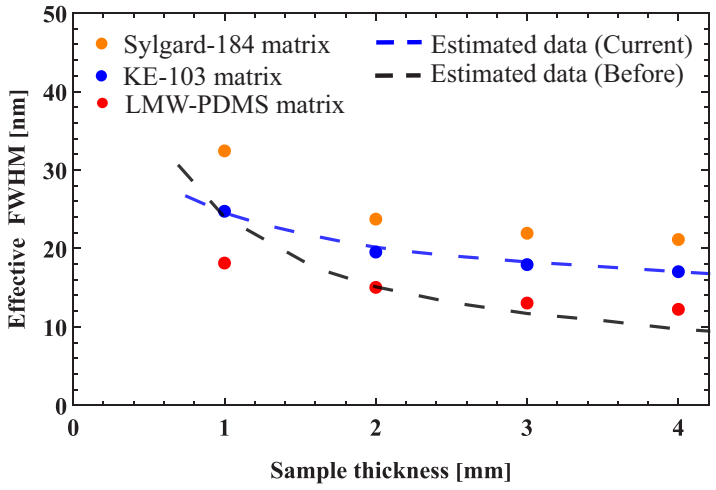

Figure 5.13: The changes of the 80 wt.% concentration scattering hybrid films' effective transmittance bandwidth with increasing thickness, as well as the experimental and estimated results (based on RW and improved RW models) comparison of CaF_2: KE-103

In addition, the improved RW scattering model's predictions in Figure 5.13 are in general agreement with the experimental results, which are vastly improved above prior research' results. This further supports the new model's broad applicability, indicating that it might be utilized with any soft scattering based on the slight refractive index difference. It is demonstrated in this work that the improved RW model may be utilized to analyze the spectroscopic properties of scattering hybrid materials quantitatively. This has important implications for further increasing spectroscopic performance and forecasting how the scattering hybrid material will be used in various scenarios. As a result, the optimal 12 nm FWHM experimental result in this section not only lowers the effective bandwidth to about 10 nm, but also clarifies the methods for improving spectroscopic performance: narrowing the particle size distribution and increasing concentration and sample thickness. These results also show that the simulation-based optimal conditions in Section 5.2 are correct. While the exact acceptance angle size

based on spectrophotometer measurements is unknown, a genuine bandwidth of less than 12 nm should be attained by choosing a sufficiently narrow acceptance angle. This opens the door to the development of microfluidic chips to detect DNA and proteins.

5.4.3 Scattering materials integrated application

To construct a viable DNA and protein detection device, first, A 80 wt.% concentration, 4 mm-thick CaF_2 (1–20 μm): KE-103 scattering hybrid film was fabricated. Then, as shown in the figure 5.14(a), an integrated module was developed: 2 pinhole structures (2 mm diameter) sandwiching the scattering material (CaF_2: KE-103 sample) and combined with a 260 nm central emission wavelength LED. Also, the emission intensity spectrum of the integrated module was measured using a fiber optic spectrometer. According to the results, as shown in 5.14(b), when the receiving angle is less than 0.1 rad (the fiber spectrometer is directly coupled to the optical module for measurement), the 4 mm-thick scattering film may decrease the real bandwidth of the UV LED emission spectrum from 12 to 9 nm. This performance meets the basic requirements for discriminating between DNA and protein detection and serves as a step forward in developing and producing DNA/ protein microfluidic detection devices.

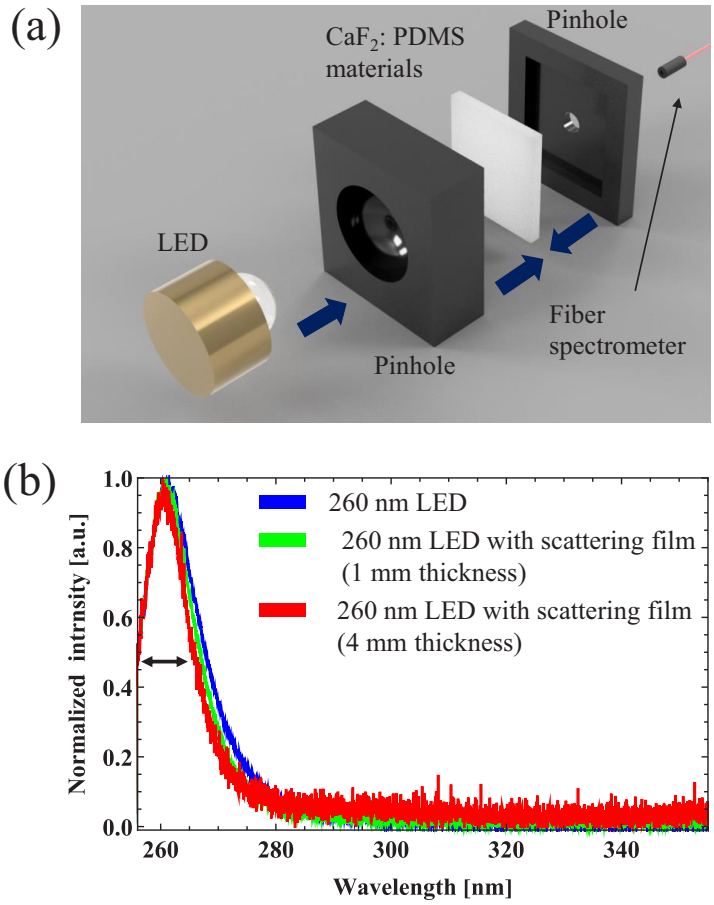

Figure 5.14: (a) The scattering hybrid material (CaF_2 dispersed in a KE-103 PDMS matrix) embedded an integrated optical module and evaluation setup; (b) The integrated optical module's normalized emission spectra

5.5. Conclusion

In terms of experimental results, this chapter obtained CaF_2 particles distributed in 1-20 μm by precipitation and centrifugation and developed 80 wt.% concentration, 4 mm sample film based on uncured PDMS (LMW-PDMS, KE-103, Sylgard- 184). In particular, the narrowest effective FWHM of 12 nm was

achieved with the CaF_2: LMW-PDMS hybrid materials. In addition, an optical module with a narrow emission spectrum of 9 nm narrow bandwidth was developed by modularizing the 80 wt.% CaF_2: KE-103 combination with a 260 nm center wavelength UV LED. In terms of simulation results, in this chapter, the RW model improved by introducing a thickness parameter is constructed. This model further compensates the case that the simple RW model in the previous chapter does not apply to thicker samples. It applies to samples of different thicknesses from 1—4 mm, and the applicable wavelength range is extended to the visible region (220—450 nm). It is possible to predict the effective transmittance and part of the scattered light distribution at this stage. Then, the improved model and the simple calculation of RGD-Hulst in this chapter also suggest the optimum conditions for obtaining the best spectroscopic performance at this stage. This is important for the application development of scattering spectroscopy materials. In addition, based on the results in this chapter, the conclusions that narrowing the particle distribution has limited improvement on the spectroscopic performance and increasing the spatial density has the most significant improvement on the spectroscopic performance are figured out.

Chapter 6

Development of scattering simulation model

In this thesis, three models were used to interpret and simulate the effective transmittance and scattering distribution of the samples. They are a simple calculation based on the RGD-Hulst approximation, a Monte Carlo principle-based random walk (RW) model that considers RGD scattering, and a modified random walk model with thickness parameter calibration. In this chapter, the advantages and disadvantages of each of these three models and the conditions for matching the experimental results will be discussed.

6.1. RGD-Hulst hybrid calculation model

As mentioned in Chapter 2.4, the formulation of the RGD-Hulst model is based on the Beer-lambert principle, where the effective scattering cross-sectional area is calculated based on the RGD (eq. 2.7) and Hulst approximations (eq. 2.9), respectively. In fact, according to the scattered light distribution measurements in Chapter 3, the scattering in the UV wavelength region tends to RGD scattering. In contrast, the scattering in the visible region tends to Mie scattering. So a hybrid model is considered for the simulation calculation in Chapter 3. The effective scattering cross-sectional area σ_{eff} of this hybrid model was calculated by interpolated with σ_{RGD} and σ_{Hulst} as shown in equation 6.1.

$$\sigma_{\text{eff}} = \eta\sigma_{Hulst} + (1-\eta)\sigma_{RGD} \tag{6.1}$$

, where $\eta = \frac{\varphi}{\sqrt[3]{1+\varphi^3}}$ and phase delay φ as the size parameter here, to switch the σ_{RGD} to σ_{Hulst}. It can be given by equation 2.8. Then, according to above definitions, $\sigma_{\text{eff}}/\sigma_N$ can be plotted as shown in figure 6.1.

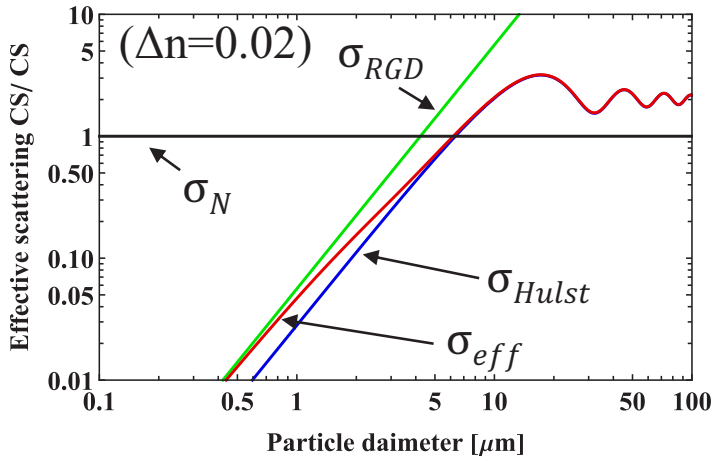

Figure 6.1: The difference between various scattering cross-sectional areas

This model is mainly applied in Chapter 3, it ignores part of transmittance caused by diffraction. But the size distribution of CaF_2 particles as shown in Section 3.3.4 is considered. So the sample transmittance is given by the following equation based on the beer-lambert theory.

$$T = e^{-t\sum(\sigma_{\text{eff}})_i N_i} \tag{6.2}$$

, where t is sample thickness and N_i is the spatial density of the respective particles, (σ_{eff}) is the effective scattering cross-sectional area of the respective particles. In addition, absorption and surface reflection losses are not considered in the experimental results and simulations. Then, according to the fitting results of 3.13 in Chapter 3, it can be seen that the model is applicable in the UV region range of 240—310 nm (RGD scattering region). Although this is sufficient for predicting the spectroscopic performance under different concentration thickness conditions, it cannot effectively simulate the distribution of scattered light. As shown in Figure 6.2, the RGD-Hulst model is used to calculate the effective scattering cross-sectional area by adding the parameter of refractive index difference. However, the refractive index difference of the mixed material is a function

of wavelength, so there are cases of small and large effective scattering cross-sections. Most of the light passes through and enters the detector for particles with a small effective scattering cross-section. For particles with a large effective scattering cross-section, the calculation of the RGD-Hulst model is treated as not transmitted. However, the actual scattering situation is shown in Figure 6.3(a). For particles with a large effective scattering cross-section, the detector still detects some of the small-angle scattered light. It caused the mismatch between the experimental and simulated results in the region of large refractive index difference (the visible region) in Figure 3.13. Hence, a model that can simulate the scattered light distribution is necessary to remedy this problem.

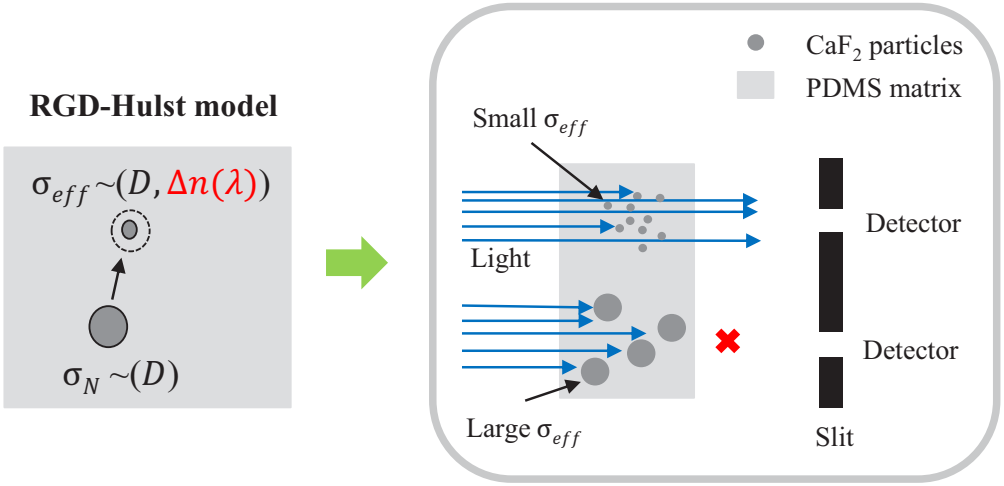

Figure 6.2: The principle of the RGD-Hulst model to calculate the effective transmittance (where σ_N is the cross-sectional scattering area calculated from the geometry, σ_{eff} is the effective scattering cross-sectional area)

6.2. Random walk scattering model

6.2.1 Random walk model considering the RGD scattering approximation

The RGD-Hulst hybrid model cannot calculate the transmittance with a large effective scattering cross-section because the RGD-Hulst calculation cannot simulate the scattered light distribution. A simple random walk model that considers the RGD scattering is developed to extend the applicability. Its fundamental constitutive principle has been presented in Section 2.5. The construction process will be described in more detail in this section. In order to solve the shortcomings of the RGD-Hulst model, the model needs to be constructed according to the actual situation as shown in Fig. 6.3(a). Therefore, as shown in Fig. 6.3(b), the MFP is calculated based on the effective scattering cross-sectional area σ_{eff} by considering the RGD scattering. Then the scattering of different sized particles is simulated based on the variation of the MFP and the deflection angle $\Delta\theta$. The whole simulation process is shown in Fig. 6.3(c). The specific process is as follows.

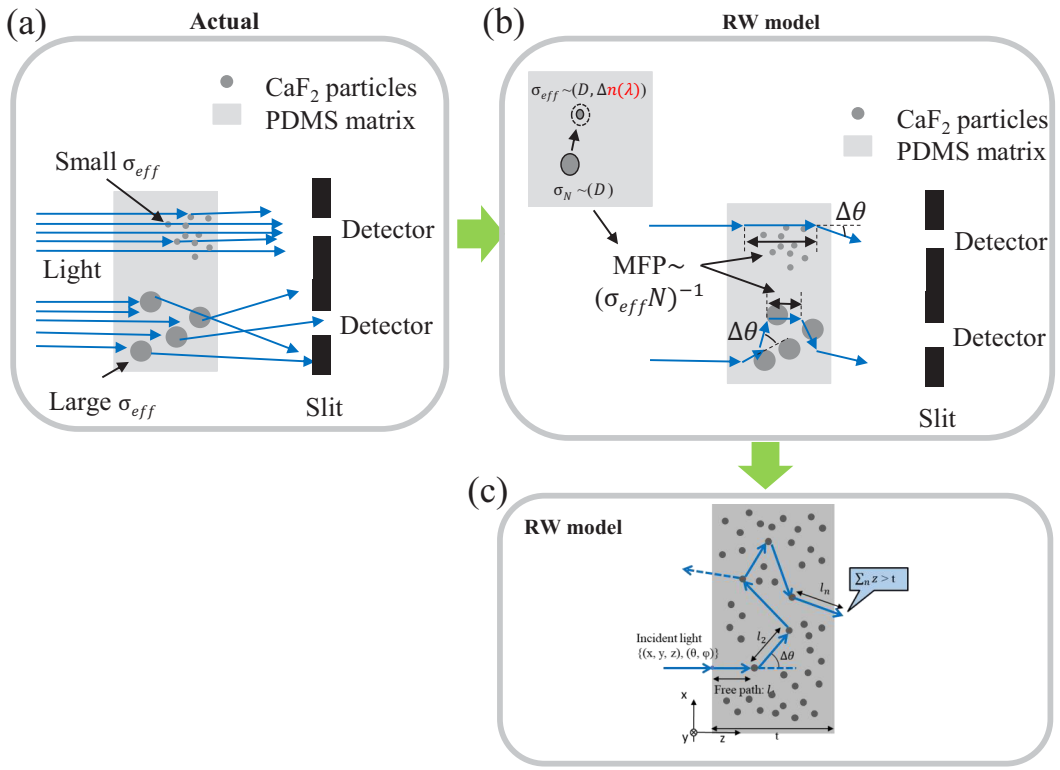

Figure 6.3: (a) The actual scattering of light by particles of different sizes; (b) Principle of the RW model for simulating the light scattering process; (c) Light transmission schematic using the RW scattering model (same as Figure 2.6)

As described in Section 2.5, the deflection angle $\Delta\theta$ is a random deflection angle obtained after injecting the light beam into a particle. And the free path l is an arbitrary distance passed by the light before it hits another particle. Each free path length l is chosen randomly from a pre-calculated database of l_i ($i = 1 \ldots 10000$). The database is calculated based on exponential distribution with the probability density function $f_{\mathrm{FP}}(x)$. It is calculated by

$$f_{FP}(x) = \sigma_{\mathrm{eff}} N e^{-\sigma_{\mathrm{eff}} N (x - \frac{D_{\mathrm{eff}}}{2})}, (x > \frac{D_{\mathrm{eff}}}{2}) \tag{6.3}$$

, here N also denotes the spatial density, σ_{eff} is the effective scattering cross-

sectional area, which is calculated according to

$$\sigma_{\text{eff}} = \pi(\frac{D_{\text{eff}}}{2})^2 \tag{6.4}$$

$$D_{\text{eff}} = D(\Delta n)^{1/4} \tag{6.5}$$

The mean of the distribution $f_{\text{FP}}(x)$ is $(\sigma_{\text{eff}} N)^{-1}$, and it is as shown in Figure 6.4. D_{eff} represents the effective particle size diameter based on RGD approximation.

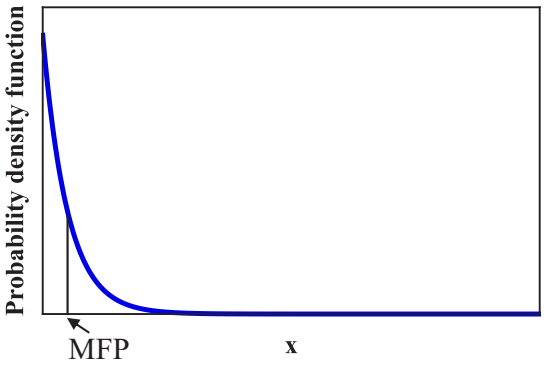

Figure 6.4: The probability density function of free path

Due to the refractive index difference (Δn) of the optically soft particles and the matrix material being tiny, the RGD scattering approximation is considered. The parameter of refractive index difference is added to the effective diameter $D_{\text{eff}} = D \times \sqrt[4]{\Delta n}$. D represents the average geometric diameter of the optically soft particles. In addition, the deflected angle ($\Delta\theta$) is chosen randomly from the Cauchy distribution defined by the probability density function of

$$f(x; x_0, \gamma) = \frac{1}{\pi\gamma(1 + (\frac{x - x_0}{\gamma})^2} \tag{6.6}$$

, where γ is its scale parameter, x_0 is location parameter. $f(x; x_0, \gamma)$ is also plotted in 6.5(a). The scale parameter γ of the Cauchy distribution is a single diffusion angle considering the RGD approximation. It is primarily affected by the refractive index difference Δn. During the actual model construction, the calculation

of γ is required by comparing the experimentally measured total diffusion angle with the RW scattering model simulated total diffusion angle, and its calculation results are shown in Fig. 6.5(b). This was also discussed in Section 4.3.3. According to the fitting results, the relationship between γ and Δn is considered as equation 6.7, when the thickness t is less than or close to 1 mm, and the refractive index difference Δn is less than 0.02.

$$\gamma = 0.29\Delta n \, (0 < \Delta n < 0.02) \tag{6.7}$$

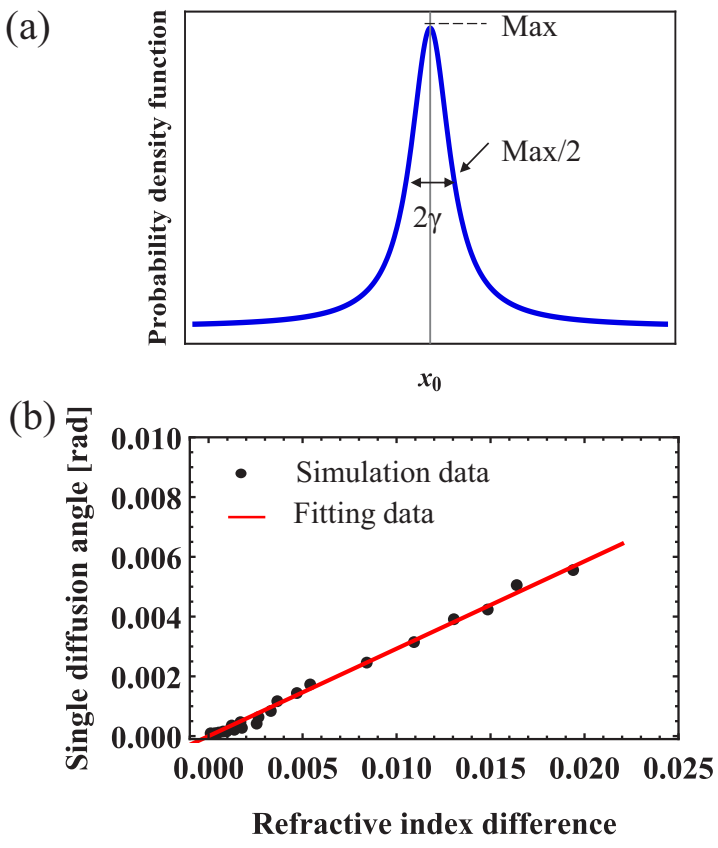

Figure 6.5: (a) The probability density function of deflection angle; (b) Estimated correlation between refractive index differences and single diffusion angles (fitting curve: $\gamma = 0.29\Delta n$)

Hence, the RW model can simulate the distribution of scattered light. It solves

the shortcomings of the RGD-Hulst model, and its process of simulating scattered light to calculate the effective transmittance is more consistent with the actual scattering situation. Therefore, for the case of sample thickness less than 1 mm, as shown in Figure 4.11, the simulation results based on this model are applicable with the experimental results in the range of 250—450 nm. However, when the sample thickness is greater than 1 mm, the simple RW model based on this model is no longer applicable. So an improved model is expected.

6.2.2 Random walk model with thickness parameters

Although, the simple RW model in the previous section can explain and simulate the distribution of scattered light. However, when the sample thickness of the scattering material is thick, the problem can arise as shown in Figure 6.6(b), the scattering light beam will keep circulating in the model due to the MFP being small. Thus, an improved model with increased MFP and $\Delta\theta$ is needed, as shown in Figure 6.6(c).

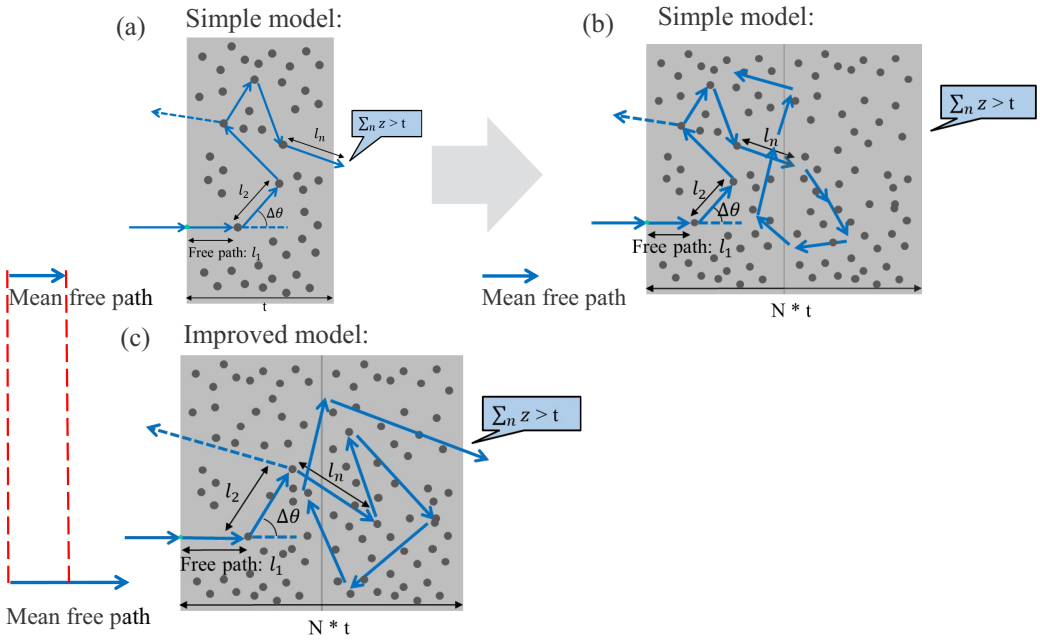

Figure 6.6: (a) Schematic diagram of the RW model, (b) the RW model under thicker samples, (c) the improved RW model under thicker samples

Then, in this section, based on the previous simple RW model, the thickness parameter is added to the model as a function of the free path probability distribution $f_{FP}(x)$ and the single diffusion angle γ as shown in equation 6.8, and equation 6.9.

$$f_{\mathrm{FP}}(x) = \sigma_{\mathrm{eff}} N (\frac{t}{t_0})^{-1} e^{-\sigma_{\mathrm{eff}} N (\frac{t}{t_0})^{-1} (x - \frac{d_{\mathrm{eff}}}{2})}, (x > \frac{d_{\mathrm{eff}}}{2}) \tag{6.8}$$

, where t is the material thickness, and t_0 (equal to 0.1) is the standard thickness used for normalization. Then, in the same way, the fitting calculation was performed based on the experimentally measured refractive index difference and total scattering angle (discussed in Section 5.2). The result is shown in Figure 6.7 (also shown in Sect. 5.2(a)). It showed the normalized single diffusion angle per unit thickness change with refractive index difference. According to the fitting results of this figure, a new single diffusion angle γ as a function of the refractive

index difference and the thickness parameter was obtained. It is shown as

$$\gamma = 9.2\Delta n^{2.4}(\frac{t}{t_0})^{0.75}\,(0 < \Delta n < 0.03) \tag{6.9}$$

Here, the model is applicable when $1 < t/t_0 < 4$ and $\Delta n < 0.03$. In addition, it can be seen that the difference in the single scattering angle γ for the same refractive index difference in Figure 6.7(a) and 6.5(b) is significant, which is because the RW model is calculated based on the SIM-360 refractive index dispersion curve fitted in the literature. At the same time, the improved RW model introduces the thickness parameter and is based on the SIM-360 dispersion results measured by the Ellipsometer for the calculation. As shown in Fig. 6.7, the measured data here refers to the result of subtracting the refractive index dispersion curve obtained from the ellipsometer measurement of the cured SIM-360 film (as shown in Figure 5.1) from the CaF_2 dispersion curve. Lit. 1, 2, 3 represent the calculated results of subtracting the fitted SIM-360 refractive index dispersion curve (Lit. 3 is shown in Figure 4.6(b)) from the CaF_2 dispersion curve. The refractive index dispersion curve of SIM-360 was fitted using the Sellmeier equation by determining the intersection with CaF_2 in the UV region and the visible refractive index obtained from the literature [67]. Lit. 1, 2, 3 represent the results of the fitting of different Sellmeier coefficients, respectively. It can be seen that they are consistent, which indicates that the stability of the fitting results is good. In addition, it is obvious that the slope of the measured results differs significantly from that of the fitted results, which explains why the single diffusion angles (calculated based on the same total scattering angle 4.8(b)) obtained from the same refractive index difference of the RW model before and after the improvement are different.

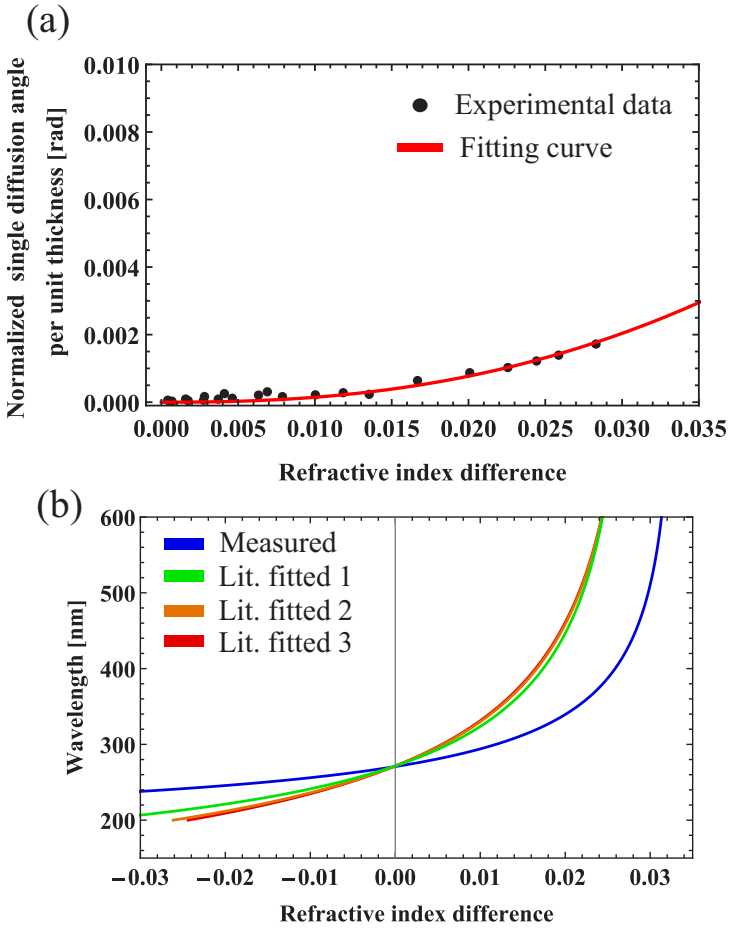

Figure 6.7: (a) Relationship between the refractive index difference and the normalized single diffusing angle per unit thickness—$\gamma(t_0/t)^{0.75}$ (fitting curve: $9.2\Delta n^{2.4}$), the same with figure 5.2(a); (b) Comparison of the refractive index difference between CaF_2 and cured SIM-360 used before and after RW model improvement ($n_{CaF_2} - n_{SIM-360}$). The measured data were used in the improved RW model in Chapter 5. Lit. 3 was used in the RW model in Chapter 4. (Lit. 1, 2, 3 are the fit results with Sellmeier coefficients B_i equal 1, 2, 3 respectively)

Also, this improved RW model can effectively simulate the actual scattering distribution since the improved model is still based on the principle of random walk. Then, the matching results between the simulation results of this model and the experimental results, as shown in Figures 5.2(b) and 5.11 in Chapter

5. For samples of different thicknesses, it is applicable in the UV and visible regions from 220—450 nm. Hence, this further improved the scattering RW model and constructs a generalized stochastic scattering model that allows quantitative prediction of scattering and spectroscopic properties of hybrid materials within a specific range (will be discussed in Section 5.2). It is expected to help model the prediction of general scattering phenomena based on tiny refractive index differences.

6.3. Conclusion

In this chapter, three models are presented to simulate the calculation of effective transmittance and scattered light distribution. First, the RGD-Hulst-based model is applicable in the UV region near SRIM and can be used to calculate the effects of particle size and its distribution, and sample concentration on the spectroscopic performance. Next, the simple RW model is also applicable in the UV region near the SRIM wavelength. It can be used to calculate the effects of sample concentration and thickness on spectroscopic performance in partial cases, and simulate the scattered light distribution under some conditions. Finally, an improved RW scattering model has the properties of the simple RW model and demonstrates applicability in both the UV and visible regions. It not only can simulate the scattered light distribution, but It can also predict the effect of most of the concentration and thickness variations on the spectroscopic performance of the sample.

Chapter 7

Conclusion

7.1. Achievements

In this thesis, spectroscopic scattering hybrid materials transparent at specific wavelengths were creatively developed by dispersing inorganic particulate materials (CaF_2/SiO_2) into organic PDMS matrix materials based on the principle of spectroscopic refractive index matching (SRIM). Then, after evaluating the various properties of the material, we realized the tunability of the transparent wavelength by adjusting the refractive index dispersion through multiple dispersions. At the same time, several scattering models were constructed to match the experimental results. Based on these scattering models, the optimal conditions for the spectroscopic performance were identified. An optical module satisfying the spectroscopic performance of DNA/protein detection was developed under the optimal conditions. The accomplishment of this thesis is summarized as follows.

In Chapter 3, the possibility of the principle was demonstrated based on the proposed spectroscopic refractive index matching principle based on inorganic particulate materials such as CaF_2/SiO_2 dispersed into organic PDMS matrix materials. Then, spectroscopic scattering materials transparent at $251, 259, 278$ and $304,$ nm were developed by mixing with four different PDMS matrix materials (LMW-PDMS, KE-103, SIM-360, Sylgard-184) that they have slight refractive index dispersion differences, respectively. It is also demonstrated that the position and order of the transparent peak wavelengths can be inferred from the cut-off wavelength of the PDMS matrix material. Among them, the 1 mm thick sample of CaF_2 dispersing SIM-360 shows a high transmittance of more than 80 % at the transparent wavelength (up to more than 95 % after regularization with pure SIM-360 samples) with 15 wt.% concentration. It also shows the spectroscopic performance with the narrowest effective transmittance line width of 28 nm for a sample of 60 wt.% dispersion concentration of 1 mm thickness. Finally, the calcu-

lations based on the scattered light distribution measurements at UV and visible wavelengths combined with the RGD-Huslt scattering approximation can be used to explain the effective transmittance of the spectroscopic scattering material in the wavelength region of 240-310 nm. And it is indicated that the spectroscopic performance of the material can be improved by increasing the average diameter of CaF_2 particles and narrowing the distribution.

In Chapter 4, different thicknesses of spectroscopic scattering films were fabricated based on 30 wt.% concentration of CaF_2 dispersed SIM-360 substrate material, and their temperature and strain responses were evaluated. Due to the significant negative thermo-optical coefficient of PDMS, the experimental results show a peak wavelength response of transmittance of 1.5 nm $^{\circ}C^{-1}$. On the other hand, it is also figured out that the stretching ratio of less than 12 % does not affect the peak transmittance wavelength. Then, the tunability of the transparent wavelength was achieved by multiple dispersion of LMW-PDMS or CQDs materials into CaF_2:PDMS scattering materials. The 10 nm blue shift, and 17 nm redshift of the transparent wavelength were achieved experimentally by dispersing 50 % of LMW-PDMS and 1.4 wt.% of CQDs dispersant, respectively. In addition, the scattered light distribution of the spectroscopic scattering materials at different wavelengths was re-evaluated based on a femtosecond laser, and a random scattering model was constructed based on the Monte Carlo principle with the RGD approximation considered. The model extends the range of effective transmittance spectra that can be interpreted and can simulate the distribution of scattered light and predict the experimental results by combining the actual scattered light reception angle.

In Chapter 5, the random scattering model is improved by adding a thickness parameter based on the RGD-Hulst scattering approximation calculation in Chapter 3 and the random scattering model in Chapter 4. The optimum conditions

for spectroscopic performance optimization are also indicated: using a narrowed CaF_2 particle distribution (1-20 μm), a high concentration of 80 wt.%, and a 4 mm sample thickness. Then, the CaF_2 particle distribution obtained from 3D milling machine with a diamond drill of high-purity CaF_2 molding materials was narrowed by precipitation and centrifugal separation to achieve the target of a basic distribution of CaF_2 particle size of 1-20 μm (where the particle removal rates were 75 %, and 100 % for particles below 1 μm and above 20 μm, respectively). Then, various samples were made by dispersing CaF_2 into PDMS at high concentration without curing agent under optimum conditions. The CaF_2-dispersed LMW-PDMS at 80 wt.% at high concentration achieved the narrowest effective transmittance bandwidth of 12 nm. Finally, the uncured 4 mm thick CaF_2-dispersed KE-103 high concentration sample was combined with a UV LED (260 nm central wavelength) to develop an optical module with a narrow emission spectrum of 9 nm bandwidth. This provides a solid foundation for constructing a microfluidic chip for DNA/protein differentiation detection.

7.2. Future perspective

In summary, this paper demonstrates the feasibility of developing spectroscopic scattering hybrid materials transparent at specific wavelengths by dispersing inorganic particulate materials into organic matrix materials based on the principle of spectral refractive index matching (SRIM). It also demonstrates the possibility of developing effective bandpass filtering performance at the 10 nm level. The tunability of transparent wavelengths is achieved by adjusting the refractive index dispersion of organic materials through multiple dispersed. The transparent wavelength can be tuned in the range of about 30 nm. The spectroscopic scattering mechanism can be well explained by RGD-Hulst + thickness-calibration

RW model except for the beam profile. Increasing the spatial density is the most effective way to improve spectroscopic performance compared to increasing the effective scattering cross-sectional area of particles and sample thickness. The future prospects of these results are up-and-coming, as described below. As mentioned in Chapters 3, 4, and 5, the spectroscopic scattering material is characterized by a simple fabrication process, the low fabrication cost is not limited by the angle of the incident light, and has flexibility and a certain degree of mobility. Moreover, its transparent wavelength and spectral properties can be easily adjusted by adjusting the concentration, thickness, and size of the dispersed particles to make it on demand. Compared with traditional filter devices, it has a broader application scenario, such as the development of small integrated absorbance photometers, wearable optoelectronic devices, microfluidic chips, etc.

Acknowledgements

I would like to express my gratitude to my supervisor, Professor Oki, for his guidance during the course of this study. He has helped me a lot in research, correcting various research papers, and practicing presentations.

I would also like to thank the supervisors of this thesis, Professor Kimura, Professor Kato, Associate Professor Tate, for their many suggestions on this thesis.

I would also like to thank Assistant Professor Yoshioka for his help and support during my time in the research lab.

I would like to express my gratitude to Dr. Chen and Associate Professor Wan, who worked together, for their knowledge and advice during daily research discussions.

I would like to express my gratitude to Mr. Morita of the USHIO company because I participated in various academic conferences and exhibitions through collaborative research with USHIO, which were precious experiences for me.

I would like to thank all the students in my lab for their help and support. In particular, I would like to thank Nakakubo and Mikami, who had worked in the same lab for almost six years; Malasuk, Nasir, Liao, Zhao, Liu, and Sakai. I would like to thank them for all their help and support in my research and life.

I sincerely acknowledge the financial support from the China Scholarship Council (CSC) for my doctoral studies under the National Scholarship Program (Program Number: 201908050217).

Last but not least, I would like to express my deepest gratitude to my family and friends who have been taking care of me so far. Especially my father and mother, who have given so much in the more than 20 years since I started school. Thanks to them, I was able to complete my Ph.D. thesis. Thank you all very much.

Junfeng Zhu

Acronyms

SRIM	Spectroscopic refractive index matching
PDMS	Polydimethylsiloxane
MOF	Metal organic frameworks
SOT	Silicone optical technology
UV	Ultraviolet
RI	Refractive index
RIs	Refractive indices
EMA	Effective medium approximation
RGD	Rayleigh-Gans-Debye
RW model	Random walk model
LL model	Lorentz–Lorenz model
MG model	Maxwell–Garnett model
SEM	Scanning electron microscope
MFP	Mean free path
LMW-PDMS	Low molecular weight Polydimethylsiloxane
FIB	Focused ion beam
CQDs	Colloidal quantum dots
FWHM	full width at half maximum
PMMA	Polymethyl methacrylate
CCD camera	Charge-coupled device camera
LED	Light-emitting diode
CS	Cross section
PMT	Photomultiplier tubes
DPSS laser	Diode-pumped solid-state laser
RT	Room temperature

References

[1] D. C. BV and D. HYDRAULICS, "Absorption spectroscopy," 1962.

[2] J. Slavík, "Absorption spectroscopy," *Intracellular pH and its Measurement*, p. 69, 1989.

[3] J. R. Lakowicz, *Principles of fluorescence spectroscopy*. Springer science & business media, 2013.

[4] S. Weiss, "Fluorescence spectroscopy of single biomolecules," *Science*, vol. 283, no. 5408, pp. 1676–1683, 1999.

[5] C. A. Royer, "Fluorescence spectroscopy," *Protein stability and folding*, pp. 65–89, 1995.

[6] J. M. Hollas, *Modern spectroscopy*. John Wiley & Sons, 2004.

[7] W. Kemp, *Organic spectroscopy*. Macmillan International Higher Education, 2017.

[8] W. W. Parson, *Modern optical spectroscopy*, vol. 2. Springer, 2007.

[9] N. V. Tkachenko, *Optical spectroscopy: methods and instrumentations*. Elsevier, 2006.

[10] F. Parker, *Applications of infrared spectroscopy in biochemistry, biology, and medicine*. Springer Science & Business Media, 2012.

[11] H. Günther, *NMR spectroscopy: basic principles, concepts and applications in chemistry*. John Wiley & Sons, 2013.

[12] B. M. Weckhuysen and D. E. Keller, "Chemistry, spectroscopy and the role of supported vanadium oxides in heterogeneous catalysis," *Catalysis Today*, vol. 78, no. 1-4, pp. 25–46, 2003.

[13] L.-P. Choo-Smith, H. Edwards, H. P. Endtz, J. Kros, F. Heule, H. Barr, J. S. Robinson Jr, H. Bruining, and G. Puppels, "Medical applications of raman spectroscopy: from proof of principle to clinical implementation," *Biopolymers: Original Research on Biomolecules*, vol. 67, no. 1, pp. 1–9, 2002.

[14] K. Strzelak, C. Malasuk, O. Yuji, K. Morita, and R. Ishimatsu, "3d printed silicone platforms with laser-scattering protein detection under flow analysis conditions as a development of silicone optical technology (sot)," *Microchemical Journal*, vol. 157, p. 104936, 2020.

[15] C. Malasuk, R. Ishimatsu, K. Morita, H. Yoshioka, and Y. Oki, "Flow-through optical device based on silicone optical technology (sot) for determination of iron in drinkable tap water," *Microchemical Journal*, vol. 157, p. 104897, 2020.

[16] K. Nakakubo, H. Yoshioka, K. Morita, R. Ishimatsu, A. Kiani, H. Hallen, M. D. Dickey, and Y. Oki, "Dynamic control of reflective/diffusive optical surfaces on egain liquid metal," *Optical Materials Express*, vol. 11, no. 7, pp. 2099–2108, 2021.

[17] K. Nakakubo, H. Nomada, H. Yoshioka, K. Morita, and Y. Oki, "Gallium and polydimethylsiloxane molding for self-organized spherical lens surface fabrication," *Applied Optics*, vol. 56, no. 36, pp. 9900–9906, 2017.

[18] H. Nomada, K. Morita, H. Higuchi, H. Yoshioka, and Y. Oki, "Carbon polydimethylsiloxane based integratable optical technology for spectroscopic analysis," *Talanta*, vol. 166, pp. 428–432, 2017.

[19] G. M. Whitesides, "The origins and the future of microfluidics," *nature*, vol. 442, no. 7101, pp. 368–373, 2006.

[20] D. J. Beebe, G. A. Mensing, and G. M. Walker, "Physics and applications of microfluidics in biology," *Annual review of biomedical engineering*, vol. 4, no. 1, pp. 261–286, 2002.

[21] T. M. Squires and S. R. Quake, "Microfluidics: Fluid physics at the nanoliter scale," *Reviews of modern physics*, vol. 77, no. 3, p. 977, 2005.

[22] E. K. Sackmann, A. L. Fulton, and D. J. Beebe, "The present and future role of microfluidics in biomedical research," *Nature*, vol. 507, no. 7491, pp. 181–189, 2014.

[23] G. M. Whitesides, A. D. Stroock, *et al.*, "Flexible methods for microfluidics," *Phys. Today*, vol. 54, no. 6, pp. 42–48, 2001.

[24] E. Verpoorte and N. F. De Rooij, "Microfluidics meets mems," *Proceedings of the IEEE*, vol. 91, no. 6, pp. 930–953, 2003.

[25] R. Seemann, M. Brinkmann, T. Pfohl, and S. Herminghaus, "Droplet based microfluidics," *Reports on progress in physics*, vol. 75, no. 1, p. 016601, 2011.

[26] H. Bruus, *Theoretical microfluidics*, vol. 18. Oxford university press, 2007.

[27] N.-T. Nguyen, S. T. Wereley, and S. A. M. Shaegh, *Fundamentals and applications of microfluidics*. Artech house, 2019.

[28] J. D. Wang, N. J. Douville, S. Takayama, and M. ElSayed, "Quantitative analysis of molecular absorption into pdms microfluidic channels," *Annals of biomedical engineering*, vol. 40, no. 9, pp. 1862–1873, 2012.

[29] J. Kuncova-Kallio and P. J. Kallio, "Pdms and its suitability for analytical microfluidic devices," in *2006 International Conference of the IEEE Engineering in Medicine and Biology Society*, pp. 2486–2489, IEEE, 2006.

[30] E. Leclerc, Y. Sakai, and T. Fujii, "Microfluidic pdms (polydimethylsiloxane) bioreactor for large-scale culture of hepatocytes," *Biotechnology progress*, vol. 20, no. 3, pp. 750–755, 2004.

[31] J. R. Anderson, D. T. Chiu, R. J. Jackman, O. Cherniavskaya, J. C. McDonald, H. Wu, S. H. Whitesides, and G. M. Whitesides, "Fabrication of topologically complex three-dimensional microfluidic systems in pdms by rapid prototyping," *Analytical chemistry*, vol. 72, no. 14, pp. 3158–3164, 2000.

[32] T. Fujii, "Pdms-based microfluidic devices for biomedical applications," *Microelectronic Engineering*, vol. 61, pp. 907–914, 2002.

[33] L. Gervais and E. Delamarche, "Toward one-step point-of-care immunodiagnostics using capillary-driven microfluidics and pdms substrates," *Lab on a Chip*, vol. 9, no. 23, pp. 3330–3337, 2009.

[34] K. Kotz, K. Noble, and G. Faris, "Optical microfluidics," *Applied physics letters*, vol. 85, no. 13, pp. 2658–2660, 2004.

[35] D. Psaltis, S. R. Quake, and C. Yang, "Developing optofluidic technology through the fusion of microfluidics and optics," *nature*, vol. 442, no. 7101, pp. 381–386, 2006.

[36] H. Gong, M. Beauchamp, S. Perry, A. T. Woolley, and G. P. Nordin, "Optical approach to resin formulation for 3d printed microfluidics," *RSC advances*, vol. 5, no. 129, pp. 106621–106632, 2015.

[37] A. Ymeti, J. S. Kanger, J. Greve, G. Besselink, P. Lambeck, R. Wijn, and R. Heideman, "Integration of microfluidics with a four-channel integrated optical young interferometer immunosensor," *Biosensors and Bioelectronics*, vol. 20, no. 7, pp. 1417–1421, 2005.

[38] B. Kuswandi, J. Huskens, W. Verboom, *et al.*, "Optical sensing systems for microfluidic devices: a review," *Analytica chimica acta*, vol. 601, no. 2, pp. 141–155, 2007.

[39] W. G. Lee, Y.-G. Kim, B. G. Chung, U. Demirci, and A. Khademhosseini, "Nano/microfluidics for diagnosis of infectious diseases in developing countries," *Advanced drug delivery reviews*, vol. 62, no. 4-5, pp. 449–457, 2010.

[40] P. Gross, G. Farge, E. J. Peterman, and G. J. Wuite, "Combining optical tweezers, single-molecule fluorescence microscopy, and microfluidics for studies of dna–protein interactions," *Methods in enzymology*, vol. 475, pp. 427–453, 2010.

[41] A. Evilevitch, L. Lavelle, C. M. Knobler, E. Raspaud, and W. M. Gelbart, "Osmotic pressure inhibition of dna ejection from phage," *Proceedings of the National Academy of Sciences*, vol. 100, no. 16, pp. 9292–9295, 2003.

[42] J. Z. Porterfield and A. Zlotnick, "A simple and general method for determining the protein and nucleic acid content of viruses by uv absorbance," *Virology*, vol. 407, no. 2, pp. 281–288, 2010.

[43] P. Brescia, "Micro-volume purity assessment of nucleic acids using a260/a280 ratio and spectral scanning," 2012.

[44] F. B. Myers and L. P. Lee, "Innovations in optical microfluidic technologies for point-of-care diagnostics," *Lab on a Chip*, vol. 8, no. 12, pp. 2015–2031, 2008.

[45] J. L. Shaw, "Practical challenges related to point of care testing," *Practical laboratory medicine*, vol. 4, pp. 22–29, 2016.

[46] C. P. Price, "Point of care testing," *Bmj*, vol. 322, no. 7297, pp. 1285–1288, 2001.

[47] E. Murray, D. Fitzmaurice, and D. McCahon, "Point of care testing for inr monitoring: where are we now?," *British journal of haematology*, vol. 127, no. 4, pp. 373–378, 2004.

[48] E. M. Van Cott, "Point-of-care testing in coagulation," *Clinics in laboratory medicine*, vol. 29, no. 3, pp. 543–553, 2009.

[49] S. K. Vashist, P. B. Luppa, L. Y. Yeo, A. Ozcan, and J. H. Luong, "Emerging technologies for next-generation point-of-care testing," *Trends in biotechnology*, vol. 33, no. 11, pp. 692–705, 2015.

[50] H. N. Chan, M. J. A. Tan, and H. Wu, "Point-of-care testing: applications of 3d printing," *Lab on a Chip*, vol. 17, no. 16, pp. 2713–2739, 2017.

[51] J. Lu, S. Ge, L. Ge, M. Yan, and J. Yu, "Electrochemical dna sensor based on three-dimensional folding paper device for specific and sensitive point-of-care testing," *Electrochimica Acta*, vol. 80, pp. 334–341, 2012.

[52] R. Sista, Z. Hua, P. Thwar, A. Sudarsan, V. Srinivasan, A. Eckhardt, M. Pollack, and V. Pamula, "Development of a digital microfluidic platform for point of care testing," *Lab on a Chip*, vol. 8, no. 12, pp. 2091–2104, 2008.

[53] J. R. Choi, J. Hu, Y. Gong, S. Feng, W. A. B. W. Abas, B. Pingguan-Murphy, and F. Xu, "An integrated lateral flow assay for effective dna amplification and detection at the point of care," *Analyst*, vol. 141, no. 10, pp. 2930–2939, 2016.

[54] J. Joung, A. Ladha, M. Saito, M. Segel, R. Bruneau, M.-l. W. Huang, N.-G. Kim, X. Yu, J. Li, B. D. Walker, *et al.*, "Point-of-care testing for covid-19 using sherlock diagnostics," *MedRxiv*, 2020.

[55] L. Zhang, B. Ding, Q. Chen, Q. Feng, L. Lin, and J. Sun, "Point-of-care-testing of nucleic acids by microfluidics," *TrAC Trends in Analytical Chemistry*, vol. 94, pp. 106–116, 2017.

[56] A. Warsinke, "Point-of-care testing of proteins," *Analytical and bioanalytical chemistry*, vol. 393, no. 5, pp. 1393–1405, 2009.

[57] C. D. Chin, S. Y. Chin, T. Laksanasopin, and S. K. Sia, "Low-cost microdevices for point-of-care testing," in *Point-of-care diagnostics on a chip*, pp. 3–21, Springer, 2013.

[58] J. S. Ahn, S. Choi, S. H. Jang, H. J. Chang, J. H. Kim, K. B. Nahm, S. W. Oh, and E. Y. Choi, "Development of a point-of-care assay system for high-

sensitivity c-reactive protein in whole blood," *Clinica chimica acta*, vol. 332, no. 1-2, pp. 51–59, 2003.

[59] A. St John and C. P. Price, "Economic evidence and point-of-care testing," *The Clinical Biochemist Reviews*, vol. 34, no. 2, p. 61, 2013.

[60] J. Zhu, K. Nakakubo, Y. Mikami, H. Yoshioka, K. Morita, and Y. Oki, "Investigation and modeling of uv band-pass-filtering white compound materials for potting or embedding in micro-optical applications," *Optical Materials Express*, vol. 9, no. 3, pp. 1002–1014, 2019.

[61] K. Nakakubo, J. Zhu, Y. Mikami, H. Yoshioka, K. Morita, and Y. Oki, "Novel spectroscopic transparent/scattering material for 260/280nm ultraviolet optical detection," in *CLEO: QELS_Fundamental Science*, pp. JTh2A–86, Optical Society of America, 2018.

[62] J. Zhu, L. Wan, C. Zhao, R. Sakai, Y. Mikami, T. Feng, C. Chen, W. Liu, H. Yoshioka, Z. Li, *et al.*, "Tunable and flexible deep-ultraviolet bandpass filters based on micro-and nanoparticle/polydimethylsiloxane hybrid membranes," *Optical Materials*, vol. 115, p. 111073, 2021.

[63] J. Zhu, R. Sakai, C. Zhao, H. Yoshioka, K. Morita, and Y. Oki, "Development of ultraviolet down conversion filters based on scattering filter materials," in *CLEO: Science and Innovations*, pp. JTu2F–6, Optical Society of America, 2020.

[64] J. Zhu, C. Zhao, R. Sakai, H. Yoshioka, and Y. Oki, "The particle size distribution influence on the spectroscopic performance of caf2 dispersed pdms hybrid materials," in *Optical Components and Materials XVIII*, vol. 11682, p. 116821I, International Society for Optics and Photonics, 2021.

[65] J. Zhu, L. Wan, C. Zhao, W. Liu, Y. Oki, and H. Yoshioka, "Narrow-bandpass transparent/diffusing materials using soft scattering based on dispersed refractive index difference," *Optical Materials Express*, vol. 12, no. 2, pp. 738–750, 2022.

[66] V. Danilov, C. Dölle, M. Ott, H. Wagner, and J. Meichsner, "Plasma treatment of polydimethylsiloxane thin films studied by infrared reflection absorption spectroscopy," 2009.

[67] D. C. Miller, M. D. Kempe, C. E. Kennedy, and S. R. Kurtz, "Analysis of transmitted optical spectrum enabling accelerated testing of multijunction concentrating photovoltaic designs," *Optical Engineering*, vol. 50, no. 1, p. 013003, 2011.

[68] I. H. Malitson, "Interspecimen comparison of the refractive index of fused silica," *Josa*, vol. 55, no. 10, pp. 1205–1209, 1965.

[69] OKEN Corporation, "Synthetic optical crystals." `http://www.oken.co.jp/ebook5/crystal.html`, Last accessed on 2022-01-05.

[70] W. Sellmeier, "Ueber die durch die aetherschwingungen erregten mitschwingungen der körpertheilchen und deren rückwirkung auf die ersteren, besonders zur erklärung der dispersion und ihrer anomalien," *Annalen der Physik*, vol. 223, no. 12, pp. 525–554, 1872.

[71] Wikipedia, "Sellmeier equation." `https://en.wikipedia.org/wiki/Sellmeier_equation`, Last accessed on 2022-01-05.

[72] T. C. Choy, *Effective medium theory: principles and applications*, vol. 165. Oxford University Press, 2015.

[73] M. Wang and N. Pan, "Predictions of effective physical properties of complex multiphase materials," *Materials Science and Engineering: R: Reports*, vol. 63, no. 1, pp. 1–30, 2008.

[74] K. E. Oughstun and N. A. Cartwright, "On the lorentz-lorenz formula and the lorentz model of dielectric dispersion," *Optics express*, vol. 11, no. 13, pp. 1541–1546, 2003.

[75] V. D. Bruggeman, "Berechnung verschiedener physikalischer konstanten von heterogenen substanzen. i. dielektrizitätskonstanten und leitfähigkeiten der mischkörper aus isotropen substanzen," *Annalen der physik*, vol. 416, no. 7, pp. 636–664, 1935.

[76] V. A. Markel, "Introduction to the maxwell garnett approximation: tutorial," *JOSA A*, vol. 33, no. 7, pp. 1244–1256, 2016.

[77] J.-B. Bossa, K. Isokoski, D. Paardekooper, M. Bonnin, E. P. van der Linden, T. Triemstra, S. Cazaux, A. G. Tielens, and H. Linnartz, "Porosity measurements of interstellar ice mixtures using optical laser interference and extended effective medium approximations," *Astronomy & Astrophysics*, vol. 561, p. A136, 2014.

[78] G. G. Hernandez-Cardoso, A. K. Singh, and E. Castro-Camus, "Empirical comparison between effective medium theory models for the dielectric response of biological tissue at terahertz frequencies," *Applied optics*, vol. 59, no. 13, pp. D6–D11, 2020.

[79] R. Apetz and M. P. Van Bruggen, "Transparent alumina: a light-scattering model," *Journal of the American Ceramic Society*, vol. 86, no. 3, pp. 480–486, 2003.

[80] H. C. Hulst and H. C. van de Hulst, *Light scattering by small particles*. Courier Corporation, 1981.

[81] F. Crapulli, D. Santoro, C. N. Haas, M. Notarnicola, and L. Liberti, "Modeling virus transport and inactivation in a fluoropolymer tube uv photoreactor using computational fluid dynamics," *Chemical Engineering Journal*, vol. 161, no. 1-2, pp. 9–18, 2010.

[82] A. Malherbe, "Interference filters for the far ultraviolet," *Applied optics*, vol. 13, no. 6, pp. 1275–1276, 1974.

[83] J. W. Lichtman and J.-A. Conchello, "Fluorescence microscopy," *Nature methods*, vol. 2, no. 12, pp. 910–919, 2005.

[84] Z. Jakšić, M. Maksimović, and M. Sarajlić, "Silver–silica transparent metal structures as bandpass filters for the ultraviolet range," *Journal of Optics A: Pure and Applied Optics*, vol. 7, no. 1, p. 51, 2004.

[85] W.-D. Li and S. Y. Chou, "Solar-blind deep-uv band-pass filter (250-350 nm) consisting of a metal nano-grid fabricated by nanoimprint lithography," *Optics express*, vol. 18, no. 2, pp. 931–937, 2010.

[86] S. Camou, H. Fujita, and T. Fujii, "Pdms 2d optical lens integrated with microfluidic channels: principle and characterization," *Lab on a Chip*, vol. 3, no. 1, pp. 40–45, 2003.

[87] Y.-L. Sung, J. Jeang, C.-H. Lee, and W.-C. Shih, "Fabricating optical lenses by inkjet printing and heat-assisted in situ curing of polydimethylsiloxane for smartphone microscopy," *Journal of biomedical optics*, vol. 20, no. 4, p. 047005, 2015.

[88] J. Chen, C. Gu, H. Lin, and S.-C. Chen, "Soft mold-based hot embossing process for precision imprinting of optical components on non-planar surfaces," *Optics express*, vol. 23, no. 16, pp. 20977–20985, 2015.

[89] W. Lee, A. Upadhya, P. Reece, and T. G. Phan, "Fabricating low cost and high performance elastomer lenses using hanging droplets," *Biomedical optics express*, vol. 5, no. 5, pp. 1626–1635, 2014.

[90] D. A. Chang-Yen, R. K. Eich, and B. K. Gale, "A monolithic pdms waveguide system fabricated using soft-lithography techniques," *Journal of lightwave technology*, vol. 23, no. 6, p. 2088, 2005.

[91] Z. Cai, W. Qiu, G. Shao, and W. Wang, "A new fabrication method for all-pdms waveguides," *Sensors and Actuators A: Physical*, vol. 204, pp. 44–47, 2013.

[92] O. Hofmann, X. Wang, A. Cornwell, S. Beecher, A. Raja, D. D. Bradley, A. J. Demello, and J. C. Demello, "Monolithically integrated dye-doped pdms long-pass filters for disposable on-chip fluorescence detection," *Lab on a Chip*, vol. 6, no. 8, pp. 981–987, 2006.

[93] K. Y. Nelson, D. W. McMartin, C. K. Yost, K. J. Runtz, and T. Ono, "Point-of-use water disinfection using uv light-emitting diodes to reduce bacterial contamination," *Environmental Science and Pollution Research*, vol. 20, no. 8, pp. 5441–5448, 2013.

[94] S. A. Brownell, A. R. Chakrabarti, F. M. Kaser, L. G. Connelly, R. L. Peletz, F. Reygadas, M. J. Lang, D. M. Kammen, and K. L. Nelson, "Assessment of a low-cost, point-of-use, ultraviolet water disinfection technology," *Journal of water and health*, vol. 6, no. 1, pp. 53–65, 2008.

[95] G. Y. Lui, D. Roser, R. Corkish, N. J. Ashbolt, and R. Stuetz, "Point-of-use water disinfection using ultraviolet and visible light-emitting diodes," *Science of the Total Environment*, vol. 553, pp. 626–635, 2016.

[96] M. Urban, J. Motteram, H.-C. Jing, S. Powers, J. Townsend, J. Devonshire, I. Pearman, K. Kanyuka, J. Franklin, and K. Hammond-Kosack, "Inactivation of plant infecting fungal and viral pathogens to achieve biological containment in drainage water using uv treatment," *Journal of applied microbiology*, vol. 110, no. 3, pp. 675–687, 2011.

[97] S. Vilhunen, H. Särkkä, and M. Sillanpää, "Ultraviolet light-emitting diodes in water disinfection," *Environmental Science and Pollution Research*, vol. 16, no. 4, pp. 439–442, 2009.

[98] A. C. Eischeid, J. N. Meyer, and K. G. Linden, "Uv disinfection of adenoviruses: molecular indications of dna damage efficiency," *Applied and Environmental Microbiology*, vol. 75, no. 1, pp. 23–28, 2009.

[99] K. G. Linden, G.-A. Shin, G. Faubert, W. Cairns, and M. D. Sobsey, "Uv disinfection of giardia lamblia cysts in water," *Environmental science & technology*, vol. 36, no. 11, pp. 2519–2522, 2002.

[100] E. Ubomba-Jaswa, C. Navntoft, M. I. Polo-Lopez, P. Fernandez-Ibáñez, and K. G. McGuigan, "Solar disinfection of drinking water (sodis): an investigation of the effect of uv-a dose on inactivation efficiency," *Photochemical & Photobiological Sciences*, vol. 8, no. 5, pp. 587–595, 2009.

[101] M. Mori, A. Hamamoto, A. Takahashi, M. Nakano, N. Wakikawa, S. Tachibana, T. Ikehara, Y. Nakaya, M. Akutagawa, and Y. Kinouchi, "Development of a new water sterilization device with a 365 nm uv-led,"

Medical & biological engineering & computing, vol. 45, no. 12, pp. 1237–1241, 2007.

[102] V. A. Oyanedel-Craver and J. A. Smith, "Sustainable colloidal-silver-impregnated ceramic filter for point-of-use water treatment," *Environmental science & technology*, vol. 42, no. 3, pp. 927–933, 2008.

[103] Y. Yoon, M. Kwon, Y. Jung, J. Moon, and J. Kang, "Development of point-of-use water disinfection technology using ceramic water filter and electrochemical hybrid system," *Water Science and Technology: Water Supply*, vol. 13, no. 4, pp. 1174–1180, 2013.

[104] T. A. Dankovich and D. G. Gray, "Bactericidal paper impregnated with silver nanoparticles for point-of-use water treatment," *Environmental science & technology*, vol. 45, no. 5, pp. 1992–1998, 2011.

[105] A. Kumar, C. Boyer, L. Nebhani, and E. H. Wong, "Highly bactericidal macroporous antimicrobial polymeric gel for point-of-use water disinfection," *Scientific reports*, vol. 8, no. 1, pp. 1–9, 2018.

[106] C. K. Pooi and H. Y. Ng, "Review of low-cost point-of-use water treatment systems for developing communities," *npj Clean Water*, vol. 1, no. 1, pp. 1–8, 2018.

[107] T. F. Clasen, J. Brown, S. Collin, O. Suntura, and S. Cairncross, "Reducing diarrhea through the use of household-based ceramic water filters: a randomized, controlled trial in rural bolivia.," *The American journal of tropical medicine and hygiene*, vol. 70, no. 6, pp. 651–657, 2004.

[108] J. Wright, S. Gundry, and R. Conroy, "Household drinking water in developing countries: a systematic review of microbiological contamination between

source and point-of-use," *Tropical medicine & international health*, vol. 9, no. 1, pp. 106–117, 2004.

[109] T. F. Clasen and A. Bastable, "Faecal contamination of drinking water during collection and household storage: the need to extend protection to the point of use," *Journal of water and health*, vol. 1, no. 3, pp. 109–115, 2003.

[110] P. Osewski, A. Belardini, M. Centini, C. Valagiannopoulos, G. Leahu, R. Li Voti, M. Tomczyk, A. Alù, D. A. Pawlak, and C. Sibilia, "New self-organization route to tunable narrowband optical filters and polarizers demonstrated with zno–znwo4 eutectic composite," *Advanced Optical Materials*, vol. 8, no. 7, p. 1901617, 2020.

[111] D. Fleischman, L. A. Sweatlock, H. Murakami, and H. Atwater, "Hyper-selective plasmonic color filters," *Optics express*, vol. 25, no. 22, pp. 27386–27395, 2017.

[112] X. He, Y. Liu, K. Ganesan, A. Ahnood, P. Beckett, F. Eftekhari, D. Smith, M. H. Uddin, E. Skafidas, A. Nirmalathas, *et al.*, "A single sensor based multispectral imaging camera using a narrow spectral band color mosaic integrated on the monochrome cmos image sensor," *APL Photonics*, vol. 5, no. 4, p. 046104, 2020.

[113] R. Rajasekharan Unnithan, M. Sun, X. He, E. Balaur, A. Minovich, D. N. Neshev, E. Skafidas, and A. Roberts, "Plasmonic colour filters based on coaxial holes in aluminium," *Materials*, vol. 10, no. 4, p. 383, 2017.

[114] Z. Hu, Y. Yin, M. U. Ali, W. Peng, S. Zhang, D. Li, T. Zou, Y. Li, S. Jiao, S.-j. Chen, *et al.*, "Inkjet printed uniform quantum dots as color conversion

layers for full-color oled displays," *Nanoscale*, vol. 12, no. 3, pp. 2103–2110, 2020.

[115] C. Markos, K. Vlachos, and G. Kakarantzas, "Bending loss and thermo-optic effect of a hybrid pdms/silica photonic crystal fiber," *Optics express*, vol. 18, no. 23, pp. 24344–24351, 2010.

[116] C. Markos, K. Vlachos, and G. Kakarantzas, "Guiding and thermal properties of a hybrid polymer-infused photonic crystal fiber," *Optical Materials Express*, vol. 2, no. 7, pp. 929–941, 2012.

[117] V. Cardinali, E. Marmois, B. Le Garrec, and G. Bourdet, "Determination of the thermo-optic coefficient dn/dt of ytterbium doped ceramics (sc2o3, y2o3, lu2o3, yag), crystals (yag, caf2) and neodymium doped phosphate glass at cryogenic temperature," *Optical Materials*, vol. 34, no. 6, pp. 990–994, 2012.

[118] D. Shah, T. Roychowdhury, J. N. Hilfiker, and M. R. Linford, "Polyethylene glycol: Optical constants from 191 to 1688 nm (0.735–6.491 ev) by spectroscopic ellipsometry," *Surface Science Spectra*, vol. 27, no. 1, p. 016001, 2020.

[119] A. C. Costa, S. Pimenta, J. F. Ribeiro, M. F. Silva, R. F. Wolffenbuttel, T. Dong, Z. Yang, and J. H. Correia, "Pdms microlenses for focusing light in narrow band imaging diagnostics," *Sensors*, vol. 19, no. 5, p. 1057, 2019.

[120] R. Niemeier and J. Rogers, "Low-cost reflective hilger–chance refractometer used to determine sellmeier coefficients of bulk polydimethylsiloxane," *Applied optics*, vol. 58, no. 22, pp. 6152–6156, 2019.

[121] M. L. Hammock, A. Chortos, B. C.-K. Tee, J. B.-H. Tok, and Z. Bao, "25th anniversary article: the evolution of electronic skin (e-skin): a brief history,

design considerations, and recent progress," *Advanced materials*, vol. 25, no. 42, pp. 5997–6038, 2013.

[122] A. Nathan, A. Ahnood, M. T. Cole, S. Lee, Y. Suzuki, P. Hiralal, F. Bonaccorso, T. Hasan, L. Garcia-Gancedo, A. Dyadyusha, *et al.*, "Flexible electronics: the next ubiquitous platform," *Proceedings of the IEEE*, vol. 100, no. Special Centennial Issue, pp. 1486–1517, 2012.

[123] D.-H. Kim, R. Ghaffari, N. Lu, and J. A. Rogers, "Flexible and stretchable electronics for biointegrated devices," *Annual review of biomedical engineering*, vol. 14, pp. 113–128, 2012.

[124] M. Stoppa and A. Chiolerio, "Wearable electronics and smart textiles: A critical review," *sensors*, vol. 14, no. 7, pp. 11957–11992, 2014.

[125] L. Xiang, H. Zhang, Y. Hu, and L.-M. Peng, "Carbon nanotube-based flexible electronics," *Journal of Materials Chemistry C*, vol. 6, no. 29, pp. 7714–7727, 2018.

[126] T.-H. Han, H. Kim, S.-J. Kwon, and T.-W. Lee, "Graphene-based flexible electronic devices," *Materials Science and Engineering: R: Reports*, vol. 118, pp. 1–43, 2017.

[127] H.-M. So, J. W. Sim, J. Kwon, J. Yun, S. Baik, and W. S. Chang, "Carbon nanotube based pressure sensor for flexible electronics," *Materials Research Bulletin*, vol. 48, no. 12, pp. 5036–5039, 2013.

[128] J. Chen, J. Zheng, Q. Gao, J. Zhang, J. Zhang, O. M. Omisore, L. Wang, and H. Li, "Polydimethylsiloxane (pdms)-based flexible resistive strain sensors for wearable applications," *Applied Sciences*, vol. 8, no. 3, p. 345, 2018.

[129] B.-S. Lin, Y.-C. Yang, C.-Y. Ho, H.-Y. Yang, and H.-Y. Wang, "A pdms-based cylindrical hybrid lens for enhanced fluorescence detection in microfluidic systems," *Sensors*, vol. 14, no. 2, pp. 2967–2980, 2014.

[130] H. Zhang, T. Qi, X. Zhu, L. Zhou, Z. Li, Y.-F. Zhang, W. Yang, J. Yang, Z. Peng, G. Zhang, *et al.*, "3d printing of a pdms cylindrical microlens array with 100% fill-factor," *ACS Applied Materials & Interfaces*, vol. 13, no. 30, pp. 36295–36306, 2021.

[131] A. Llobera, S. Demming, H. N. Joensson, J. Vila-Planas, H. Andersson-Svahn, and S. Büttgenbach, "Monolithic pdms passband filters for fluorescence detection," *Lab on a Chip*, vol. 10, no. 15, pp. 1987–1992, 2010.

[132] C. Fang, B. Dai, Z. Li, A. Zahid, Q. Wang, B. Sheng, and D. Zhang, "Tunable guided-mode resonance filter with a gradient grating period fabricated by casting a stretched pdms grating wedge," *Optics letters*, vol. 41, no. 22, pp. 5302–5305, 2016.

[133] A. Ryabchun, M. Wegener, Y. Gritsai, and O. Sakhno, "Novel effective approach for the fabrication of pdms-based elastic volume gratings," *Advanced Optical Materials*, vol. 4, no. 1, pp. 169–176, 2016.

[134] S. M. Azmayesh-Fard, L. Lam, A. Melnyk, and R. G. DeCorby, "Design and fabrication of a planar pdms transmission grating microspectrometer," *Optics express*, vol. 21, no. 10, pp. 11889–11900, 2013.

[135] P. Gutruf, E. Zeller, S. Walia, S. Sriram, and M. Bhaskaran, "Mechanically tunable high refractive-index contrast tio2–pdms gratings," *Advanced Optical Materials*, vol. 3, no. 11, pp. 1565–1569, 2015.

[136] C. Yang, K. Shi, P. Edwards, and Z. Liu, "Demonstration of a pdms based hybrid grating and fresnel lens (g-fresnel) device," *Optics express*, vol. 18, no. 23, pp. 23529–23534, 2010.